Study of Interface Modification and Perovskite Surface Morphology Control in Perovskite Solar Cells

(ペロブスカイト太陽電池の界面修飾と表面モルフォロジーの最適化に関する研究)

Graduate School of Life Science and System Engineering
Kyushu Institute of Technology

Dissertation for the Degree of Doctor of Philosophy

Putao Zhang

July 2019

Supervisor

Professor Shuzi Hayase

Abstract

Recently, perovskite solar cells (PSCs) have got much attention due to their high efficiency and low-cost fabrication. Within the last ten years, they have shown a sharp rise in efficiency from initial 3.8% to over 24% thus enabling them the most promising upcoming new generation solar cells. But, the bottom neck of PSCs lie in the prospect of commercialization, such as industry standard stability and further reduction of manufacturing cost. Nevertheless, the perovskite film quality has a great influence on the working stability of the PSCs. Therefore, in this thesis, we focus to enhance the stability of perovskite-based devices by controlling the morphology and utilizing the interface passivation strategy. The main research contents are as follows:

In chapter 1, development history of photovoltaic technology and the classification of solar cells have been introduced. In addition, the working principle of PSCs, the current challenges and the purpose of this thesis have been described.

In chapter 2, we demonstrate the fabrication of a triple layer mesoscopic carbon-based PSC. The carbon electrode was pre-passivated with PbI_2. The results showed that PbI_2 was strongly adsorbed on carbon surface following reaction with -OH on the carbon surface to form a C-O-Pb bond. Since the PbI_2 passivation layer effectively reduces carrier recombination, the J_{SC} and V_{OC} were improved in the carbon electrode based passivated solar cell.

In chapter 3, the mesoporous TiO_2 substrates were immersed in a certain concentration of SbI_3/DMF solution to passivate the TiO_2 surface. The results of QCM and XPS indicate that SbI_3 molecules were successfully introduced onto TiO_2 surface, and the passivation layer consisting of Ti-O-Sb bond was formed. The SbI_3 passivation layer effectively reduced the trap density of TiO_2, thereby carrier recombination was suppressed efficiently. Compared with the control device, the SbI_3 modified solar cell show much enhanced efficiency and 80% of the initial efficiency was maintained in the air under environment exposure after 60 days.

In chapter 4, the ZnO ETL was prepared by a low temperature solution process, and Nb_2O_5 was spin-coated on the top of ZnO. The Nb_2O_5 passivation layer effectively avoids the contact of perovskite and ZnO, therefore the perovskite film stability was enhanced. The results showed that after the introduction of Nb_2O_5 passivation layer stability of perovskite was enhanced and cell efficiency reached up to 14.57%.

In chapter 5, high-quality perovskite films were prepared by liquid nitrogen assisted method.

The perovskite film obtained by this method was having high-quality with dense crystal grains and pinhole free. Fabricated devices with the high-quality perovskite film showed a PCE of 16.53%. The photoconversion efficiency performance remained above 89% of initial PCE following one month of storage in a desiccator at room temperature.

Finally, the conclusions and prospects are presented. Perovskite solar cells are facing significant challenges in terms of long-term stability and production costs. It would have great significance to further study preparation of PSCs in the air environment.

Table of Contents

Chapter 1. Introduction

1.1 Solar energy

The continuous development of human society has led to the growing demand for energy. However, the non-renewable energy, resources especially oil, natural gas, and coal mines, essential energy resources in human life are about to be exhausted. The excessive use of this fossil energy has caused serious damage to the environment. Finding and utilizing clean and renewable energy has become the key to sustainable development in today's society.[1]Human beings have developed and utilized a variety of new energy sources such as solar energy, nuclear energy, wind energy, biomass energy, hydro energy, and geothermal energy. Among them, solar energy is an easily available and giant resource of green energy. Making full use of solar energy can effectively alleviate energy and environmental problems. At present, there are three main ways in which humans use solar energy, such as light energy-thermal energy conversion, light energy-electric energy conversion, and light energy-chemical energy conversion. Among them, the solar energy-electric energy conversion process using solar cells with high PCE and less geographical restrictions, is the most common way to use solar energy. [2] The development of high-efficiency, the low-cost solar cell is a great means for ensuring energy security and sustainable socio-economic development.

The principle of photoelectric conversion exist in converting solar energy into electrical energy through the photovoltaic effect. Photovoltaic principle refers to the absorption of photon energy by semiconductor material when sunlight shines, it influences the internal charge distribution to generate electromotive force and current. Since 1839, French scientist Edmund Becquerel has first reported the photovoltaic effect. Up to now, solar cells have been developed for more than 100 years. They are widely used in daily life, such as solar power plants, roof solar

energy panels, solar cell street lighting, satellites, etc. In general, the future of the solar cell industry is bright. New light-absorbing materials are emerging, device efficiency and stability are gradually rising, and production costs are gradually decreasing. With the continuous development of technology, in the future solar cells will play an important role. However, as the most promising clean energy in recent years, there are still some problems in photovoltaic power generation. For example, the sunlight intensity is affected by clouds and illumination angles, at nights solar cells cannot generate electricity. The low PCE of solar cells poses challenges for their future application.

1.2 Working principles and classification of solar cells

Semiconductors are the basic materials for solar cells. When two semiconductors with different doping types combine together, a p-n junction or a heterojunction will be formed. There is a built-in electric field around the p-n junction. The working principle and important physical processes of solar cells are shown in Figure 1-1:

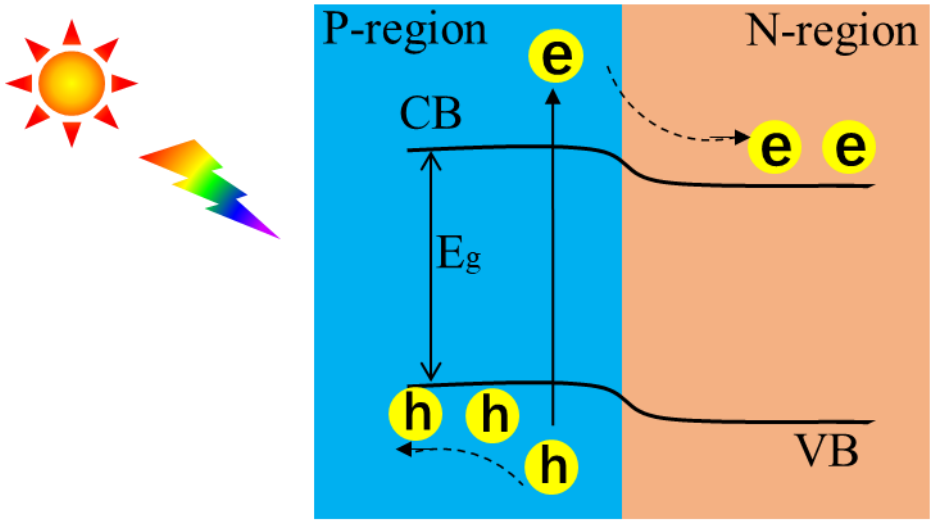

Figure 1-1 Schematic diagram of the working principle of solar cells.

The work process of perovskite devices can be roughly divided into the following steps. (1) Exciton generation and separation; (2) Free carriers transport; (3) Carriers collection and current generation; Which is also accompanied by (4) Carriers recombination.

Perovskite materials absorb sunlight and generate excitons, which rapidly separate into free electrons and holes. The free carriers diffuse to the electrode under the action of a built-in electric field; The excited electrons above the conduction band (CB) still have a chance to fall back into the valence band (VB) and recombine with the holes on the VB.

After decades of development, various types and structures of solar cells are investigated. In the classification by structure, the solar cell can be divided into Schottky junction solar cells, homojunction solar cells, and heterojunction solar cells. In the classification by material, it can be divided into silicon solar cells, compound solar cells, organic thin film solar cells, dye-sensitized solar cells. In the classification by light absorbing materials, several representative solar cells are introduced.

1.2.1 Silicon solar cells

So far, silicon solar cells are the most commercially developed solar cells. Various kinds of Silicon solar cells are available such as monocrystalline, polycrystalline and amorphous silicon solar cells. Due to the low defect density of single crystal silicon, the efficiency of single crystal silicon solar cell obtained at the laboratory scale has reached more than 26%.[3] Efficiency for silicon solar cell module has arrived above 20%, with the service life time expectancy is about 20 to 30 years. However, the purity of material requirements of monocrystalline silicon solar cells are very high ~ 99.999% or more. The preparation conditions of Silicon ingoats are also very strict, the cost and energy consumption are very high, and moreover, the pollution arisen is serious.

The polysilicon material is composed of monocrystalline silicon. At present, the polysilicon

solar cells have achieved a laboratory efficiency of more than 22%, and module efficiency exceeds 16%. Due to the high performance price ratio, the polycrystalline silicon solar cells have the largest market share among silicon solar cells. The silicon atoms in amorphous silicon materials are disorderly arranged and their production conditions are relatively mild. Therefore, the manufacturing cost of the amorphous silicon solar cells is low. The efficiency of it can reach about 14%. In addition, amorphous silicon solar cells have poor stability, so their market share is small.

1.2.2 Thin film solar cells

The major limitations in the fabrication process of silicon solar cells, lie in high energy consumption, serious pollution, and high cost, which seriously restrict the process of solar energy replacing traditional energy sources. Thin film solar cells, as an emerging solar cell device, with the advantages of the simple preparation process, high energy conversion efficiency, good stability have been rapidly developed in recent years. Common compound semiconductor thin film based solar cells have the following types: cadmium telluride (CdTe) solar cells, copper indium gallium selenide (CIGS) solar cells, gallium arsenide (GaAs) solar cells, copper zinc tin sulfur (CZTS) solar cells.

Since the cadmium telluride material is a direct bandgap semiconductor with a forbidden band gap of 1.45 eV, it is well matched to sunlight. It is insensitive to temperature changes and has good environmental stability. In 1982, Kodak Laboratory first prepared p-CdTe/n-CdS film solar cells by a chemical deposition process, and its efficiency reached ~10%. Since then, after years of continuous development, the efficiency of cadmium telluride thin-film solar cells has been continuously improved, and the most commercial efficiency certified by the NREL has reached 24.2%. In addition, many researchers have paid attention to the research of large-area applications. The cadmium thin film solar cell with an area of 6879 cm^2 has been prepared by

Solar Cell Company, and its efficiency reached 7.7%, which has a good application prospect. However, there are still some problems in CdTe thin-film solar cells. For example, CdTe is a polycrystalline thin film, in which a large number of grain boundaries are likely to become composite centers, resulting in serious grain boundary recombination; Lattice matching problems exist at heterojunction interfaces. The high defect density and trap state increase the recombination in the cells, affecting the efficiency of the device; the heavy metal element Cd is very harmful to the environment, and the element Te is a rare element with a rare content, which limits the mass production of such solar cells. CIGS thin film solar cells have similar problems to CdTe. The reserves of In element for CIGS is not rich in the earth and heavy metal elements such as Ga is harmful to the environment, which limits the further development of this solar cell.

GaAs solar cell is another representative thin film solar cell. GaAs is a direct bandgap semiconductor with an absorption coefficient 10 times of silicon, so it has great advantages in thickness. Moreover, GaAs also has good radiation resistance and small temperature coefficient, so it is very suitable for preparation of high efficiency solar cells. However, GaAs materials are very expensive, and the preparation of solar cells require the preparation of high-purity crystals, the preparation technique is complicated, resulting in the cost of the cell being much higher than that of the crystalline silicon solar cells. At the same time, the As element in GaAs has toxic limiting its further development.

In recent years, copper-zinc-tin-sulfide (CZTS) thin film solar cells with a similar structure of CIGS have been developed. This solar cell material is a rich and environmentally friendly element in the earth, and its preparation methods are also diverse. In addition to vapor deposition similar to CIGS, it can be prepared by a chemical solution method, and can achieve more than 12% power conversion efficiency. And therefore have good prospects. However, under current process the power conversion efficiency of the device is not high; at present, the characteristics

and crystallization properties of the CZTS film are not well grasped, and the preparation process of the device is complicated. Therefore, the CZTS thin film solar cells are still in the laboratory development stage, and there is still a long way to go from practical applications.

1.2.3 Organic polymer thin film solar cells

Organic polymer thin film solar cells have the advantages of low cost, simple preparation process, lightweight and flexible nature. In 1986, C.W. Tang first made a two-layer heterojunction device using a derivative of tetracarboxylic quinone and a copper phthalocyanine, which have a high absorption of visible light, and the power conversion efficiency of the device reached 1%.[4] After more than 30 years of development, the highest power conversion efficiency of single-cell organic thin-film solar cells has reached 11.7%.[5] At present, the main problem limiting the development of organic thin film solar cells is the low power conversion efficiency. At the same time, there are some problems with organic materials. For example, the material has a low dielectric constant, and the excitons have large binding energy (There is a strong Coulomb force between electrons and holes, which cannot be separated freely. We usually call such electron-hole pairs excitons), short exciton lifetime, and short diffusion length. These factors make the organic polymer thin film solar cell efficiency always have a certain distance from the inorganic solar cells.

1.2.4 Dye-sensitized solar cells

In 1991, Professor M. Grätzel of the Lausanne Institute of Advanced Industries in Switzerland reported on the breakthrough progress of dye-sensitized solar cells.[6] His work was published in the journal Nature, which has attracted wide attention from scientists in this field. The United States, Japan, Europe, and other developed countries and regions have invested a lot of manpower and material resources to carry out research and development, and the development of solar cells has entered in a new era. This can be said to be the beginning of research on dye-

sensitized solar cells. In just two years, the research team led by Professor M. Grätzel increased the efficiency of dye-sensitized solar cells from about 7.1% in 1991 to about 10% in 1993. In 1997, K. Tennakone et al. prepared a dye-sensitized solar cell with an efficiency of 10%-11%, a short-circuit current density of 18 $mA \cdot cm^{-2}$, and an open circuit voltage of 0.72 V. In 1998, Professor M. Grätzel's research team made another significant progress and developed a dye-sensitized solar cell based on solid organic transport materials which converts 33% photons to electric current, and opened the way for solid-state dye-sensitized solar cells. After this, the Toshiba company developed a quasi-solid-state dye-sensitized solar cell with a power conversion efficiency of 7.3%. In 2001, Australia's STA Company built a pilot-scale dye-sensitized solar cell factory. Dyesol, which was established in Australia in 2004, is the first to conduct industrial research on dye-sensitized solar cells. In 2006, the UK G24i built a 20MW roll-to-roll flexible dye-sensitized solar cell pilot production line, which was also an early industrialization research company. In 2013, the conversion efficiency of dye-sensitized solar cells has reached 13%.[7]

1.3 Perovskite solar cells

Perovskite solar cells have mainly the following two structures, and a simplified schematic diagram is shown in Figure 1-2.

The mesoporous support structure (a), referred to mesoporous structure, use mesoporous TiO_2 or Al_2O_3 as a scaffold, and perovskite is filled in the mesoporous structure. The planar heterojunction structure (b), referred to a planer structure and refers to the structure consisting of a multilayer film without mesoporous support. There are minor differences in the mechanism of the two structured solar cells. So we introduce the solar cell mechanism of the two structures separately.

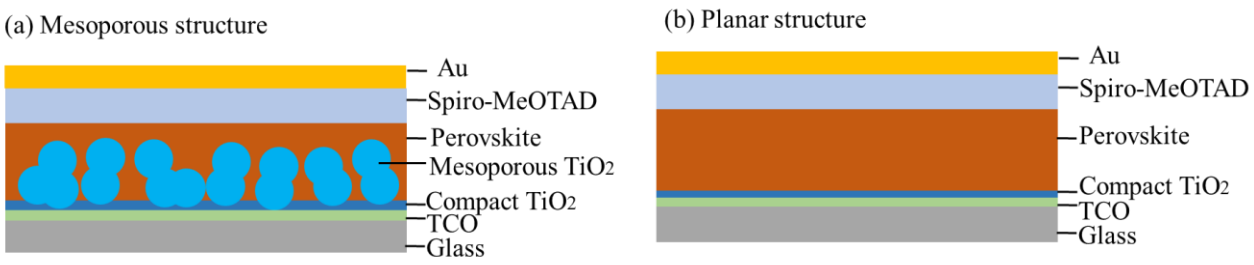

Figure 1-2Schematic diagram of mesoporous structure and planar structure perovskite solar cells.

a) Mesoporous structure (Figure 1-3a):

1. Perovskite nanocrystals adsorbed or filled in a TiO_2 scaffold absorb sunlight and generate free electrons and holes.

2. Electrons are transferred from the perovskite layer to the conduction band of TiO_2, leaving holes in the perovskite layer.

3. The electrons are collected by the electrode through the diffusion transport of the TiO_2 layer and the perovskite layer. The holes are transferred to the hole transport layer and collected by the other side electrode.

b) Planar structure (Figure 1-3b):

1. The perovskite film absorbs sunlight and produces free electrons and holes.

2. Via the perovskite layer itself, electrons and holes are transferred to the corresponding transport layer.

3. The charges are collected by the corresponding electrodes on both sides, generating current in the external circuit.

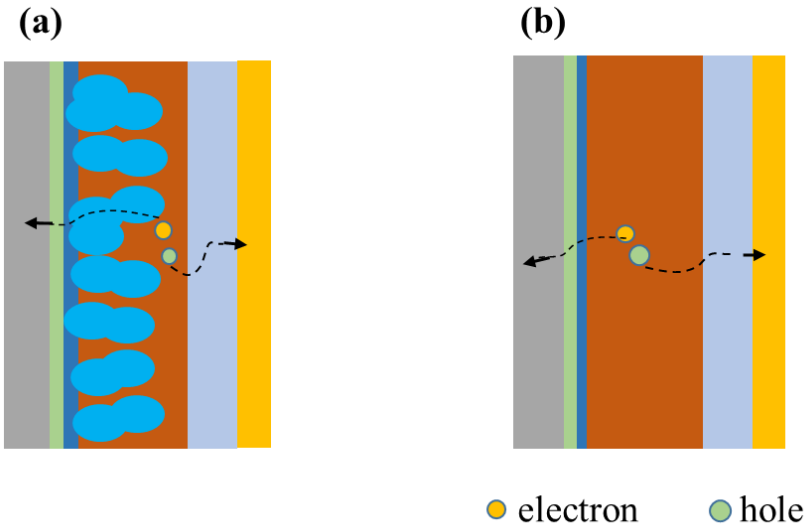

Figure 1-3 Schematic diagram of the working mechanism of perovskite solar cells. (a) Mesoporous structure, (b) Planar structure.

The perovskite material has a large absorption vibrator strength at the edge of the belt, so it has strong absorption in the visible region.[8] At the same time, the perovskite material itself can transport electrons and transport holes, so it can be applied to p-i-n junctions as well as p-n junction cells.

1.4 Development history of perovskite solar cells

In 2009, Miyasaka and his colleagues have applied organic-inorganic hybrid perovskite materials to sensitized solar cells for the first time and achieved a power conversion efficiency of 3.8%.[9] However, due to the use of liquid electrolytes, perovskite materials are highly susceptible to decomposition, resulting in poor device stability. In order to solve the influence of liquid electrolyte on the stability of perovskite solar cells, in 2012, Park et al.[10] first introduced solid-state hole transport material, Spiro-OMeTAD into perovskite solar cells to prepare all-solid-state solar cells. The devices reached a power conversion efficiency of 9.7%, and under the unpackaged condition, the efficiency decay of the device was very small after 500 h, which greatly improves the stability of the perovskite solar cells. Snaith research group replaced the

"active" TiO_2 nanoparticles with "inert" Al_2O_3 nanoparticles, and Cl containing perovskite ($CH_3NH_3PbI_{3-x}Cl_x$) was used as the light absorbing material, resulting in a mesoporous superstructure perovskite solar cell with a PCE of 10.9%.[11] Later, other research groups also reported the study of zirconium oxide (ZrO_2) and silicon oxide (SiO_2) as mesoporous materials.[12, 13]The use of non-conductive nanoparticles as mesoporous support in perovskite solar cells reveals that the perovskite material itself has a strong carrier transport capacity. In the same year, Etgar et al.[14] prepared a device without a hole transport layer. The efficiency of 5.5% under standard sunlight was obtained, which further proves that the perovskite material can be used not only as a light absorbing layer but also as a hole transport layer. From 2013, perovskite solar cells began to develop rapidly, Gratzel et al.[15] used a continuous solution deposition method to prepare a perovskite layer by spin coating a PbI_2 layer on TiO_2 and then immersing it in CH_3NH_3I solution to form a perovskite, $CH_3NH_3PbI_3$, the power conversion efficiency of the device was up to 15%. In 2014, Yang and his co-workers [16] used polyethoxyethyleneimine (PEIE) to modify ITO and Y-doped TiO_2 as an electron transport layer. The obtained perovskite solar cell device achieved an efficiency of 19.3%. The certified efficiency of perovskite solar cells produced by the KRICT Institute in Korea and UNIST University reached 22.1%.[17] So far, the highest PCE of 24.2% has been certified.[18]

1.5 Composition of perovskite solar cells

1.5.1 Electron transport layer material

In order to improve the efficiency and longevity of PSCs, we usually introduce an ETL between perovskite and the cathode. On the one hand, it reduces the energy level barrier of the electrode and the perovskite, and more favorable for carriers transporting. On the other hand, the electron transport layer forms selective contact with the perovskite layer to increase the extraction rate of electrons and effectively block the movement of holes toward the cathode, thereby reducing the

phenomenon of carrier recombination at the interface. A material that can accept and transport electrons is called electron transport material, and N-type semiconductors are usually used as electron transport material. Semiconductors with small direct bandgap has a relatively small effective electron mass and thus has high carrier mobility. For inorganic semiconductors, defects and impurities have a large impact on their electrochemical properties. The most commonly used ETM is TiO_2,[19] in addition SnO_2,[20, 21] ZnO,[22-24] etc.TiO_2 is widely used electron transport material in PSCs. Conduction band minimum (CBM) of TiO_2 is -4.1 eV, which is lower than the lowest unoccupied molecular orbital level of $CH_3NH_3PbI_3$, which is beneficial to electron injection. The property of the TiO_2 wide bandgap (3.2 and 3.0 eV for anatase and rutile phase, respectively) makes its valence band maximum (VBM) at a deeper position, effectively blocking the injection of holes. In PSCs, the TiO_2 ETL can be adjusted in the method of preparation, doping, and morphology control to adjust the energy level, electron mobility.The preparation method of TiO_2 includes sol-gel method,[25] aerosol spray pyrolysis method,[15] spin-coating method,[26] and the like. In the preparation process, the high temperature of 450 ℃ or more is usually required to convert amorphous TiO_2 into anatase TiO_2 to improve its electron transporting ability.However, high temperature preparation process limits its application to flexible substrates. Snaith and his co-workers disperse anatase TiO_2 particles (diameter <5 nm) in an ethanol solution of diisopropoxy bisacetoacetone in titanium, and the device efficiency by spin coating and sintering at low temperature (150 °C) reaches about 16%.[27] The TiO_x dense layer containing oxygen vacancies prepared at 130 °C was applied to a flexible solar cell device to obtain an efficiency of about 6.4%.[28]

1.5.2 Perovskite light absorbing layer material

Perovskite as the light absorbing material of PSCs directly impact device performance. The light absorbing layer with a wide absorption in the visible and the near-frared light region is a

necessary condition for achieving high PCE. If the band gap is too small, although it can absorb more incident light, the V_{OC} of the cells will be reduced. A material having a band gap of 1.4 eV is more suitable as an absorption layer of a solar cell.[29] In perovskite material, the band gap can be adjusted by changing the composition of the constituent elements, thereby obtaining a suitable absorption band gap. The structure of the organic-inorganic hybrid perovskite is ABX_3 type, the structure is shown in Figures 1-4. A site is an inorganic cation (Cs^+) or an organic cation (MA, FA), B site is a metal ion (Pb^{2+}, Sn^{2+}), and X site is a halogen ion (Cl^-, Br^-, I^-).

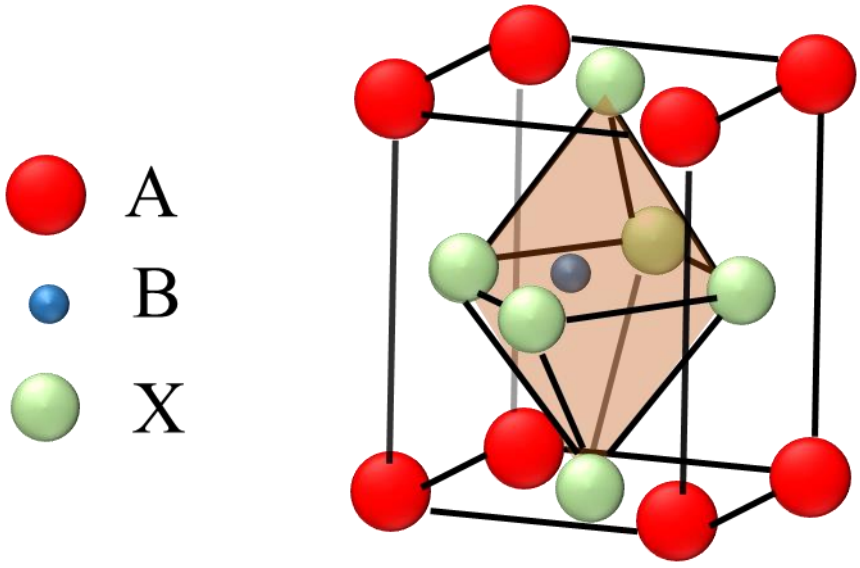

Figures 1-4 Schematic diagram of perovskite crystal structure.

Changes in the atoms or groups at the A, B, and X positions of the organic-inorganic hybrid perovskite material may affect the energy band of perovskite material. A acts as a lattice charge compensation and does not have an important effect on the energy band of the material. The organic cation size at B position causes expansion or contraction of the crystal lattice, thereby causing a change in the bond length, and thus affecting the band gap.[30, 31] The most commonly used A cations are methylamine cation ($CH_3NH_3^+$,MA^+), formamidine cation ($HC(NH_2)_2^+$,FA^+), cesium ion (Cs^+), etc., wherein the methylamine cation is the most widely

used cation, the band of perovskite $CH_3NH_3PbI_3$ is 1.55 eV with high absorption coefficient. Band gap of $FAPbI_3$ perovskite is only 1.43 eV, which can broaden the absorption spectrum to 850 nm.

The metal elements in the B position are mainly Pb^{2+}, Ge^{2+}, Sn^{2+}, etc.. The widely used perovskite material is lead-containing perovskite $MAPbI_3$, in which Pb is toxic, so it is desirable to replace it with non-toxic or low-toxic elements. Previous researches have shown that the bond angle of B-X has influence on the band gap of perovskite. As the bond angle increases, the band gap decreases. Therefore, the Sn-doped Pb perovskite material can effectively extend material absorption spectrum to the near-infrared region. However, the Sn material lattice is unstable, resulting in a decrease in material life.

The larger radius of X-halogen atoms is expected to expand the lattice of the perovskite structure. A larger atomic radius can effectively reduce the interaction between the halogen and the Pb atom, thereby improving the light absorption in the long-wave region.

1.5.3 Hole transport layer material

Spiro-MeOTADwith excellent hole transport properties are often used as a HTL material in PSCs.[10]Since Spiro-MeOTAD is difficult to purificate, a HTM containing triphenylamine is synthesized to replace Spiro-MeOTAD, such as a triphenylamine polymer PTAA.[30] By adding Li-TFSI and TBP, a good hole transport effect was exhibited. The conjugated polymer P3HT has been used in a planar structure PSC, and the cell efficiency was more than 10%.[32]The oligothiophene derivatives have good hydrophobicity and hole transport properties. And good device efficiency can be obtained no need for additives such as Li-TFSI and TBP. The inorganic hole transport layer material generally has better chemical stability, and lower preparation cost than the organic HTL material. Commonly used inorganic HTL materials are NiO, [33, 34] CuI,[35] CuSCN,[36] CuO_x,[37] CuS[38] and MoO_3,[39] etc. The inorganic HTL material has

good thermal stability, effectively enhance the stability of device. However, the PCE of perovskite photovoltaic devices based on inorganic hole transport layers is generally low. Therefore, further research is needed to improve efficiency.

1.5.4 Electrode material

In photovoltaic devices, holes and electrode are collected by high and low work function electrode, respectively. ITO and FTO are commonly used electrodes. The ITO work function is about 4.5-4.9eV,[40] with the forbidden band width of 3.7eV, and it has a high transmittance in the visible range (up to 80% or more). The FTO work function is about 4.4eV.[41] Excellent high temperature resistance, the metal electrodes for collecting holes include Au, Ag, Al, Cu, etc., as well as Ag nanowires, Ag/Al alloy electrodes etc..[42-44] Carbon electrodes (including graphene, carbon nanotubes, etc.) are also used as inexpensive and stable electrode materials in perovskite solar devices.[45-51]

1.6 Challenges and research topics

As described above, PSCs are expected to be the most competitive new-generation solar cells due to their simple preparation process and high efficiency. However, they are still facing many challenges. First, it is necessary to improve stability of device, which is the basic request for commercialization. Second, it is needed to reduce production costs. Since perovskite solar cells are multilayer structures, the interface state will have a significant impact on device performance. This thesis attempts to enhance device stability and efficiency through interface modification.

1.7 References

[1] Q. Yang; G. Chen, Energy Policy 41 (2012) 340-347.

[2] A.J. Mcevoy; Castaner, L.; Markvart, T., Academic Press: 2012.

[3] T. Saga, NPG Asia Materials 2 (2010) 96.

[4] C.W. Tang, Appl. Phys. Lett. 48 (1986) 183-185.

[5] J. Zhao; Li, Y.; Yang, G.; Jiang, K.; Lin, H.; Ade, H.; Ma, W.; Yan, H., Nature Energy 1 (2016) 15027.

[6] B. O'regan; Grätzel, M., Nature 353 (1991) 737.

[7] S. Mathew; Yella, A.; Gao, P.; Humphry-Baker, R.; Curchod, B.F.; Ashari-Astani, N.; Tavernelli, I.; Rothlisberger, U.; Nazeeruddin, M.K.; Grätzel, M., Nature chemistry 6 (2014) 242.

[8] S.D. Stranks; Snaith, H.J., Nature nanotechnology 10 (2015) 391.

[9] A. Kojima; Teshima, K.; Shirai, Y.; Miyasaka, T., J. Am. Chem. Soc. 131 (2009) 6050-6051.

[10] H.-S. Kim; Lee, C.-R.; Im, J.-H.; Lee, K.-B.; Moehl, T.; Marchioro, A.; Moon, S.-J.; Humphry-Baker, R.; Yum, J.-H.; Moser, J.E., Scientific reports 2 (2012) 591.

[11] M.A. Green; Ho-Baillie, A.; Snaith, H.J., Nature Photonics 8 (2014) 134.

[12] D. Bi; Moon, S.-J.; Häggman, L.; Boschloo, G.; Yang, L.; Johansson, E.M.; Nazeeruddin, M.K.; Grätzel, M.; Hagfeldt, A., RSC Advances 3 (2013) 18762-18766.

[13] N. Cheng; Liu, P.; Bai, S.; Yu, Z.; Liu, W.; Guo, S.-S.; Zhao, X.-Z., J. Power Sources 321 (2016) 71-75.

[14] L. Etgar; Gao, P.; Xue, Z.; Peng, Q.; Chandiran, A.K.; Liu, B.; Nazeeruddin, M.K.; GräTzel, M., J. Am. Chem. Soc. 134 (2012) 17396-17399.

[15] J. Burschka; Pellet, N.; Moon, S.-J.; Humphry-Baker, R.; Gao, P.; Nazeeruddin, M.K.; Grätzel, M., Nature 499 (2013) 316.

[16] H. Zhou; Chen, Q.; Li, G.; Luo, S.; Song, T.-b.; Duan, H.-S.; Hong, Z.; You, J.; Liu, Y.; Yang, Y., Science 345 (2014) 542-546.

[17] M. Saliba; Matsui, T.; Domanski, K.; Seo, J.-Y.; Ummadisingu, A.; Zakeeruddin, S.M.; Correa-Baena, J.-P.; Tress, W.R.; Abate, A.; Hagfeldt, A., Science 354 (2016) 206-209.

[18] https://www.nrel.gov/pv/cell-efficiency.html.

[19] J.-H. Im; Lee, C.-R.; Lee, J.-W.; Park, S.-W.; Park, N.-G., Nanoscale 3 (2011) 4088-4093.

[20] E. Halvani Anaraki; Kermanpur, A.; Mayer, M.T.; Steier, L.; Ahmed, T.; Turren-Cruz, S.-H.; Seo, J.; Luo, J.; Zakeeruddin, S.M.; Tress, W.R., ACS Energy Letters 3 (2018) 773-778.

[21] L. Xiong; Qin, M.; Chen, C.; Wen, J.; Yang, G.; Guo, Y.; Ma, J.; Zhang, Q.; Qin, P.; Li, S., Adv. Funct. Mater. 28 (2018) 1706276.

[22] J. Cao; Wu, B.; Chen, R.; Wu, Y.; Hui, Y.; Mao, B.W.; Zheng, N., Efficient, Adv. Mater. 30 (2018) 1705596.

[23] Y. Sun; Seo, J.H.; Takacs, C.J.; Seifter, J.; Heeger, A.J., Adv. Mater. 23 (2011) 1679-1683.

[24] D. Liu; Kelly, T.L., Nature photonics 8 (2014) 133.

[25] S.K. Pathak; Abate, A.; Ruckdeschel, P.; Roose, B.; Gödel, K.C.; Vaynzof, Y.; Santhala, A.; Watanabe, S.I.; Hollman, D.J.; Noel, N., Adv. Funct. Mater. 24 (2014) 6046-6055.

[26] J.-H. Im; Jang, I.-H.; Pellet, N.; Grätzel, M.; Park, N.-G., Nature nanotechnology 9 (2014) 927-932.

[27] K. Wojciechowski; Saliba, M.; Leijtens, T.; Abate, A.; Snaith, H.J., Energy & Environmental Science 7 (2014) 1142-1147.

[28] P. Docampo; Ball, J.M.; Darwich, M.; Eperon, G.E.; Snaith, H.J., Nature communications 4 (2013) 2761.

[29] W. Shockley; Queisser, H.J., J. Appl. Phys. 32 (1961) 510-519.

[30] J.H. Noh; Im, S.H.; Heo, J.H.; Mandal, T.N.; Seok, S.I., Nano Lett. 13 (2013) 1764-1769.

[31] S.A. Kulkarni; Baikie, T.; Boix, P.P.; Yantara, N.; Mathews, N.; Mhaisalkar, S., Journal of Materials Chemistry A 2 (2014) 9221-9225.

[32] B. Conings; Baeten, L.; De Dobbelaere, C.; D'haen, J.; Manca, J.; Boyen, H.G., Adv. Mater. 26 (2014) 2041-2046.

[33] Z. Zhu; Bai, Y.; Zhang, T.; Liu, Z.; Long, X.; Wei, Z.; Wang, Z.; Zhang, L.; Wang, J.; Yan, F., Angew. Chem. 126 (2014) 12779-12783.

[34] J.H. Kim; Liang, P.W.; Williams, S.T.; Cho, N.; Chueh, C.C.; Glaz, M.S.; Ginger, D.S.; Jen, A.K.Y., Adv. Mater. 27 (2015) 695-701.

[35] J.A. Christians; Fung, R.C.; Kamat, P.V., J. Am. Chem. Soc. 136 (2013) 758-764.

[36] S. Ye; Sun, W.; Li, Y.; Yan, W.; Peng, H.; Bian, Z.; Liu, Z.; Huang, C., Nano Lett. 15 (2015) 3723-3728.

[37] C. Zuo; Ding, L., Small 11 (2015) 5528-5532.

[38] H. Rao; Sun, W.; Ye, S.; Yan, W.; Li, Y.; Peng, H.; Liu, Z.; Bian, Z.; Huang, C., ACS applied materials & interfaces 8 (2016) 7800-7805.

[39] J. Liang; Zu, F.-S.; Ding, L.; Xu, M.-F.; Shi, X.-B.; Wang, Z.-K.; Liao, L.-S., Applied Physics Express 7 (2014) 111601.

[40] Y. Park; Choong, V.; Ettedgui, E.; Gao, Y.; Hsieh, B.; Wehrmeister, T.; Müllen, K., Appl. Phys. Lett. 69 (1996) 1080-1082.

[41] M.G. Helander; Greiner, M.; Wang, Z.; Tang, W.; Lu, Z., Journal of Vacuum Science & Technology A: Vacuum, Surfaces, and Films 29 (2011) 011019.

[42] Z. Jiang; Chen, X.; Lin, X.; Jia, X.; Wang, J.; Pan, L.; Huang, S.; Zhu, F.; Sun, Z., Sol. Energy Mater. Sol. Cells 146 (2016) 35-43.

[43] Y. Deng; Dong, Q.; Bi, C.; Yuan, Y.; Huang, J., Advanced Energy Materials 6 (2016) 1600372.

[44] J. Springer; Poruba, A.; Vanecek, M., J. Appl. Phys. 96 (2004) 5329-5337.

[45] A. Mei; Li, X.; Liu, L.; Ku, Z.; Liu, T.; Rong, Y.; Xu, M.; Hu, M.; Chen, J.; Yang, Y., Science 345 (2014) 295-298.

[46] S.N. Habisreutinger; Leijtens, T.; Eperon, G.E.; Stranks, S.D.; Nicholas, R.J.; Snaith, H.J., Nano Lett. 14 (2014) 5561-5568.

[47] Z. Li; Kulkarni, S.A.; Boix, P.P.; Shi, E.; Cao, A.; Fu, K.; Batabyal, S.K.; Zhang, J.; Xiong,

Q.; Wong, L.H., ACS nano 8 (2014) 6797-6804.

[48] Z. Ku; Rong, Y.; Xu, M.; Liu, T.; Han, H., Scientific reports 3 (2013) 3132.

[49] K. Cao; Zuo, Z.; Cui, J.; Shen, Y.; Moehl, T.; Zakeeruddin, S.M.; Grätzel, M.; Wang, M., Nano Energy 17 (2015) 171-179.

[50] X. Wang; Li, Z.; Xu, W.; Kulkarni, S.A.; Batabyal, S.K.; Zhang, S.; Cao, A.; Wong, L.H., Nano Energy 11 (2015) 728-735.

[51] P. You; Liu, Z.; Tai, Q.; Liu, S.; Yan, F., Adv. Mater. 27 (2015) 3632-3638.

Chapter 2. Study the effect of PbI_2 passivation on carbon electrode for perovskite solar cells by quartz crystal microbalance system

2.1 Introduction

Organic-inorganic trihalide perovskite solar cells (PSCs) have received much attention in recent years owing to their excellent optoelectronic properties such as high absorption coefficient, low exciton binding energy, nearly ambipolar nature and tunable direct band gap. In 2009, Miyasaka et al reported the first perovskite based material $CH_3NH_3PbX_3$ (X =Br or I) as light harvester in liquid-state perovskite-sensitized solar cells, and achieved the power conversion efficiency (PCE) of 3.8%.[1] Since then, the performance of PSC has been constantly refreshed and till now, the highest PCE of 22.7% has been attained.[2] PSCs have shown promising industrial potential due to their low-cost solution processable fabrication methods, involving a layer by layer deposition of an electron transporting layer (ETL), a perovskite light harvester layer, a hole transporting layer (HTL) and a metal electrode.[3-4] However, highly efficient PSCs typically require an expensive and air sensitive HTL (e.g., spiro-OMeTAD) and a metal electrode (Au or Ag) deposited by expensive vacuum based thermal evaporation techniques, limiting the large-scale production of the PSCs.[5-10] To reduce the high cost and instability due to spiro-OMeTAD, there are some reports focusing on novel HTMs[11-18] and even HTL free PSCs, [14, 19-23] but the PCE is not comparable to conventional PSCs. Therefore, the replacement of unstable HTL material and noble metal electrode with an inexpensive, earth-abundant, environment friendly material is highly desirable. As a result, in the recent past, carbon with most of these

characteristics and a suitable work function of around 5.0 eV [7, 24-25] has been successfully implemented both as HTL and hole collecting electrode.[26-31] A certified efficiency of 12.8% PSC which consists of carbon as HTL and electrode utilizing solar cell architecture with TiO_2 (perovskite)/ZrO_2 (perovskite)/Carbon (perovskite) has been reported by Han et al.[32] It was mentioned that the architecture has the advantages of simple manufacturing process, low cost and long-term stability. This report on the relatively high efficiency without hole transport layer was a surprise, which prompted us to focus on the interface between carbon and the perovskite layers. It is well known that a direct contact between the electrode and perovskite layers, increases the opportunity for the charge recombination, resulting in hampered solar cell efficiency. Therefore, a direct contact between carbon electrode and perovskite layers needs to be avoided to enhance the PCE. Mhaisalkar et al[33] reported that increasing the proportion of PbI_2 in perovskite precursors can improve the performance of perovskite solar cells. Jang and his co-workers used the method of adding carbon nanotubes to monk the interface between perovskite and carbon electrodes, improving the efficiency of carbon-based perovskite solar cells effectively.[34] We have already reported[35] that TiO_2 passivation with PbI_2 decreases the trap density on the surface of TiO_2, hence improves the PCE in conventional PSC. Similar kind of observation has been reported by Sargent et al, where TiO_2 surface passivation by $PbCl_2$ led to increase in the efficiency and stability.[36-37] Therefore, highly efficient PSCs have been obtained via the passivation of TiO_2 surface; however, similar concept has not been so far checked on the PSCs involving mesoporous carbon.

Therefore, in this work we introduce molecularly designed interface architecture between carbon and perovskite layer, resulting in the structure of (TiO_2 and PVK composite)/(ZrO_2 and PVK composite)/(Carbon passivated with PbI_2). The effect of PbI_2

passivation at the surface of carbon electrode on the performance of PSC will be discussed by analyzing the interface utilizing a quartz crystal microbalance (QCM) measurement system, which monitors the PbI_2 adsorption on the carbon surface. Here, the formation of C-O-Pb linkage on the carbon surface is discussed from the view point of enhancement of solar cell efficiency, including the advantage of two-step sequential method over one-step method.[35] The disadvantage of the one-step method,[32] such as improper pore filling and less surface coverage was overcome by the insertion of C-O-Pb layer, resulting in achieving 7.30% efficiency.

2.2 Experimental section

2.2.1 Materials.

(a). Perovskite precursor solution: Methylammonium iodide (MAI) (Wako, Japan) solution in 2-propanol (Wako, Japan) and lead iodide (PbI_2) (Tokyo Chemical Industry, Japan) solution in dimethylformamide (DMF) (Wako, Japan) were prepared, respectively, as reported earlier[38] for fabricating PSCs by employing two-step method. In one-step fabrication method, an equimolar PbI_2 and MAI were dissolved in γ-butyrolactone (Tokyo Chemical Industry, Japan); (b). Solar cell electrodes: Fluorine doped tin oxide (FTO) glass (Nippon Sheet Glass Co. Ltd.) was employed as the photoanodes. Titanium diisopropoxide bis(acetylacetonate) (Sigma Aldrich) was diluted in ethanol (Wako, Japan) to deposit a compact layer as reported in literature.[39] On the top of it, a mesoporous layer of TiO_2 (Solaronix, PST-18NR) followed by ZrO_2 (Sigma-Aldrich) completes the photoanode deposition. Carbon (Borun New Material Technology) was finally coated as the top layer to be used as a cathode. In this work, all the chemicals were used as received directly without further purification.

2.2.2 Preparation of carbon sensor for PbI_2 adsorption testing.

The QCM system (Meywafosus Co. LTD) as shown in Figure 2-1 was implemented to study the PbI_2 adsorption on the carbon surface. The carbon sensors used for QCM testing were fabricated by the following process. Firstly, Au QCM sensor was treated by oxygen plasma for 1 min to make the surface hydrophilic. Afterwards, carbon paste diluted in ethanol (carbon:ethanol, 1:20) was spin coated on the Au QCM sensor at 1000 rpm for 15 s followed by baking at 100 ℃ for 5 min. Multiple coatings were done to get the desired thickness of carbon, and finally carbon coated sensor was baked at 100 ℃ for 30 min. Once the baking was over, the carbon sensor thus obtained was allowed to cool down to room temperature and then PbI_2/DMF solution was passed over carbon sensor with a flow rate of 0.5 $\mu L \cdot s^{-1}$. QCM monitors the frequency change with the adsorption of the adsorbent on the sensor's surface. The frequency change and adsorbed mass can be described with the following Sauerbrey equation (1)[40-41]:

$$\Delta F = \frac{2F_0^2}{\sqrt{\rho\mu}} \frac{\Delta m}{A} \qquad (1)$$

Where ΔF and Δm are the frequency and weight change, respectively. F_0 is the sensor frequency, A is the sensor area, μ is the shearing stress (μ =2.947×1010 kg ms), and ρ is the density (ρ =2648 kg m^{-3})

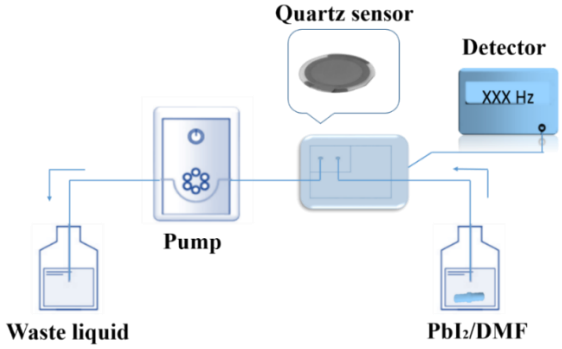

Figure 2-1 Quartz crystal microbalance measurement apparatus for measuring PbI_2 adsorption on carbon surface.

2.2.3 Fabrication of perovskite solar cell devices

Fluorine doped tin oxide (FTO) glass was etched with zinc powder and HCl aqueous (6 M) and then washed carefully with soap, acetone, isopropyl alcohol and deionized water for 15 min each. The surface of FTO was later cleaned by plasma prior to deposition of layers on the top of it. The PSC device fabrication started with the deposition of a 50 nm-thick TiO_2 compact layer (c-TiO_2) on the substrate by spray deposition of titanium diisopropoxide bis(acetylacetonate) solution diluted in ethanol (1:39, volume ration) followed by sintering at 300 °C for 10 min as illustrated earlier.[35] The mesoporous TiO_2 layer was then prepared on the top of the c-TiO_2 by spin coating a TiO_2 paste diluted in ethanol (TiO_2:Ethanol=1:4, weight ration) at 5000 rpm for 30 s followed by a sintering at 500 °C for 30 min. In the same way, ZrO_2 layer was spin coated onto the mesoporous TiO_2 layer at 5000 rpm for 30s and sintered at 400 °C for 30 min. Carbon paste was, then, screen printed and dried at 100 °C for 15min to form the cathode. The nanopores of the sample with porous triple layers finally obtained FTO/TiO_2/ZrO_2/Carbon was filled with a perovskite precursor in two ways such as one-step and two-step as presented in Figure 2-2a. Two-step deposition of perovskite was done as described earlier,[42-43] where first a 70 µL solution of PbI_2 (1 M in DMF) was coated on top of the substrate (FTO/TiO_2/ZrO_2/Carbon) by spin coating at 3000 rpm for 30 s for these pore filling, followed by heating at 70 °C for 30 min. Then in second step, the film was dipped in solution of CH_3NH_3I (10 mg/mL in 2-propanol) for 15 min. Finally, the substrate was rinsed with 2-propanol and heated at 70 °C for 30 min. In contrary, for one-step drop-casting method, perovskite precursor solution (5 µL) consisting of PbI_2 and MAI (PbI_2:MAI=1:1, molar ratio, 1.25 M) in γ-butyrolactone was dropped on the top of the carbon electrodes (FTO/TiO_2/ZrO_2/Carbon) and sample was kept in a fume hood for 20 min. Finally, the substrate filled with perovskite precursor was annealed on a hotplate at 50 °C for one

hour. In case of passivation of carbon electrode with PbI_2 layer, the device architecture FTO/TiO_2/ZrO_2/Carbon was dipped in 0.2 mM PbI_2 solution prepared in DMF for 30 minutes at room temperature. In the final step, the device was rinsed with DMF to get rid of loosely bound PbI_2.

2.2.4 Characterization

X-ray photoelectron spectroscopy (XPS) (Kratos Axis-Nova) was employed to determine surface chemical composition. The cross-section of perovskite solar cell device and the top view of carbon electrode were imaged by a field-emission scanning electron microscope (FE-SEM, Jeol JSM 6700F). Photovoltaic performance of the device was measured with a solar simulator (KHP-1, Bunko-Keiki, Japan) equipped with a xenon lamp (XLS-150A). The intensity of light irradiation was confirmed to be 1 SUN (100 $mW \cdot cm^{-2}$). The solar simulator spectrum and its power were adjusted using a spectroradiometer (LS-100, Eiko Seiki, Japan). The exposure power was also corrected with standard amorphous Si photodetector (BS-520 S/N 007, Bunko-Keiki, Japan), which has a similar visible light sensitivity to the PSC. The electrochemical impedance spectrum (EIS) analysis was performed using an electrochemical measurement system (12528WB, Solartron Metrology) in the dark conditions with the frequency ranging from 10^5 to 10^{-1} Hz using perturbation amplitude of 10 mV.

2.3 Results and discussion

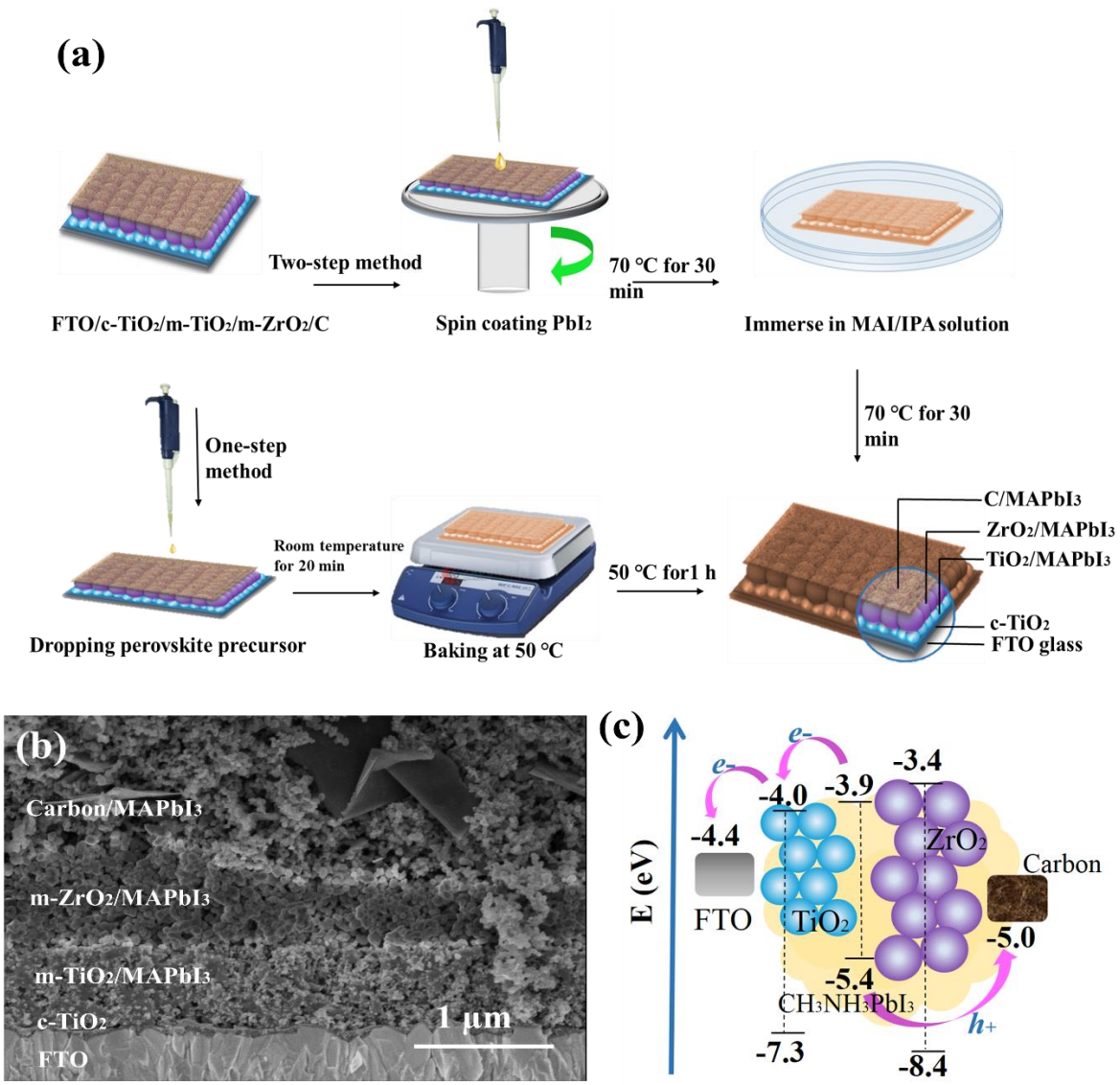

Figure 2-2 (a) Schematic illustration of one-step and two-step process for fabricating perovskite films, and the device structure. (b) Cross-sectional SEM image of the perovskite solar cell device. (c) Energy level of each layer in the device.

The cross-sectional image showing the thickness of different layers of the device is displayed in Figure 2-2(b). The solar cell consists of an ~800 nm thick mesoporous TiO_2 layer and a ~700 nm thick mesoporous ZrO_2 layer prepared on the top of c-TiO_2 by the spin coating

method. As represented in Figure 2-2(c) by energy diagram of different components of the solar cells, the perovskite layer acts as an absorber layer. Firstly, electrons in LUMO energy level are transferred to TiO_2 layer and finally to conducting FTO glass. The c-TiO_2 layer coated on FTO glass helps to avoid the charge recombination between electrons in FTO and holes in HOMO (PVK). Mesoporous ZrO_2 avoids direct contact between meso-porous TiO_2 and carbon, physically. As the contact between TiO_2 and carbon electrode should be avoided to reduce the recombinations, hence an optimized thickness of m-ZrO_2 is required which plays the role of an insulator layer.

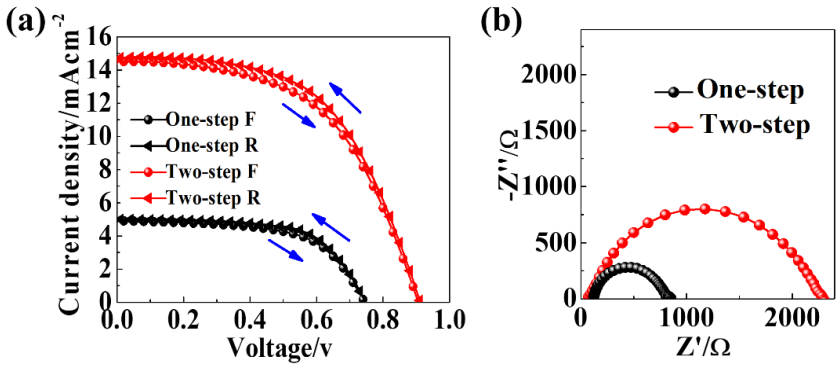

Figure 2-3 (a) J-V and (b) EIS curves of carbon based perovskite solar cells fabricated by one-step and two-step.

Figure 2-3(a) shows the current-voltage characteristics of carbon based perovskite solar cells prepared by one-step and two-step method in this work. The solar cells fabricated by using the one-step method exhibited a low PCE of 2.21%, with J_{sc}, V_{oc} and FF values of 4.91 $mA \cdot cm^{-2}$, 0.74 V, and 0.60 respectively. This low performance can be attributed to the poor pore-filling and coverage of the perovskite layer formed, which is common and well known issue in conventional PSCs employing one-step method without anti-solvent approach.[44-45] And as expected a two-step method improves the pore-filling and surface coverage, due to which the

device displayed a higher PCE of 7.08%. The J_{sc} and V_{oc} were drastically increased to 14.51 $mA \cdot cm^{-2}$ and 0.91 V, which is clear indication of increased absorption and reduced recombination in case of two-step method. However, regardless of the perovskite solar cell device prepared by the one-step method or the two-step method, the fill factor is not high. This can be attributed to the large electrical resistance offered because of the thick layers of TiO_2/ZrO_2 scaffold of our solar cell, as seen through SEM image (Figure 2-2b), which exceeds the diffusion length of photogenerated charge carriers resulting in trap/recombination centers[46-48] and contributes in carrier non-radiative recombination.[49-51] It was mentioned earlier that charge recombination occurs between carbon electrode and TiO_2 layers because of direct contact. However, it is an important observation in the work that recombination can additionally be originated from direct contact of carbon electrode and perovskite absorber layers, because of the holes in carbon electrode with the excited electrons in conduction band (CB) of perovskite absorber. In case of two-step deposition, an initial coating of PbI_2 might be helpful in separating the carbon and perovskite layers which inhibits the recombination, thereby improving solar cell performance. This observation was also confirmed from EIS results under dark, the Nyquist plot (Figure 2-3b) shows the typical semicircle in high frequency. The arc is related to charge carrier recombination involved in device. And it strongly confirms that the two-step solar cells exhibit higher recombination resistance, which as a consequence increases the solar cell performance. It has been already reported that passivation using PbI_2 on the porous TiO_2 improves the photovoltaic parameters in PSCs based on metal electrode (Ag or Au).[35] The presence of thin PbI_2 layer on carbon surface has also been noticed to improve the stability of PSCs owing to the blockage of H_2O insertion into the perovskite crystals.[52] However, its role on changing the photovoltaic characteristics was not discussed. Hence, it becomes very interesting to know the

passivation effect of PbI_2 on carbon surface to improve the photovoltaic properties of PSCs as well.

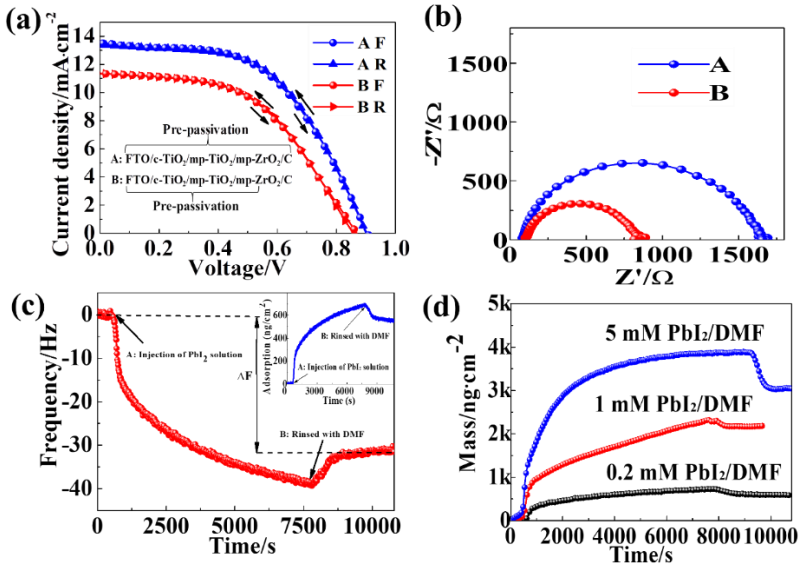

Figure 2-4 (a) J-V and (b) EIS curves of carbon based perovskite solar cells consisting of structure A and B by one-step mothed. (c) Relationship between relative frequency of carbon sensor and adsorption time. (inset) Relationship between PbI_2 adsorption density on carbon and adsorption time. The concentration of PbI_2/DMF is 0.2 mM. (d) PbI_2 adsorption density under different concentration PbI_2/DMF solution.

To clarify the effect of PbI_2 coating on carbon, two kinds of solar cell architectures, A and B were fabricated (see Figure 2-4a), with and without PbI_2 passivation respectively. For structure B, we infiltrated PbI_2 on FTO/c-TiO_2/mp-TiO_2/mp-ZrO_2 substrates, and then, carbon electrode was coated on the sample, where, the carbon surface did not have opportunity to contact directly with the PbI_2. Finally, a precursor solution consisting of MAI and PbI_2 was infiltrated in nanopores of the triple layer. In this structure, the carbon surface was not coated by PbI_2 (Structure B: FTO/c-TiO_2/mp-TiO_2(Pb)(PVK)/mp-ZrO_2(Pb)(PVK)/mp-C(PVK)), where (Pb)

stands for porous layers with surface passivation of PbI_2. Structure A (FTO/c-TiO_2/mp-TiO_2(Pb)(PVK)/mp-ZrO_2(Pb)(PVK)/mp-C(Pb)(PVK) was prepared similar to the architecture utilized in case of one-step method as shown in Figure 2-2 (a), but with PbI_2 coating on each layer, which was absent in previous case. Therefore in structure A, mp-TiO_2/mp-ZrO_2/mp-Carbon pores were passivated with PbI_2 and then mp-TiO_2(Pb)/mp-ZrO_2(Pb)/mp-Carbon pores(Pb) were filled with a precursor solution consisting of MAI and PbI_2. Solar cells based on architecture A, where all of the porous surfaces consisting of TiO_2/ZrO_2/C was covered by PbI_2, exhibited better performance than solar cell B. This confirms the role of PbI_2 passivation on carbon electrode in avoiding the direct contact between the carbon and perovskite absorber layers, which as a result improved the PCE in structure A compared to structure B. Here, it is important to mention that one-step method to prepare solar cells without any pretreatment of PbI_2 gave an efficiency of 2.21% (Figure 2-3). After passivation with PbI_2, as shown in Figure 2-4 (a), efficiency improved to 4.97% for Structure B, and 6.55% for Structure A. This further shows that PbI_2 passivation is beneficial, not only on mp-TiO_2, but also on mp-carbon to improve solar cell performance. It is worth noting that the two-step method can form a passivation layer before the perovskite formation, so pre-passivation before one-step method should be same as that in two-step method. To further investigate the charge transport process in the devices and role of PbI_2 passivation, EIS were measured for Structure A and B. The EIS was measured under dark condition at an applied bias (0.6 v) in the frequency range from 10^5 to 10^{-1} Hz. As shown in Figure 2-4 (b), one typical arc in Nyquist plots, and this arc could be related to the overall charge transport in the cells.[24] It is found that device A has greater charge recombination resistance than device B. This could be attributed to the pre-passivation of the carbon electrode, which reduces the charge recombination rate occurring between carbon and perovskite layers.

QCM analysis was done to further investigate the surface chemistry of carbon layer which was affecting the different devices fabricated. Figure 2-4 (c) shows the relative frequency of carbon sensor in real time monitored by quartz crystal microbalance (QCM). The PbI_2 solution was introduced to the carbon sensor surface at point A in Figure 2-4 (c), resulting in a decrease in frequency until equilibrium was reached. With the increase of adsorption time, the frequency is getting lower and lower, but the rate of frequency decrease is becoming slower. The sensors were then rinsed with DMF solution at point B in Figure 2-4 (c) to remove weakly bound PbI_2 molecules from the carbon sensor surface. During the rinse process, the weakly bound PbI_2 molecules were desorbed from the carbon sensor surface. Therefore, from the point B, the relative frequency starts to rise again and tended to be stable finally. The frequency drop ΔF in Figure 2-4 (c) represents the strongly bound PbI_2. After weakly bound PbI_2 was removed, the amount of strongly bound PbI_2 to the carbon sensor surface can be calculated by use of the Sauerbrey equation. The inset figure of Figure 2-4 (c) shows the relationship between the adsorption time and PbI_2 adsorption density on carbon sensor, calculated from Figure 2-4 (c) by Sauerbrey equation. It can be seen intuitively that the weight of the carbon layer increased with time, demonstrating that PbI_2 was adsorbed on the carbon layer.

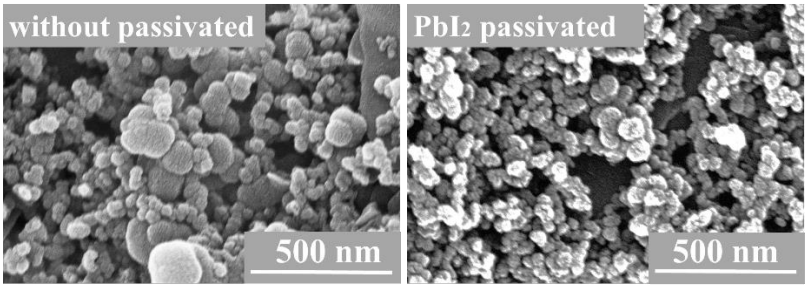

Figure 2-5. FESEM images of carbon electrode before and after passivated by PbI_2.

As shown in Figure 2-4 (d) the maximum PbI_2 adsorption density increased with the increase of concentration of PbI_2/DMF solution. The SEM image of the carbon electrode is shown in Figure 2-5 we can see there is almost no change in morphology before and after passivation. In order to further study the effect of different PbI_2/DMF concentration on the carbon surface passivation, the EIS curves of devices after passivation with the different PbI_2/DMF solution are shown in Figure 2-6. EIS plot suggests that increase in concentration resulted in increased recombination resistance, which is the signature of more coverage of carbon surface with the increased concentration. When the solution concentration was greater than 5 mM, the carbon surface was completely covered by PbI_2 molecules. The diameter of PbI_2 molecule ranges from 0.558 to 0.954 nm. When the PbI_2 molecule is adsorbed on the plane surface, the smallest area occupied by PbI_2 is 2.45×10^{-15} to 7.15×10^{-15} cm^2. When PbI_2 molecules completely cover the planar substrate, the adsorption density of PbI_2 is about 107 to 313 $ng\cdot cm^{-2}$. In this work, the carbon sensor has a thickness of ~ 106 nm, consisting of carbon particle with diameter of ~ 30 nm. So carbon sensor covered by three or four layers of carbon particles. If all of the carbon particles surface is covered by PbI_2 molecules, the PbI_2 adsorption density could be calculated to be 1498 to 4382 $ng\cdot cm^{-2}$. The PbI_2/DMF solution with a concentration of 5 mM, can eventually reach saturation absorption of ~ 3000 $ng\cdot cm^{-2}$. This was concurrent with the calculated value. Therefore, the 1 M PbI_2/DMF in this work is sufficient to achieve the saturated adsorption of the carbon electrode surface.

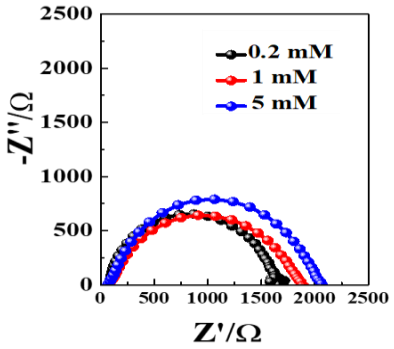

Figure 2-6 EIS curves of devices after passivation with different concertation of PbI_2/DMF solution.

Figure 2-7 (a) is the XPS full scan comparisons of PbI_2-adsorbed carbon film before and after rinsing with DMF (the blue and the red curves). Peaks at 619.0 and 630.8 eV are assigned to I 3d5/2 and I 3d3/2, respectively. Peaks at 139.2 and 144.0 eV are assigned to Pb 4f7/2 and Pb 4f5/2, respectively. After rinsing with DMF, we can see that C, O, Pb and I still existed in the sample, indicating that the strongly bound PbI_2 cannot be removed from the carbon surface even when rinsed with DMF which is also consistent with the QCM results. XPS spectra of carbon for the reference is also shown in Figure 2-7 (a) (the black curve). The full scan of carbon film shows that there are no obvious other elements except C and O. The peak of O is located at 532.8 eV, which can be attributed to the -OH of the carbon surface.[53] -OH is a very reactive group that readily reacts with PbI_2 and produces HI and C-O-Pb bonds, as shown in Figure 2-7 (c). The XPS spectra of Pb 4f for perovskite Pb layer and PbI_2 layer is shown in Figure 2-7 (b). Before rinsing with DMF, the peak of Pb 4f7/2 for bulk perovskite Pb layer and PbI_2 layer were observed at 138.4 and 138.6 eV, respectively. After rinsing with DMF, the Pb 4f7/2 peaks shift to higher binding energy location (from 138.4 to 139.17 eV for perovskite Pb; from 138.6 to 139.2 eV for PbI_2). This suggests that C-O-Pb linkages are formed at the C/perovskite interface.

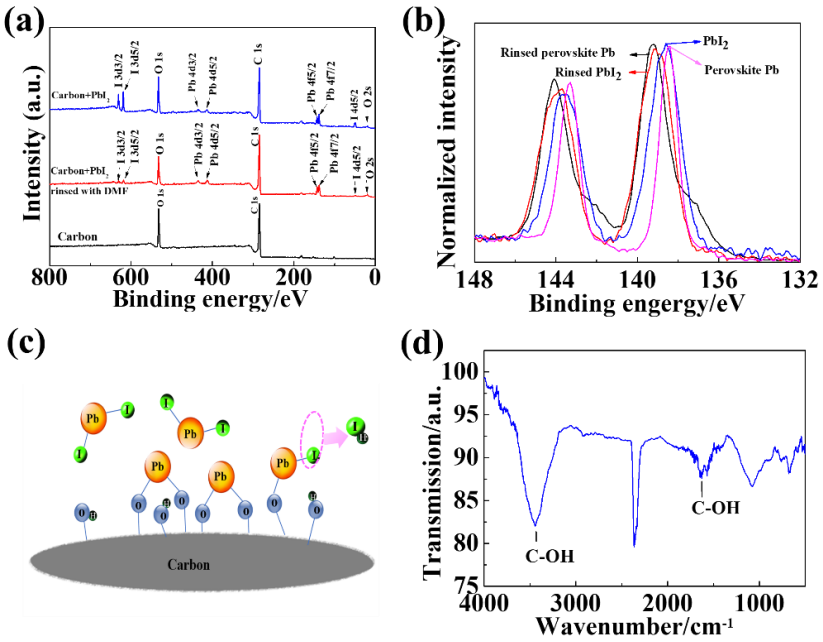

Figure 2-7 (a) XPS full scan of carbon film and PbI_2-adsorbed carbon film, (b) High-resolution XPS spectra of Pb adsorbed on carbon surface (spectra of Pb 4f7/2 and Pb 4f5/2). (c) Expected reaction process of -OH on the carbon surface and PbI_2. (d) FTIR spectra of carbon powder. Carbon paste was screen printed on glass substrate and then baked at 100℃ for 10 min, carbon powder was scratched after cooling the substrate to room temperature. The baseline of the spectra is shifted for better visualization.

FTIR is an effective method to characterize the chemical composition of carbon surface. FTIR spectra is shown in Figure 2-7 (d). It is clear that the C-OH stretching mode can be found at around 3445 cm^{-1} and their bending mode sround1630 cm^{-1}. Therefore, we can assume that -OH group as the binding site of Pb is present on the carbon surface.

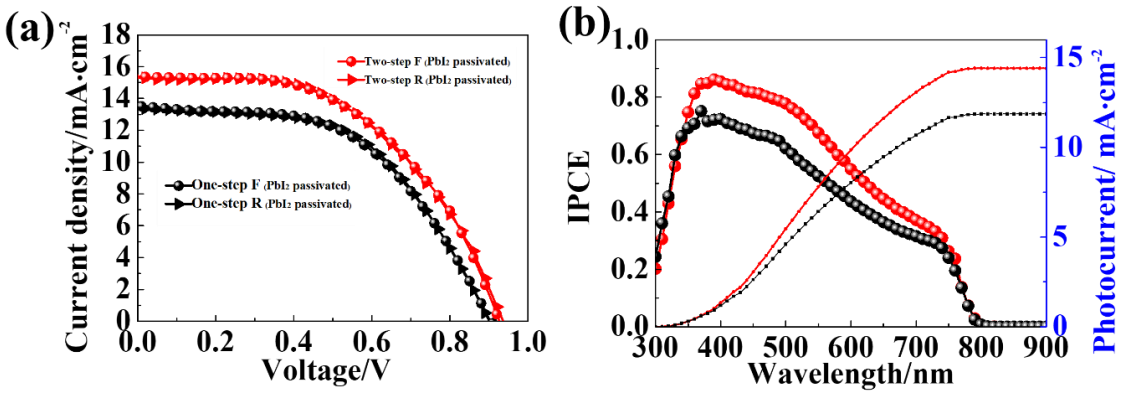

Figure 2-8 (a) J-V and (b) IPCE curves of pre-passivated carbon based perovskite solar cells fabrication by one-step and two-step mothed.

It is interesting that C-O-Pb linkage on carbon, which is playing the role of protecting layer to reduce the recombination can't be removed after rinsing with DMF as well. Therefore, finally, solar cells were prepared to see the difference in performance by one-step and two-step method with the PbI_2 passivation, J-V and IPCE curves as shown in Figure 2-8 (a) and (b), structure A (FTO/c-TiO_2/mp-TiO_2(Pb) /mp-ZrO_2(Pb)/mp-C(Pb) was employed in both cases. At first, PbI_2 was deposited on all porous layers, mp-TiO_2(Pb)/mp-ZrO_2(Pb)/mp-Carbon pores(Pb), secondly, PbI_2 layer was rinsed and then, perovskite was coated. The device prepared by two-step method displayed PCE of 7.30%, which is better than solar cells without PbI_2 passivation (7.08%). The enhanced J_{sc} of 15.32 mA·cm^{-2} (integrated value of 14.41 mA·cm^{-2}) and V_{oc} of 0.93 V were the direct effect of passivation of carbon electrode with C-O-Pb formation. The solar cell prepared by one-step resulted in the PCE of 6.55% with Jsc of 13.38 mA·cm^{-2} (integrated value of 11.86 mA·cm^{-2}), V_{oc} of 0.90 V, and a FF of 0.54, which is still lower than two-step technique; however, passivation effect by C-O-Pb is prominent in one-step as well.

2.4 Conclusions

In summary, carbon based perovskite solar cells by one-step and two-step methods were fabricated. As a result, a PCE of 7.08% with two-step method was attained, better than one-step method (2.21%). Furthermore, a novel analysis method using QCM was reported, which is an effective technology to monitor the change of carbon electrode surface in carbon based PSCs. The results obtained from QCM demonstrate that PbI_2 loaded on the carbon surface can't be removed even after rinsing with solvent (DMF), the remnants were C-O-Pb linkages bonded covalently as confirmed from XPS and FTIR. It has been proven that passivation of carbon electrode is necessary to enhance the PCE, by reducing the recombination due to direct contact with absorber layer. The passivation using C-O-Pb was finally utilized successfully in fabricating the solar cells with improved PCE of 7.30% and 6.55%, employing two-step and one-step fabrication methods respectively.

2.5 References

[1] A. Kojima; Teshima, K.; Shirai, Y.; Miyasaka, T., J. Am. Chem. Soc. 131 (2009) 6050-6051.

[2] W.S. Yang; Park, B.-W.; Jung, E.H.; Jeon, N.J.; Kim, Y.C.; Lee, D.U.; Shin, S.S.; Seo, J.; Kim, E.K.; Noh, J.H., Science 356 (2017) 1376-1379.

[3] Y. Du; Cai, H.; Bao, X.; Xing, Z.; Wu, Y.; Xu, J.; Huang, L.; Ni, J.; Li, J.; Zhang, J., ACS Sustainable Chemistry & Engineering 6 (2017) 1083-1090.

[4] L. Xu; Liu, H.; Qiu, W.; Xue, K.; Liu, X.; Wang, J.; Zhang, H.; Huang, W., ACS Sustainable Chemistry & Engineering 5 (2017) 9718-9724.

[5] J.Y. Seo; Uchida, R.; Kim, H.S.; Saygili, Y.; Luo, J.; Moore, C.; Kerrod, J.; Wagstaff, A.; Eklund, M.; Mcintyre, R., Adv. Funct. Mater. 28 (2018) 1705763.

[6] K. Rakstys; Saliba, M.; Gao, P.; Gratia, P.; Kamarauskas, E.; Paek, S.; Jankauskas, V.; Nazeeruddin, M.K., Angew. Chem. 128 (2016) 7590-7594.

[7] Y. Liang; Wang, Y.; Mu, C.; Wang, S.; Wang, X.; Xu, D.; Sun, L., Advanced Energy Materials 8 (2018) 1701159.

[8] W. Wei; Hu, Y.H., Journal of Materials Chemistry A 5 (2017) 24126-24130.

[9] C.-M. Tsai; Wu, G.-W.; Narra, S.; Chang, H.-M.; Mohanta, N.; Wu, H.-P.; Wang, C.-L.; Diau, E.W.-G., Journal of Materials Chemistry A 5 (2017) 739-747.

[10] J.A. Christians; Schulz, P.; Tinkham, J.S.; Schloemer, T.H.; Harvey, S.P.; De Villers, B.J.T.; Sellinger, A.; Berry, J.J.; Luther, J.M., Nature Energy 3 (2018) 68.

[11] G.W. Kim; Lee, J.; Kang, G.; Kim, T.; Park, T., Advanced Energy Materials 8 (2018) 1870018.

[12] J. You; Meng, L.; Song, T.-B.; Guo, T.-F.; Yang, Y.M.; Chang, W.-H.; Hong, Z.; Chen, H.; Zhou, H.; Chen, Q., Nature nanotechnology 11 (2016) 75.

[13] F. Zhang; Wang, Z.; Zhu, H.; Pellet, N.; Luo, J.; Yi, C.; Liu, X.; Liu, H.; Wang, S.; Li, X., Nano Energy 41 (2017) 469-475.

[14] J. Zhang; Xu, B.; Yang, L.; Ruan, C.; Wang, L.; Liu, P.; Zhang, W.; Vlachopoulos, N.; Kloo, L.; Boschloo, G., Advanced Energy Materials 8 (2018) 1701209.

[15] P. Qin; Tanaka, S.; Ito, S.; Tetreault, N.; Manabe, K.; Nishino, H.; Nazeeruddin, M.K.; Grätzel, M., Nature communications 5 (2014) 3834.

[16] K. Rakstys; Paek, S.; Gao, P.; Gratia, P.; Marszalek, T.; Grancini, G.; Cho, K.T.; Genevicius, K.; Jankauskas, V.; Pisula, W., Journal of Materials Chemistry A 5 (2017) 7811-7815.

[17] J.-J. Guo; Bai, Z.-C.; Meng, X.-F.; Sun, M.-M.; Song, J.-H.; Shen, Z.-S.; Ma, N.; Chen, Z.-L.; Zhang, F., Solar Energy 155 (2017) 121-129.

[18] J.H. Kim; Liang, P.W.; Williams, S.T.; Cho, N.; Chueh, C.C.; Glaz, M.S.; Ginger, D.S.; Jen, A.K.Y., Adv. Mater. 27 (2015) 695-701.

[19] J. Chen; Rong, Y.; Mei, A.; Xiong, Y.; Liu, T.; Sheng, Y.; Jiang, P.; Hong, L.; Guan, Y.; Zhu, X., Advanced Energy Materials 6 (2016) 1502009.

[20] H. Zhang; Wang, H.; Williams, S.T.; Xiong, D.; Zhang, W.; Chueh, C.C.; Chen, W.; Jen, A.K.Y., Adv. Mater. 29 (2017) 1606608.

[21] L. Liu; Mei, A.; Liu, T.; Jiang, P.; Sheng, Y.; Zhang, L.; Han, H., J. Am. Chem. Soc. 137 (2015) 1790-1793.

[22] L. Chu; Zhang, J.; Liu, W.; Zhang, R.; Yang, J.; Hu, R.; Li, X.a.; Huang, W., ACS Sustainable Chemistry & Engineering 6 (2018) 5588-5597.

[23] L. Wagner; Chacko, S.; Mathiazhagan, G.; Mastroianni, S.; Hinsch, A., ACS Energy Letters 3 (2018) 1122-1127.

[24] H. Wei; Xiao, J.; Yang, Y.; Lv, S.; Shi, J.; Xu, X.; Dong, J.; Luo, Y.; Li, D.; Meng, Q., Carbon 93 (2015) 861-868.

[25] Q. Luo; Ma, H.; Hou, Q.; Li, Y.; Ren, J.; Dai, X.; Yao, Z.; Zhou, Y.; Xiang, L.; Du, H., Adv. Funct. Mater. 28 (2018) 1706777.

[26] Z. Wei; Chen, H.; Yan, K.; Yang, S., Angew. Chem. Int. Ed. 53 (2014) 13239-13243.

[27] R. Hu; Chu, L.; Zhang, J.; Li, X.a.; Huang, W., J. Power Sources 361 (2017) 259-275.

[28] H. Chen; Wei, Z.; He, H.; Zheng, X.; Wong, K.S.; Yang, S., Advanced Energy Materials 6 (2016) 1502087.

[29] H. Zhou; Shi, Y.; Dong, Q.; Zhang, H.; Xing, Y.; Wang, K.; Du, Y.; Ma, T., The journal of physical chemistry letters 5 (2014) 3241-3246.

[30] H. Sung; Ahn, N.; Jang, M.S.; Lee, J.K.; Yoon, H.; Park, N.G.; Choi, M., Advanced Energy Materials 6 (2016).

[31] Q.-Q. Chu; Ding, B.; Li, Y.; Gao, L.L.; Qiu, Q.; Li, C.-X.; Li, C.-J.; Yang, G.-J.; Fang, B., ACS Sustainable Chemistry & Engineering 5 (2017) 9758-9765.

[32] A. Mei; Li, X.; Liu, L.; Ku, Z.; Liu, T.; Rong, Y.; Xu, M.; Hu, M.; Chen, J.; Yang, Y., Science 345 (2014) 295-298.

[33] V. Kapoor; Bashir, A.; Haur, L.J.; Bruno, A.; Shukla, S.; Priyadarshi, A.; Mathews, N.; Mhaisalkar, S., Energy Technology 5 (2017) 1880-1886.

[34] J. Ryu; Lee, K.; Yun, J.; Yu, H.; Lee, J.; Jang, J., Small 13 (2017) 1701225.

[35] S. Nakayashiki; Daisuke, H.; Ogomi, Y.; Hayase, S., Journal of Photonics for Energy 5 (2015) 057410.

[36] H. Tan; Jain, A.; Voznyy, O.; Lan, X.; De Arquer, F.P.G.; Fan, J.Z.; Quintero-Bermudez, R.; Yuan, M.; Zhang, B.; Zhao, Y., Science 355 (2017) 722-726.

[37] Q. Chen; Zhou, H.; Song, T.-B.; Luo, S.; Hong, Z.; Duan, H.-S.; Dou, L.; Liu, Y.; Yang, Y., Nano Lett. 14 (2014) 4158-4163.

[38] Y. Wu; Xie, F.; Chen, H.; Yang, X.; Su, H.; Cai, M.; Zhou, Z.; Noda, T.; Han, L., Adv. Mater. 29 (2017) 1701073.

[39] J. Carrillo; Guerrero, A.; Rahimnejad, S.; Almora, O.; Zarazua, I.; Mas-Marza, E.; Bisquert, J.; Garcia-Belmonte, G., Advanced Energy Materials 6 (2016) 1502246.

[40] K.K. Kanazawa; Gordon, J.G., Anal. Chem. 57 (1985) 1770-1771.

[41] H.K. Wayment-Steele; Johnson, L.E.; Tian, F.; Dixon, M.C.; Benz, L.; Johal, M.S., ACS applied materials & interfaces 6 (2014) 9093-9099.

[42] Z. Hu; Kapil, G.; Shimazaki, H.; Pandey, S.S.; Ma, T.; Hayase, S., The Journal of Physical Chemistry C 121 (2017) 4214-4219.

[43] J. Burschka; Pellet, N.; Moon, S.-J.; Humphry-Baker, R.; Gao, P.; Nazeeruddin, M.K.; Grätzel, M., Nature 499 (2013) 316.

[44] N.J. Jeon; Lee, J.; Noh, J.H.; Nazeeruddin, M.K.; GräTzel, M.; Seok, S.I., J. Am. Chem. Soc. 135 (2013) 19087-19090.

[45] J.-H. Im; Kim, H.-S.; Park, N.-G., Apl. Materials 2 (2014) 081510.

[46] P.L. Qin; Yang, G.; Ren, Z.w.; Cheung, S.H.; So, S.K.; Chen, L.; Hao, J.; Hou, J.; Li, G., Adv. Mater. 30 (2018) 1706126.

[47] M. Jahandar; Khan, N.; Lee, H.K.; Lee, S.K.; Shin, W.S.; Lee, J.-C.; Song, C.E.; Moon, S.-J., ACS applied materials & interfaces 9 (2017) 35871-35879.

[48] N.K. Noel; Abate, A.; Stranks, S.D.; Parrott, E.S.; Burlakov, V.M.; Goriely, A.; Snaith, H.J., ACS nano 8 (2014) 9815-9821.

[49] C. Han; Yu, H.; Duan, J.; Lu, K.; Zhang, J.; Shao, M.; Hu, B., Journal of Materials Chemistry C 6 (2018) 6164-6171.

[50] G.J.A. Wetzelaer; Scheepers, M.; Sempere, A.M.; Momblona, C.; vila, J.; Bolink, H.J., Adv. Mater. 27 (2015) 1837-1841.

[51] D.-Y. Son; Lee, J.-W.; Choi, Y.J.; Jang, I.-H.; Lee, S.; Yoo, P.J.; Shin, H.; Ahn, N.; Choi, M.; Kim, D., Nature Energy 1 (2016) 16081.

[52] P. Zhang; Kapil, G.; Hamada, K.; Pandey, S.S.; Ma, T.; Hayase, S., ACS Sustainable Chemistry & Engineering 6 (2018) 10221-10228.

[53] C. Kozlowski; Sherwood, P.M., Journal of the Chemical Society, Faraday Transactions 1: Physical Chemistry in Condensed Phases 81 (1985) 2745-2756.

Chapter 3. Performance enhancement of mesoporous TiO_2-based perovskite solar cells by SbI_3 interfacial modification layer

3.1 Introduction

Perovskite solar cells (PSCs) have gained considerable attention in the recent years due to their unique optoelectronic properties such as tunable band gap in the visible range, high absorption coefficient, high charge carrier mobility, long charge carrier lifetime and large charge carrier diffusion length.[1-4] For these reasons, the power conversion efficiency (PCE) of PSCs has been improved tremendously from initially 3.8% to over 22.7% within the past few years by optimizing the solar cell structures and perovskite film deposition methods, tuning perovskite compositions, improving interface quality or reducing interface defects.[5-6] The high efficiency is almost approaching that of commercial silicon solar cells or other inorganic thin film solar cells such as copper indium gallium selenide (CIGS) and cadmium telluride (CdTe) solar cells. Although PSCs have achieved impressive PCE values, some key issues such as long-term stability, hysteresis behavior and cost of production still exist in the generally fabricated PSCs. The decay of device performance in ambient air condition is a great hurdle for the commercialization of PSCs. The phenomenon of hysteresis in PSCs is caused by interface defects, ion migration or ferroelectric effect etc..[7-8] In order to improve the performance of PSCs, the hysteresis issue needs to be resolved to ensure a reliable performance.

In the perovskite photovoltaic devices, cells with mesoporous structure (Cell 1)[9] and that with planar structures (Cell 2)[10] have been reported. Cell 1 has semiconductor or insulator

nanoparticles as a scaffold layer. There is a large number of voids in the scaffold layer. The perovskite precursor solution can easily penetrate into the interstices of the scaffold layer and finally forms a continuous perovskite layer in the interface of the scaffold layer. Cell 2 does not need the mesoporous layer and form a sandwich structure with the p-type and n-type semiconductor. In addition, there are some new structures such as inverted structure, a hole transporting layer free structure, an electron transporting layer free structure. In all of these structures, a device with mesoporous structure has the best repeatability and the highest solar cell efficiency so far.[6] In Cell 1, researchers modified the electron transport layer in various ways in order to get more excellent performance. In the case of mesoporous TiO_2 (mp-TiO_2) based PSCs, a variety of dopants has been investigated, including Al,[11] Co,[12] Li,[13-15] Mg,[16] K,[17] Ru,[18] Nb,[19] Y,[20] and other additives.[21] Various interfacial modifiers have also been studied including organic molecules,[22-23] metal oxides[24] other materials.[25-26] However, little attention has been paid to the passivation of TiO_2 by SbI_3 and how it binds to TiO_2.

In this work, we adopted a simple immersion method to form a SbI_3 passivation layer on the surface of TiO_2. Quartz crystal microbalance system (QCM) was used to monitor the binding of SbI_3 molecules to TiO_2 surface groups. It has been shown that SbI_3 monolayer on TiO_2 surface can be formed utilizing the simple immersion of the TiO_2 substrate, which not only reduces TiO_2 surface defects but also improves the morphology of the $CH_3NH_3PbI_3$ perovskite film. The results show that hysteresis is significantly reduced, and the long-term stability in the air environment is greatly improved after the SbI_3 passivation. A high device performance of 17.33% (16.41%, average) and enhanced device stability was achieved, compared to those of devices without the passivation (champion 15.82%, average 15.04%).

3.2 Experiment section

3.2.1 Device fabrication.

Firstly, fluorine-doped tin oxide (FTO) glass (Nippon Sheet Glass Co. Ltd.) was cut into pieces with dimensions of 20 mm × 20 mm and etched with zinc powder and hydrochloric acid solution (6 M). Then the substrates were washed with detergent, acetone, isopropanol and deionized water for 15 min, respectively under ultrasonic condition. Then the substrates were dried with air and treated with oxygen plasma for 10 min. To prepare a TiO_2 compact layer (c-TiO_2), 0.15 M titanium diisopropoxide bis (acetylacetonate) (75 wt% in isopropanol, Sigma-Aldrich) in 1-butanol (99.8%, Sigma-Aldrich) solution was spin-coated on an FTO substrate at 2000 rpm for 20 s, which was followed by heating on a hotplate at 125 °C for 5 min[27]. After cooling down to room temperature, the diluted-TiO_2 paste was spin-coated on the c-TiO_2 layer at 5000 rpm for 30 s, where the paste was diluted in ethanol (TiO_2 paste/ethanol = 1/ 4, weight ratio). After drying on the hotplate at 125 °C for 5 min, the film was annealed at 500 °C for 1 h, providing a mesoporous TiO_2 (mp-TiO_2) with a thickness of 150~200 nm. The SbI_3 passivation layer was then introduced on the mp-TiO_2 surface by immersion the substrates into a 0.2 mM of SbI_3/DMF solution for 30 min, followed by rinsing the film with DMF solution and then drying with air. Light harvesting layer, $CH_3NH_3PbI_3$, was prepared using the one-step anti-solvent method. 1.5 M of perovskite precursor solution was prepared by using methylammonium iodide (MAI, 477 mg) and lead iodide (PbI_2, 1452 mg) dissolved in a binary solution of N, N-dimethylformamide (DMF, 1.6 mL) and dimethyl sulfoxide (DMSO, 0.4 mL) and stirring for 1 hour at room temperature. For deposition of perovskite films, the $CH_3NH_3PbI_3$ precursor solution (50 μL) was first dropped onto a TiO_2/SbI_3 coated FTO substrate. The substrate was spun at 4000 rpm for 25 s, and at 4000 rpm for 10 seconds, during which, 500 μL anhydrous ethyl acetate was quickly

dropped onto the center of the substrate. The obtained films were then dried at 65 °C for 1 min and 100 °C for 10 min. The hole-transporting layer was deposited by spin coating 20 μL of 2,2′,7,7′-tetrakis(N,N-di-p-methoxyphenylamine)-9,9-spirobifluorene (spiro-OMeTAD) solution on top of $CH_3NH_3PbI_3$. The spiro-OMeTAD solution was prepared by dissolving 72.3 mg of spiro-OMeTAD in 1 mL of chlorobenzene, to which 28.8 μL of 4-tert-butyl pyridine (4-TBP) and 17.5 μL of lithium bis(trifluoromethanesulfonyl)imide (Li-TFSI) solution (520 mg LI-TSFI in 1 mL acetonitrile) were added. Finally, an 80-nm-thick Au was thermally evaporated on the spiro-OMeTAD-coated film as the cathode. The whole process was carried out in the air environment without using a glove box. Note the following points: (a), the substrate was treated with oxygen plasma before making the perovskite; (b), before spin coating, perovskite precursor solution and spiro-OMeTAD solution were filtered by 0.45 μm PVDF syringe filter; (c), after spin-coating spiro-OMeTAD, the samples were kept in a desiccator overnight and Au electrode was evaporated the next day.

3.2.2 Film characterization.

A field-emission scanning electron microscope (FE-SEM, Jeol JSM 6700F) and a Bruker Innova atomic force microscopy (AFM) (JSPM-5200) were used to investigate the surface morphology of the samples. UV-Vis spectra were obtained using a Shimadzu UV-2550 spectrophotometer. The photoelectron yield spectroscopy (PYS) was used to measure the valence-band maximum (VBM). X-ray diffraction (XRD) experiments were conducted by a Rigaku SmartLab X-ray diffractometer with Cu Kα radiation (λ=1.5418 Å), 45 kV and 200 mA at room temperature. The samples were scanned from 10° to 80° with a step-size of 0.01°.

3.2.3 Device characterization.

Photocurrent and voltage were measured with a solar simulator (KHP-1, Bunko-Keiki, Japan) equipped with a xenon lamp (XLS-150A) and a Keithley 2400 source meter. The intensity of light irradiation was calibrated with a standard amorphous Si photodetector (BS-520 S/N 007, Bunko-Keiki, Japan), and adjusted to simulate the 1 SUN (100 $mW \cdot cm^{-2}$) AM1.5G illumination. The voltage scan rate was 10 $mV \cdot s^{-1}$. The devices were measured after stored for one day in a moisture-free desiccator. These samples were covered with a black metal mask (0.1 cm^2) to define the active area and reduce the influence of the scattered light. The electrochemical impedance spectrum (EIS) analysis was performed using an electrochemical measurement system (12528WB, Solartron Metrology) in the dark conditions with the frequency ranging from 10^5 to 10^{-1} Hz at an applied bias of 0.4, 0.6 and 0.8 V.

3.3 Results and discussion

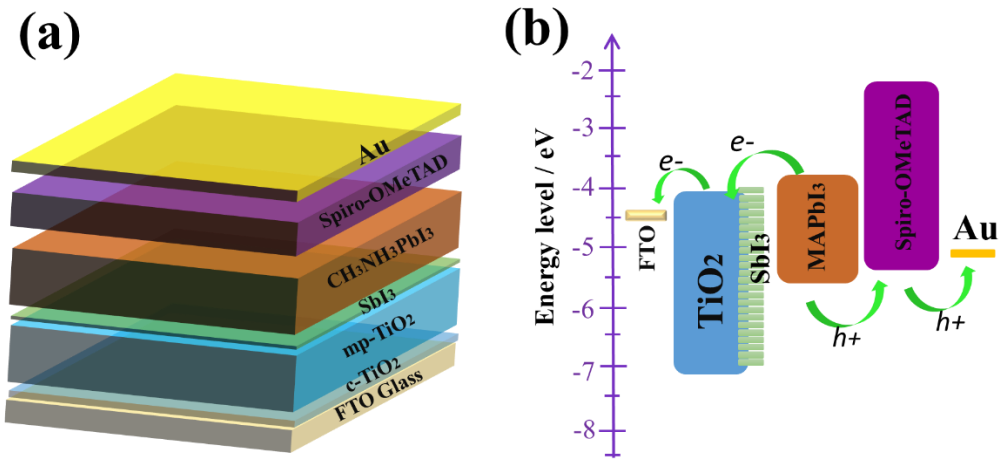

Figure 3-1 The $TiO_2/SbI_3/MAPbI_3$/spiro-OMeTAD/Au solar cell: (a) the device structure, and (b) the energy band diagram.

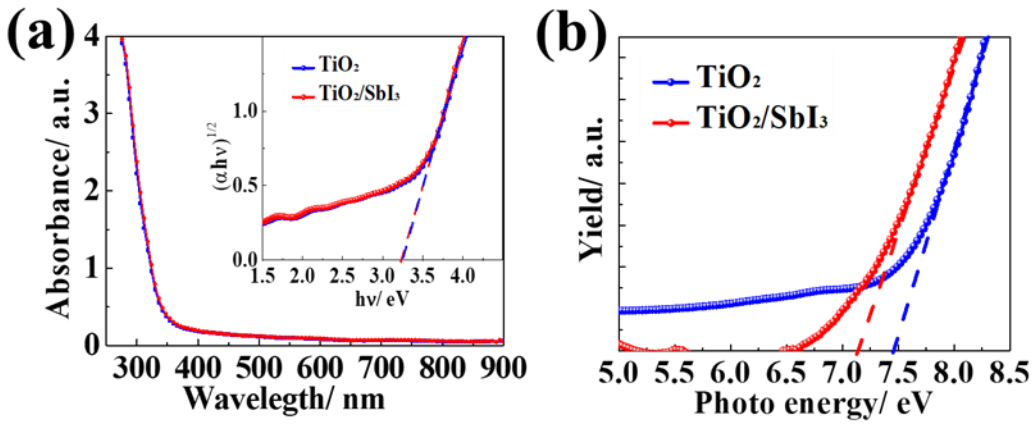

Figure 3-2 (a) UV-visible absorption and (b) photoelectron yield (PY) spectra of the TiO_2 and TiO_2/SbI_3 films. Inset figure, the Tauc plot of band gap for TiO_2 and TiO_2/SbI_3 films.

The architecture of the prepared TiO_2/SbI_3-based perovskite solar cell, as illustrated in Figure 3-1a, is FTO/c-TiO_2/m-TiO_2/SbI_3/$MAPbI_3$/spiro-OMeTAD/Au. The thin passivation layer, SbI_3, was introduced onto the TiO_2 surface by immersing TiO_2 film into SbI_3/DMF solution. It is expected that the SbI_3 thin layer can effectively passivate TiO_2 to reduce surface defects, and reduce electron-hole recombination which takes place at TiO_2 surface. The light absorption and valence-band maximum of TiO_2 and TiO_2/SbI_3 were measured by using a UV-vis spectrophotometer and photoelectron yield spectroscopy, as shown in Figure 3-2. It is evident from the UV-Vis result that the surface passivation by SbI_3 does not affect the absorption of the TiO_2. The band gap, Eg determined from the UV-Vis spectra also showed no change before and after SbI_3 passivation suggesting that the surface of TiO_2 is passivated by a monolayer SbI_3 (3.20 eV, see inset figure in Figure 3-2a). However, from the PYS measurement, passivating the TiO_2 surface with SbI_3 reduces the VBM from -7.45 eV to -7.13 eV (Figure 3-2b). The reason for the lower VBM in the case of SbI_3 passivation is due to the lower VBM and Eg in the case of Sb_2O_3 and SbI_3.[28-29] The working mechanism of PYS is based on the photoelectric effect and thus

the measurement is very sensitive to the surface condition of the sample, therefore passivation with a monolayer resulted in different values as shown in Figure 3-2b. Figure 3-1b shows the schematic energy level diagram of the device. In this configuration, based on the matching energy level of each layer in the device components, the electrons and holes originated from $MAPbI_3$ perovskite can be easily be injected into TiO_2 and spiro-OMeTAD, respectively.

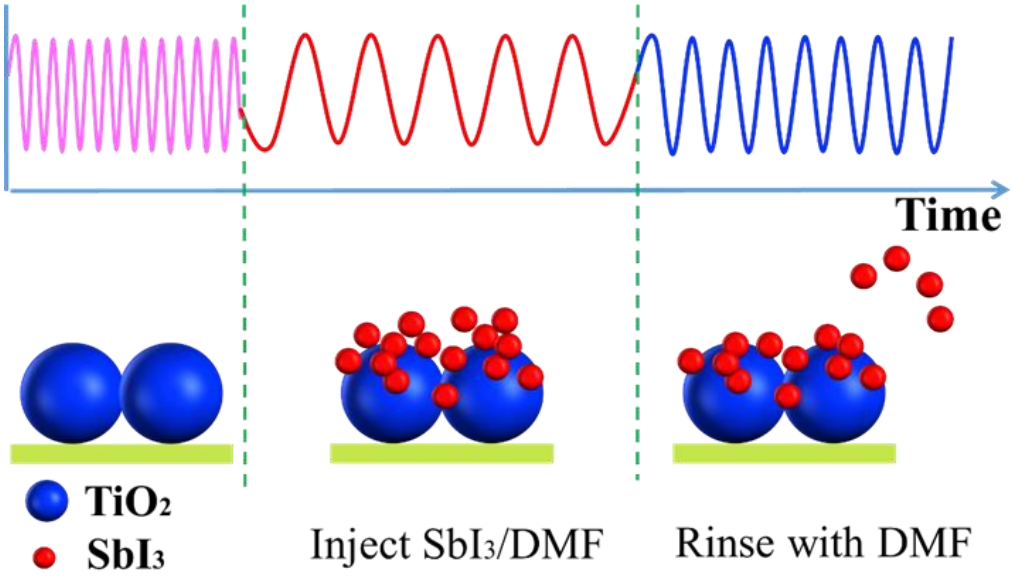

Figure 3-3 Schematic diagram of adsorption and rinsing process of SbI_3 on TiO_2 surfaces and the change in the vibrational frequency.

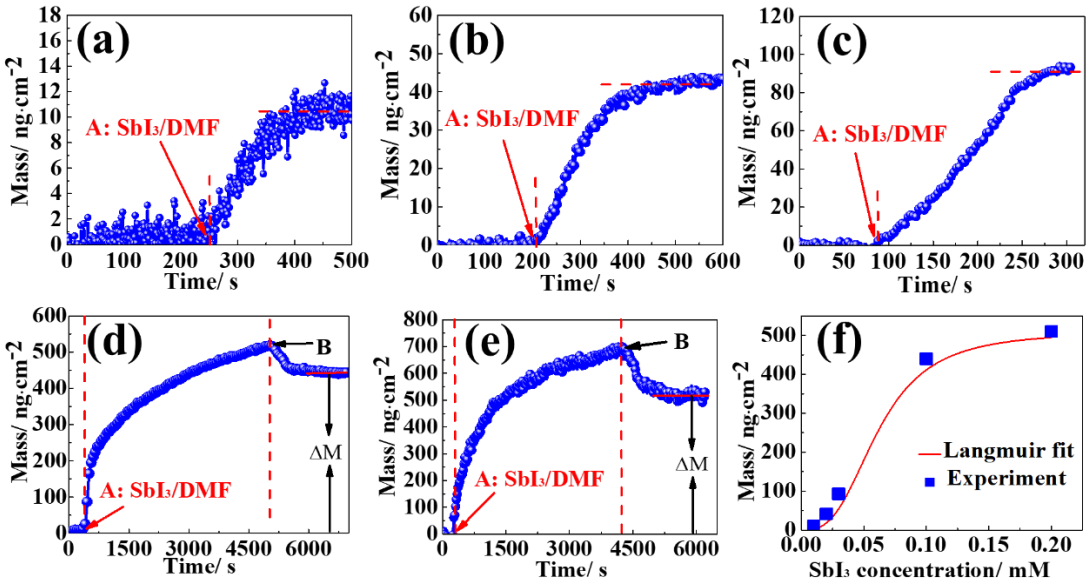

Figure 3-4 Relationship between SbI_3 adsorption density on TiO_2 and the adsorption time. Mass was calculated via the Sauerbrey equation from frequency data. The concentration of SbI_3/DMF is (a) 0.01 mM, (b) 0.02 mM, (c) 0.03 mM, (d) 0.1 mM and (e) 0.2 mM. (f) Absorption mass at different concentrations. The solid red line indicates a nonlinear least-square fit to the Langmuir model.

To investigate the kinetics of SbI_3 adsorption to TiO_2, we utilized a quartz crystal microbalance (QCM) measurement system, which monitors the SbI_3 adsorption on the TiO_2 surface. When the SbI_3/DMF solution flows over the surface of TiO_2-QCM-sensor, the SbI_3 molecule binds to -OH on the surface of TiO_2, resulting in a decrease in the vibration frequency of the TiO_2-QCM-sensor. As shown in Figure 3-3, SbI_3 is firstly adsorbed on the surface of TiO_2. After that, the surface is washed with solvent to remove the additional SbI_3. Figure 3-4 (a-e) shows the adsorbed mass on a TiO_2 surface in SbI_3/DMF solution with a concentration from 0.01 to 0.2 mM. The SbI_3 solution was introduced to the TiO_2 sensor surface at point A in the figure. With the increase in adsorption time, the mass is getting higher, but the rate of mass increase is

becoming slower. The substrates were then rinsed with pure DMF solution at point B in Figure 3-4 (d,e) to remove weakly bound SbI_3 molecules from the TiO_2 surface. Due to the presence of -OH groups on the TiO_2 surface,[30-31] SbI_3 can react with -OH to form Ti-O-Sb bonds.

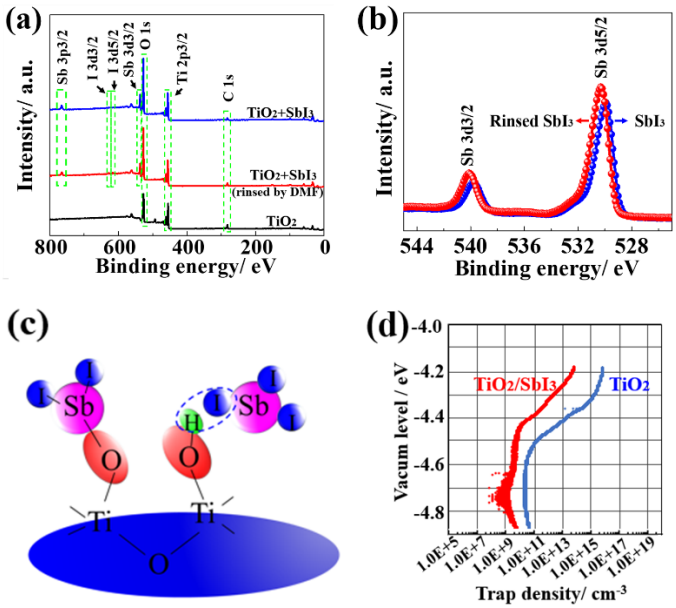

Figure 3-5 (a) XPS wide scan of TiO_2 film and SbI_3-adsorbed TiO_2 film, (b) High-resolution XPS spectra of Sb adsorbed on TiO_2 surface (spectra of Sb 3d5/2 and Sb 3d3/2). (c) Schematic diagram portraying the reaction of SbI_3 with the -OH of TiO_2. (d) Trap distribution of porous TiO_2 and TiO_2/SbI_3.

Figure 3-5 (a) shows the XPS full spectrum of bare TiO_2 (black curve) and SbI_3-adsorbed TiO_2 (blue and red curves). In the sample after rinsing with DMF, peaks corresponding to Sb elements still exist, indicating that Sb element was successfully incorporated in the TiO_2 surface. Peaks at 539.4 and 766.4 eV are assigned to Sb 3d3/2 and Sb 3p3/2, respectively. The peaks at 616.17 and 628.19 eV can be assigned to I 3d5/2 and I 3d3/2, respectively. The XPS

spectra of Sb 3d of TiO_2/SbI_3 samples is shown in Figure 3-5 (b). Before rinsing with DMF, the peak of Sb 3d5/2 and Sb 3d3/2 were observed at 529.18 and 539.77 eV. After rinsing, the Sb 3d peak pairs shift to higher binding energy location. This suggests that Ti-O-Sb linkages are formed at the TiO_2 surface. The schematic diagram showing the reaction of SbI_3 with TiO_2 is shown in Figure 3-5c. It is understood from the XPS result that the hydroxyl (-OH) on TiO_2 surface react with Sb-I to form Ti-O-Sb. The reaction mechanism is shown in Formula (i). A similar observation with PbI_2 has been reported previously by Nakayashiki et al.[30, 32]

$$Ti\text{-}OH + SbI_3 \rightarrow Ti\text{-}O\text{-}Sb + HI \quad (i)$$

The positively charged Sb is nucleophilically attacked by negatively charged O of Ti-O to form Ti-O-Sb bond and generate HI molecular. In order to further explore the influence of the passivation layer of SbI_3 on the surface of TiO_2, the surface electron trap distribution of the films was measured by using thermally stimulated current method (TSC). As shown in Figure 3-5(d), the trap density of the bare TiO_2 at a vacuum level of -4.2 eV is 10^{16}/cm^3, while that of the TiO_2/SbI_3 film was significantly reduced at -4.2 eV (10^{14}/cm^3). It has been reported that surface trap acts as recombination center. The low trap density upon passivation with SbI_3 is expected to reduce electron-hole recombination and hence helped to improve the performance of the solar cells.[33]

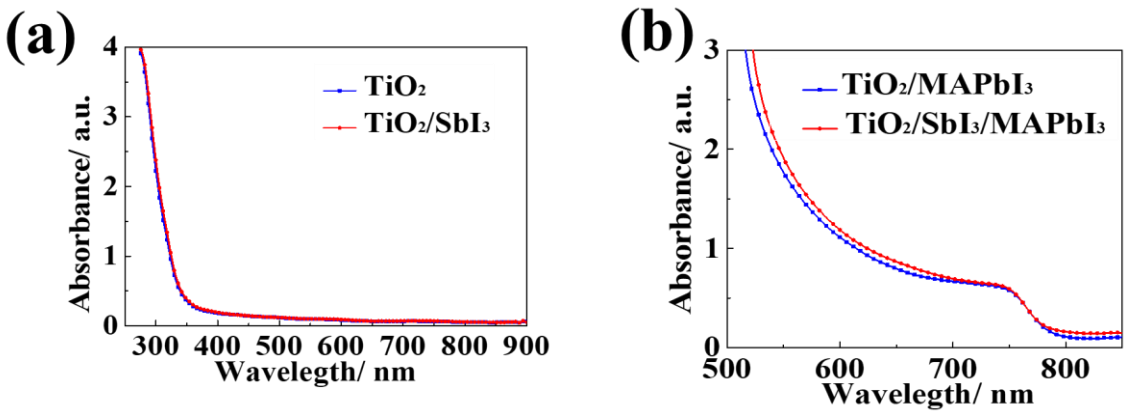

Figure 3-6 UV-visible absorption spectra of (a) TiO_2, TiO_2/SbI_3 film, and (b) perovskite film on TiO_2 and TiO_2/SbI_3 substrates.

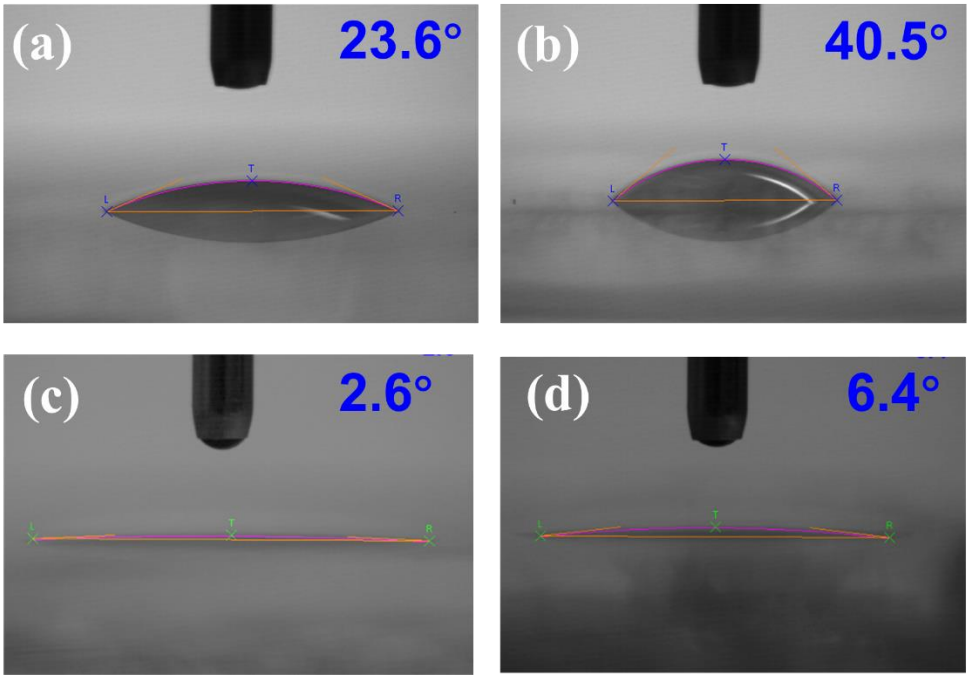

Figure 3-7 Contact angle measurement for water on (a) TiO_2 and (b) TiO_2/SbI_3 films. After plasma treatment the contact angle for water on (c) TiO_2 and (d) TiO_2/SbI_3.

In order to confirm the change of the surface properties of the films before and after passivation, we measured the contact angle of water on the films (see Figure 3-7). After

passivation, the contact angle increased significantly (from 23.6° to 40.5°), indicating that the -OH on the surface of TiO_2 decreased. This supports the results of QCM, XPS, and TSC data shown in Figure 3-4 and Figure 3-5. On device fabrication, the TiO_2 surface is treated with plasma. Hydrophilicity of the thin film after plasma treatment is enhanced, but the contact angle of TiO_2/SbI_3 (6.4°) is still larger than bare TiO_2 (2.6°) (see Figure 3-7c-d). The UV-vis absorption measurement of $MAPbI_3$ perovskite film prepared on TiO_2 and TiO_2/SbI_3 substrates were carried out to investigate the effect of the SbI_3 passivation layer on the light absorption of the perovskite films, as shown in Figure 3-6a and 3-6b. The introduction of SbI_3 has little effect on the absorption of the TiO_2 film (See Figure 3-6a). However, the absorption from 500 nm to 800 nm of the perovskite film was enhanced on the TiO_2/SbI_3 substrates. Figure 3-8 (a) shows top-view SEM images of the $MAPbI_3$ film deposited on mp-TiO_2. It can be seen that there are some pin-holes on the perovskite film and is clearly visible at high magnification in Figure 3-8 (b). While, in Figure 3-8 (d) the perovskite films deposited on the TiO_2 passivated by SbI_3 were significantly improved, and the perovskite crystals were arranged more densely without pin-holes, at high magnification (Figure 3-8e). The $TiO_2/SbI_3/MAPbI_3$ film in Figure 3-8f was smoother and denser, compared with $TiO_2/MAPbI_3$ film (Figure 3-8c). Corresponding 3D AFM images are shown in Figure 3-9. In addition, the X-ray diffraction (XRD) spectra in Figure 3-10 show that there is no significant crystallographic difference of the perovskite layer between passivation and non-passivation cases; however, the full width at half maximum (FWHM) of perovskite is smaller for $TiO_2/SbI_3/MAPbI_3$ indicating SbI_3 passivation can increase the crystallinity of $MAPbI_3$.

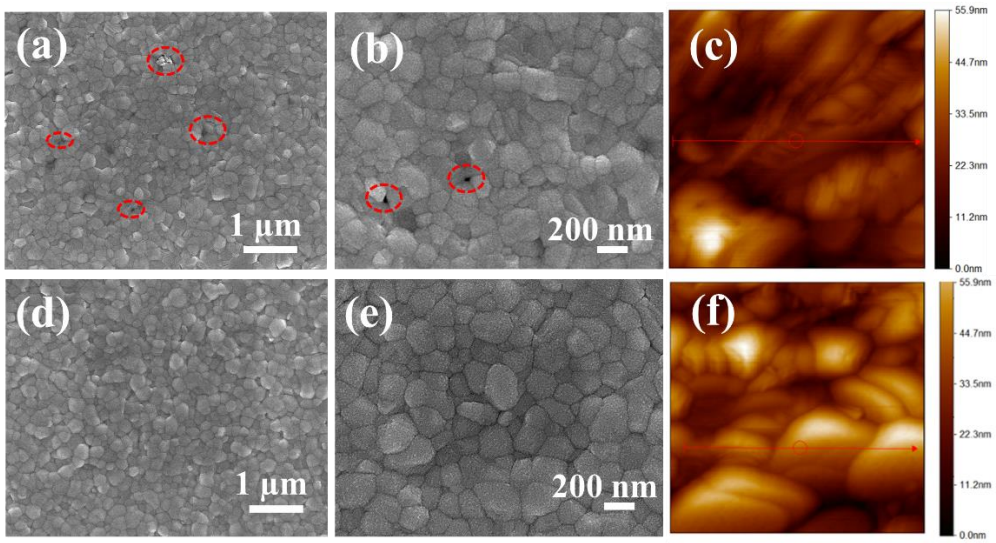

Figure 3-8. Top-view of SEM (a, b, d, e) and 2D AFM (c, f) images of $MAPbI_3$ perovskite film deposited on (a, b, c) FTO/TiO_2 and (d, e, f) FTO/TiO_2/SbI_3.

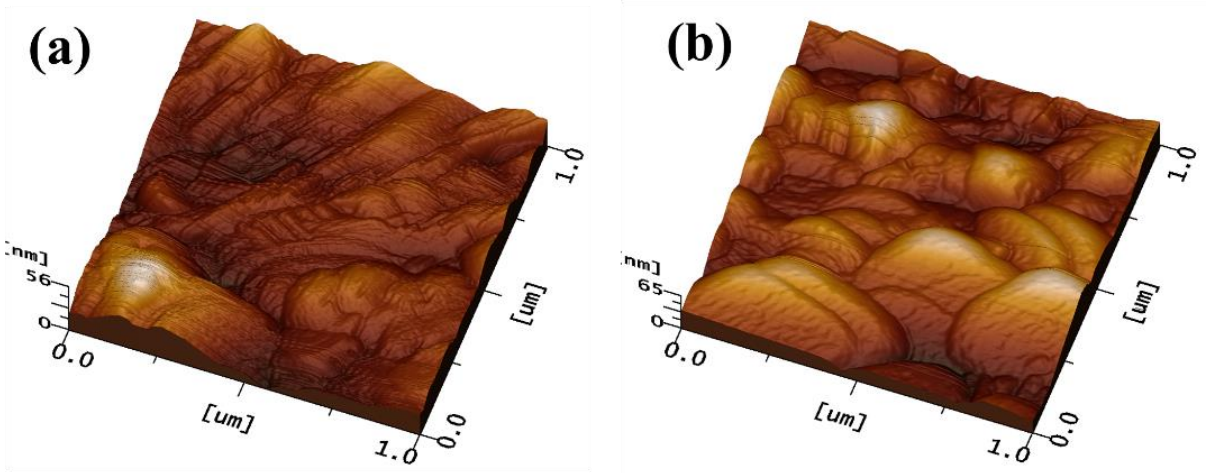

Figure 3-9. 3D AFM images of $CH_3NH_3PbI_3$ perovskite film deposited on (a) TiO_2 and (b) TiO_2/SbI_3 substrate.

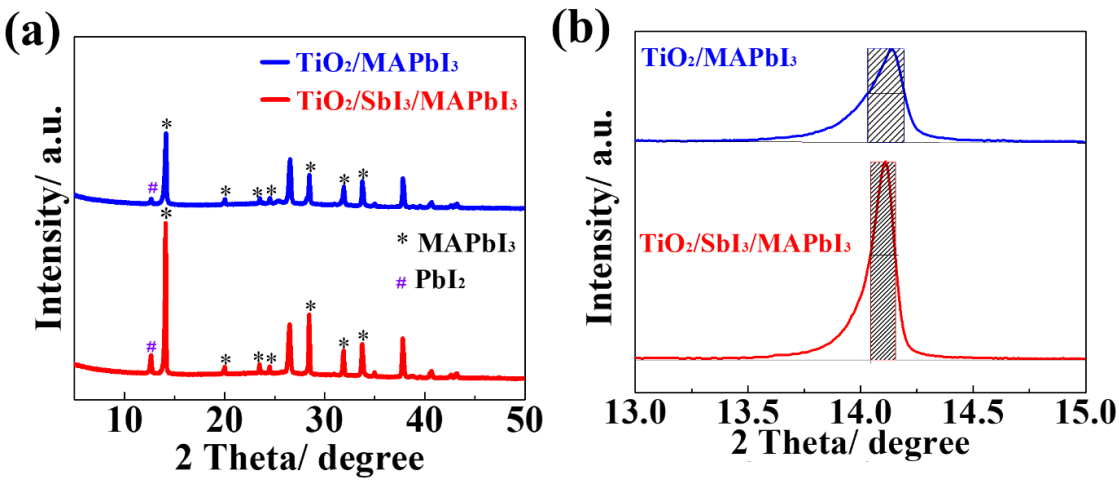

Figure 3-10 (a) X-ray diffraction spectra of $CH_3NH_3PbI_3$ perovskite films deposited on TiO_2 (blue) and TiO_2/SbI_3 (red) substrate. (b) The full width at half maximum (FWHM) of the peak at 14.17°。

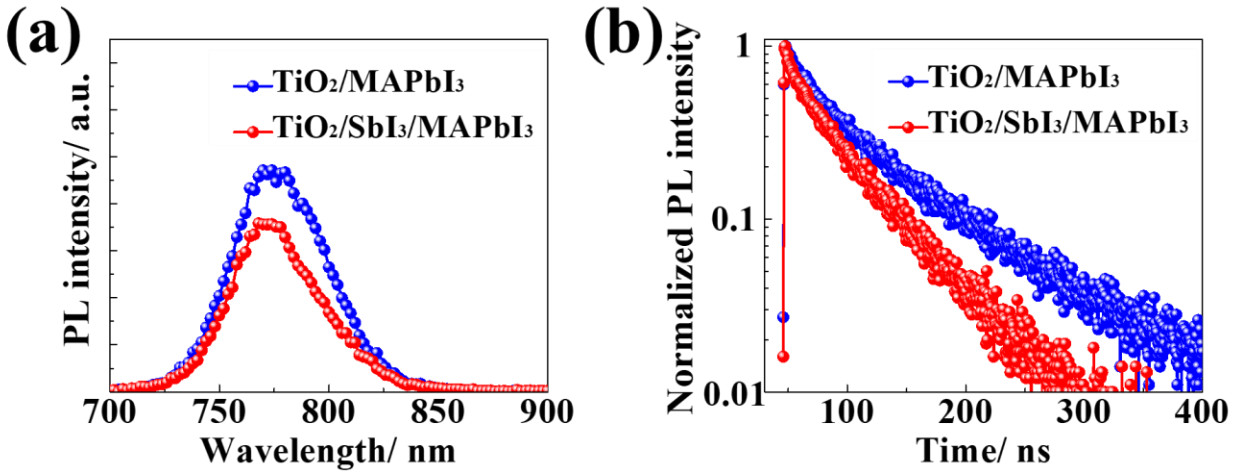

Figure 3-11. (a) Steady-state PL spectra and (b) TRPL spectroscopy for perovskite films deposited on TiO_2 and TiO_2/SbI_3 substrates.

In order to better ascertain the effect of the SbI_3 passivation layer on electron transport, the charge dynamics of the perovskite film deposited on TiO_2 and TiO_2/SbI_3 were carefully

examined by using PL spectroscopy. The steady-state PL and TRPL spectra as shown in Figure 3-11. The PL quenching effect is an evidence of carrier charge separation at the interface. Figure 3-11a portrays the PL quenching on perovskite film deposited on TiO_2/SbI_3 compared to that on bare TiO_2, showing a faster electron transport after SbI_3 passivation. More interestingly, the perovskite film deposited on TiO_2/SbI_3 showed a slight blue-shifted PL peak from 774 nm to 772 nm compared with the non-passivation sample, which implies the SbI_3 passivation layer can effectively inhibit charge recombination.[34] The TRPL spectroscopy in Figure 3-11b shows a significant reduction in decay time after passivation, again consistent with effective electron transfer to the SbI_3 modified TiO_2.

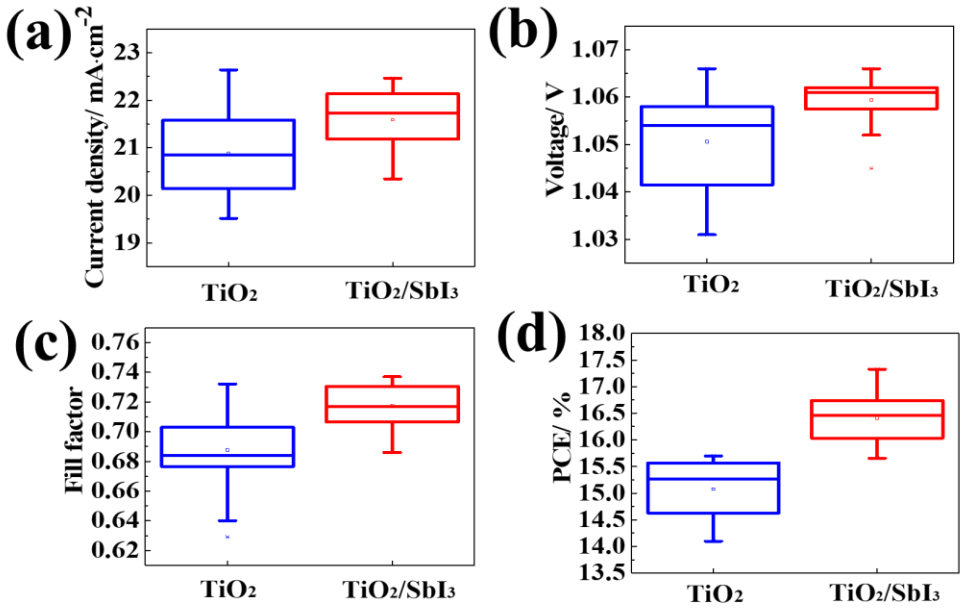

Figure 3-12 Box charts of 20 independent solar cells in each group (a) J_{SC}, (b) V_{OC}, (c) FF and (d) PCE for perovskite solar cells based on TiO_2 and TiO_2/SbI_3.

Figure 3-12 (a-d) are the box charts of detailed photovoltaic performance. After the passivation of the TiO_2 electron transport layer with SbI_3, the solar cell performance was

significantly improved. As mentioned above, after passivation, the concentration of trap on the TiO_2 surface decreased. This decreases the chance of electrons and holes recombining on the TiO_2 surface, resulting in a higher open circuit voltage and fill factor.

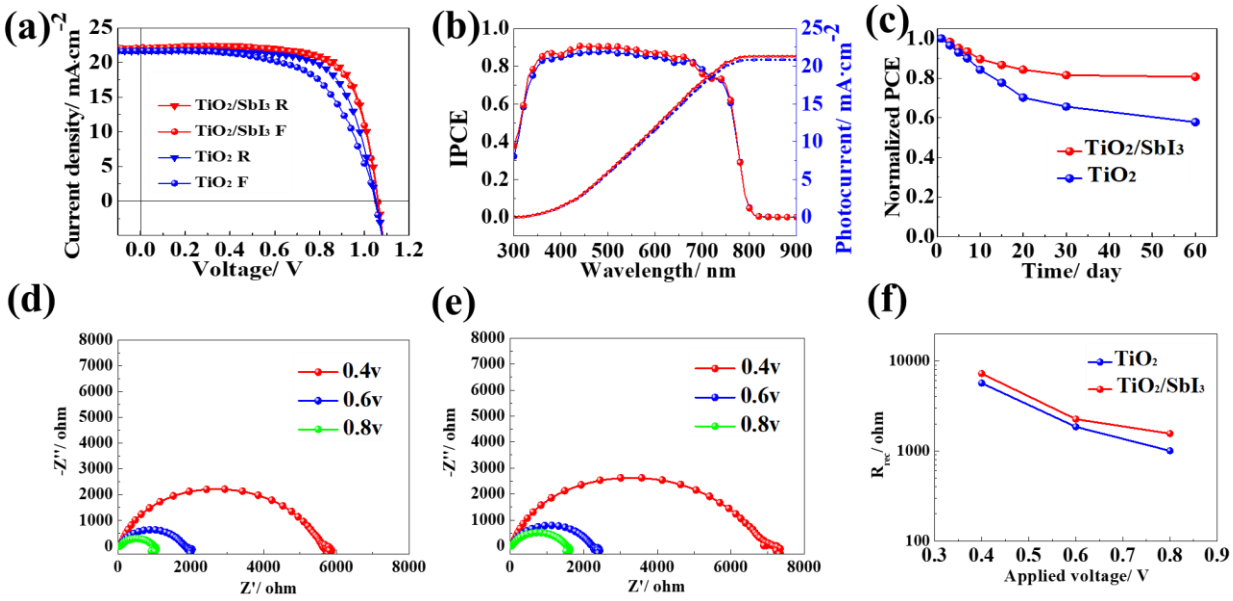

Figure 3-13 (a) J-V curves and (b) IPCE spectra of the champion devices based on TiO_2 and TiO_2/SbI_3. (c) Stability test for TiO_2 and TiO_2/SbI_3 based perovskite solar cells. The devices were stored in a ~50% humidity air environment. Nyquist plots of devices based on (d) TiO_2 and (e) TiO_2/SbI_3 measured in dark condition with different forward applied bias (0.4, 0.6 and 0.8v). (f) Carrier recombination resistance extracted from EIS measurements at varied bias potentials.

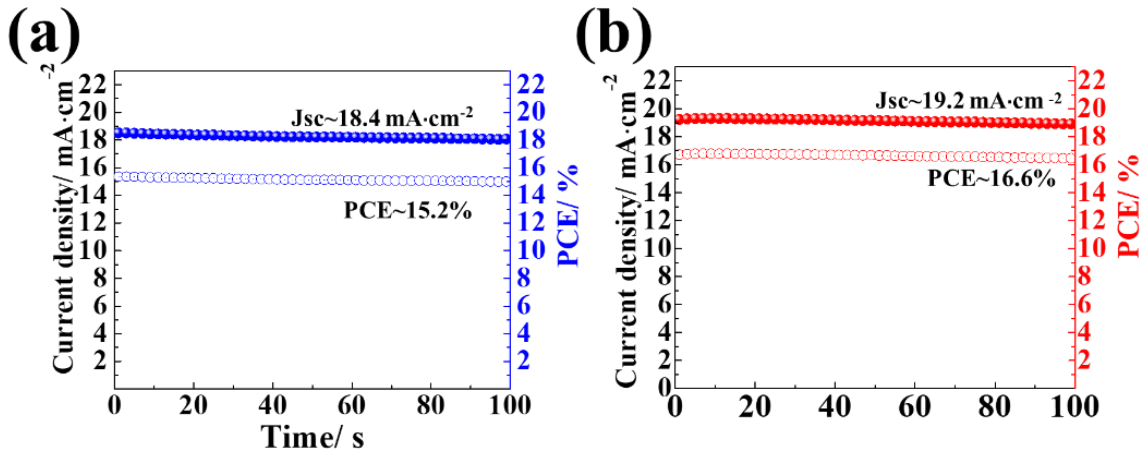

Figure 3-14 Maximal steady-state photocurrent output of the solar cells, (a) at 0.83 V for the TiO_2-based device and (b) at 0.87 V for the TiO_2/SbI_3-based device, under constant 1 SUN illumination.

J-V and IPCE characteristics of the solar cells with the highest PCE based on TiO_2 and TiO_2/SbI_3 are shown in Figure 3-13 (a, b). TiO_2 based solar cell showed a large hysteresis, while the solar cell based on TiO_2/SbI_3 showed almost no hysteresis. As previously reported, such photocurrent hysteresis is also typically observed in many kinds of electronic devices, particularly defect-rich, organic-based electronic devices, which contain a non-negligible amount of charge traps.[34-36] In this work, after passivated with SbI_3, trap on TiO_2 surface obviously decrease, therefore, the hysteresis is effectively reduced. A high PCE of 17.33%, with J_{SC}, V_{OC}, and FF, of 1.06 V, 22.16 $mA \cdot cm^{-2}$, and 0.74 respectively, were obtained under standard illumination conditions (AM 1.5G, 100 $mW \cdot cm^{-2}$). Clearly, the application of a SbI_3 passivation layer increased the PCE from 15.82% (J_{SC}=21.65 $mA \cdot cm^{-2}$, V_{OC}= 1.05 V and FF= 0.70) to 17.33%, which comes mainly from the enhanced J_{SC} and FF. To investigate the effect of SbI_3 passivation on the device stability, we have also measured the maximal steady-state photocurrent

output of the two representative devices by applying a constant bias voltage (0.83 V for the TiO_2-based device, 0.87 V for the TiO_2/SbI_3-based device) taken from the maximum power points (MPP) in the J-V measurements. Figure 3-14 (a, b) show that the steady-state efficiency of the cells based on TiO_2 and TiO_2/SbI_3 are stabilized at 16.6% and 15.2%, respectively. In all, SbI_3 plays a very positive passivation effect on the electronic transport layer, resulting in an enhanced efficiency. The long-term stability of PSCs is closely related to the front ESL/perovskite interfacial charge accumulation during operation.[7,37-38] We examined the long-term stability of PSCs based on TiO_2/SbI_3 and TiO_2. The unencapsulated solar cells for long-term stability test were done in air condition with about 50% humidity at room temperature for two months. Figure 3-13 (c) presents the PCE change of both devices as a function of aging time. The devices based on TiO_2/SbI_3 showed enhanced stability, maintained 81% of the initial PCE after storage in air condition for 60 days, whereas those based on TiO_2 retained 58% of their initial efficiency.

To further investigate the interfacial charge transport process in the device, EIS measurement was performed for TiO_2 and TiO_2/SbI_3 based perovskite solar under a dark condition at different applied bias. The Nyquist plot in Figure 3-13 (d) and (e) shows the typical semicircles. Based on the previous report, the semicircle could be related to the overall charge transport in the devices.[31,39] From Figure 3-13 (f), at the same bias compare to the TiO_2-based device, the TiO_2/SbI_3-based device shows a higher charge recombination resistance. Theoretically, a large recombination resistance favors delayed carrier recombination and helps to increase the FF, which is consistent with the box chart in Figure 3-12 (c).[40-41]

3.4 Conclusions

In summary, we demonstrated that the interface between the electron transporting layer and perovskite is important for device performance of perovskite solar cells. The thin SbI_3 passivation layer was prepared by a simple immersion method which can passivate the TiO_2 surface and thus effectively reduced the TiO_2 electronic trap states and enabled faster electron transport. QCM monitors of the adsorption of SbI_2 on TiO_2 surface, XPS and TSC result effectively proved that the surface trap concentration of TiO_2 after passivation was reduced. The solar cell efficiency with the SbI_3-passivated mesoporous TiO_2 electrodes was enhanced from 15.82% (15.04% in average) to over 17.33% (16.41% on average). Even after 60 days, the device still maintained more than 80% of the initial efficiency at air without encapsulation.

3.5 References

[1] J.-P. Correa-Baena; Tress, W.; Domanski, K.; Anaraki, E.H.; Turren-Cruz, S.-H.; Roose, B.; Boix, P.P.; Grätzel, M.; Saliba, M.; Abate, A., Energy & Environmental Science 10 (2017) 1207-1212.

[2] H.-H. Fang; Adjokatse, S.; Shao, S.; Even, J.; Loi, M.A., Nature communications 9 (2018) 243.

[3] N.F. Montcada; Méndez, M.; Cho, K.T.; Nazeeruddin, M.K.; Palomares, E., Nanoscale 10 (2018) 6155-6158.

[4] K. Domanski; Alharbi, E.A.; Hagfeldt, A.; Grätzel, M.; Tress, W., Nature Energy 3 (2018) 61.

[5] A. Kojima; Teshima, K.; Shirai, Y.; Miyasaka, T., J. Am. Chem. Soc. 131 (2009) 6050-6051.

[6] W.S. Yang; Park, B.-W.; Jung, E.H.; Jeon, N.J.; Kim, Y.C.; Lee, D.U.; Shin, S.S.; Seo, J.; Kim, E.K.; Noh, J.H., Science 356 (2017) 1376-1379.

[7] H. Tan; Jain, A.; Voznyy, O.; Lan, X.; De Arquer, F.P.G.; Fan, J.Z.; Quintero-Bermudez, R.; Yuan, M.; Zhang, B.; Zhao, Y., Science 355 (2017) 722-726.

[8] S.S. Shin; Yeom, E.J.; Yang, W.S.; Hur, S.; Kim, M.G.; Im, J.; Seo, J.; Noh, J.H.; Seok, S.I., Science 356 (2017) 167-171.

[9] J.-P. Correa-Baena; Nienhaus, L.; Kurchin, R.C.; Shin, S.S.; Wieghold, S.; Putri Hartono, N.T.; Layurova, M.; Klein, N.D.; Poindexter, J.R.; Polizzotti, A., Chem. Mater. 30 (2018) 3734-3742.

[10] F. Yang; Kapil, G.; Zhang, P.; Hu, Z.; Kamarudin, M.A.; Ma, T.; Hayase, S., ACS applied materials & interfaces 10 (2018) 16482-16489.

[11] N. Fu; Huang, C.; Liu, Y.; Li, X.; Lu, W.; Zhou, L.; Peng, F.; Liu, Y.; Huang, H., ACS applied materials & interfaces 7 (2015) 19431-19438.

[12] S. Sidhik; Cerdan Pasaran, A.; Esparza, D.; Lopez Luke, T.; Carriles, R.n.; De La Rosa, E., ACS applied materials & interfaces 10 (2018) 3571-3580.

[13] F. Giordano; Abate, A.; Baena, J.P.C.; Saliba, M.; Matsui, T.; Im, S.H.; Zakeeruddin, S.M.; Nazeeruddin, M.K.; Hagfeldt, A.; Graetzel, M., Nature communications 7 (2016) 10379.

[14] T. Matsui; Seo, J.Y.; Saliba, M.; Zakeeruddin, S.M.; Grätzel, M., Adv. Mater. 29 (2017) 1606258.

[15] D. Liu; Li, S.; Zhang, P.; Wang, Y.; Zhang, R.; Sarvari, H.; Wang, F.; Wu, J.; Wang, Z.; Chen, Z.D., Nano Energy 31 (2017) 462-468.

[16] H. Zhang; Shi, J.; Xu, X.; Zhu, L.; Luo, Y.; Li, D.; Meng, Q., Journal of Materials Chemistry A 4 (2016) 15383-15389.

[17] T. Singh; z, S.; Sasinska, A.; Frohnhoven, R.; Mathur, S.; Miyasaka, T., Adv. Funct. Mater. 28 (2018) 1706287.

[18] Z. Xu; Yin, X.; Guo, Y.; Pu, Y.; He, M., Journal of Materials Chemistry C 6 (2018) 4746-4752.

[19] D.H. Kim; Han, G.S.; Seong, W.M.; Lee, J.W.; Kim, B.J.; Park, N.G.; Hong, K.S.; Lee, S.; Jung, H.S., ChemSusChem 8 (2015) 2392-2398.

[20] H. Zhou; Chen, Q.; Li, G.; Luo, S.; Song, T.-b.; Duan, H.-S.; Hong, Z.; You, J.; Liu, Y.; Yang, Y., Science 345 (2014) 542-546.

[21] Q. Cai; Zhang, Y.; Liang, C.; Li, P.; Gu, H.; Liu, X.; Wang, J.; Shentu, Z.; Fan, J.; Shao, G., Electrochim. Acta 261 (2018) 227-235.

[22] J. Peng; Wu, Y.; Ye, W.; Jacobs, D.A.; Shen, H.; Fu, X.; Wan, Y.; Wu, N.; Barugkin, C.; Nguyen, H.T., Energy & Environmental Science 10 (2017) 1792-1800.

[23] D. PéRez-Del-Rey; Boix, P.P.; Sessolo, M.; Hadipour, A.; Bolink, H.J., The journal of physical chemistry letters 9 (2018) 1041-1046.

[24] M.M. Tavakoli; Giordano, F.; Zakeeruddin, S.M.; GräTzel, M., Nano Lett. 18 (2018) 2428-2434.

[25] J.Y. Seo; Uchida, R.; Kim, H.S.; Saygili, Y.; Luo, J.; Moore, C.; Kerrod, J.; Wagstaff, A.; Eklund, M.; Mcintyre, R., Adv. Funct. Mater. 28 (2018) 1705763.

[26] S. You; Wang, H.; Bi, S.; Zhou, J.; Qin, L.; Qiu, X.; Zhao, Z.; Xu, Y.; Zhang, Y.; Shi, X., Adv. Mater. 30 (2018) 1706924.

[27] J.-H. Im; Jang, I.-H.; Pellet, N.; Grätzel, M.; Park, N.-G., Nature nanotechnology 9 (2014) 927.

[28] G.-H. He; Liang, C.-J.; Ou, Y.-D.; Liu, D.-N.; Fang, Y.-P.; Xu, Y.-H., Mater. Res. Bull. 48 (2013) 2244-2249.

[29] P. Liu; Lu, F.; Wu, M.; Luo, X.; Cheng, Y.; Wang, X.-W.; Wang, W.; Wang, W.-H.; Liu, H.; Cho, K., Journal of Materials Chemistry C 5 (2017) 9066-9071.

[30] S. Nakayashiki; Daisuke, H.; Ogomi, Y.; Hayase, S., Journal of Photonics for Energy 5 (2015) 057410.

[31] X. Zhu; Yang, D.; Yang, R.; Yang, B.; Yang, Z.; Ren, X.; Zhang, J.; Niu, J.; Feng, J.; Liu, S.F., Nanoscale 9 (2017) 12316-12323.

[32] F. Zhang; Song, J.; Hu, R.; Xiang, Y.; He, J.; Hao, Y.; Lian, J.; Zhang, B.; Zeng, P.; Qu, J., Small 14 (2018) 1704007.

[33] Y. Ogomi; Morita, A.; Tsukamoto, S.; Saitho, T.; Shen, Q.; Toyoda, T.; Yoshino, K.; Pandey, S.S.; Ma, T.; Hayase, S., The Journal of Physical Chemistry C 118 (2014) 16651-16659.

[34] Y. Shao; Xiao, Z.; Bi, C.; Yuan, Y.; Huang, J., Nature communications 5 (2014) 5784.

[35] A. Campos; Riera-Galindo, S.; Puigdollers, J.; Mas-Torrent, M., ACS applied materials & interfaces 10 (2018) 15952-15961.

[36] X. Xiao; Bao, C.; Fang, Y.; Dai, J.; Ecker, B.R.; Wang, C.; Lin, Y.; Tang, S.; Liu, Y.; Deng, Y., Adv. Mater. 30 (2018) 1705176.

[37] Y.I. Lee; Jeon, N.J.; Kim, B.J.; Shim, H.; Yang, T.Y.; Seok, S.I.; Seo, J.; Im, S.G., Advanced Energy Materials 8 (2018) 1701928.

[38] E. Halvani Anaraki; Kermanpur, A.; Mayer, M.T.; Steier, L.; Ahmed, T.; Turren-Cruz, S.-H.; Seo, J.; Luo, J.; Zakeeruddin, S.M.; Tress, W.R., ACS Energy Letters 3 (2018) 773-778.

[39] H. Wei; Xiao, J.; Yang, Y.; Lv, S.; Shi, J.; Xu, X.; Dong, J.; Luo, Y.; Li, D.; Meng, Q., Carbon 93 (2015) 861-868.

[40] W. Li; Dong, H.; Guo, X.; Li, N.; Li, J.; Niu, G.; Wang, L., Journal of Materials Chemistry A 2 (2014) 20105-20111.

[41] M. Stolterfoht; Wolff, C.M.; Amir, Y.; Paulke, A.; Perdigón-Toro, L.; Caprioglio, P.; Neher, D., Energy & Environmental Science 10 (2017) 1530-1539.

Chapter 4. Nb_2O_5 surface passivation for enhanced performance of ZnO based perovskite solar cells

4.1 Introduction

In the recent past, perovskite solar cells (PSCs) have gained widespread attention around the world due to the rapid improvement in the device performance,[1-6] with record 22.7% of certified power conversion efficiency (PCE) from 3.8% in a very short time span.[7-9] Initially, PSC device structure was inspired by conventional dye-sensitized solar cells, where a liquid electrolyte was implemented as a hole-transport material.[10-11] Utilization of the liquid electrolyte was found to have the serious corrosive effect on the perovskite absorbing layer leading to the fast degradation the solar cell in few minutes. To circumvent this issue, use of the Spiro-OMeTAD as a solid-state hole-transporting material in PSCs not only led to the greatly improved PCE but also the stability. This result ignited fast pace development in the area of PSCs research with two mainly adopted mesoporous and planar device architectures.[12-17] Mesoporous structure was designed by the introduction of semiconductor or insulating nanoparticles as a scaffold for perovskite absorber, which in addition affects the charge carrier transport also depending on physical properties of semiconductor under consideration. Amongst various mesoporous material attempted so far, TiO_2 was one of the most preferred wide band gap semiconductor but requires very high sintering temperature of ~500 °C, rendering it unsuitable for the use of indium tin oxide or flexible substrates. Although efforts have

also been directed towards the preparation of TiO_2 mesoporous layer under milder conditions, however, led to seriously hampered PCE. Very high charge carrier mobility and life-time of the perovskite absorber,[18-21] led to the proposal of planar device architecture owing to the efficient and relatively fast fabrication as compared to that of mesoporous device structure. The planar structure can be n-i-p or p-i-n type, where both n and p type semiconductors at the bottom are only of few hundred nanometers on the substrate surface. Due to the absence of mesoporous materials, the high-temperature sintering step can also be avoided, which simplifies the fabrication steps of PSCs and enhances their potential applications on flexible substrates.

In low temperature processed planar structure based PSCs, ZnO is one of the potential candidates as electron transporting material due to higher electron mobility and a simpler preparation process.[12,21-22] However, studies have indicated about the proton transfer at the perovskite/ZnO interface leading to perovskite decomposition.[23-24] In addition, hydroxyl groups at the surface or remaining acetate groups from the precursor can also lead to perovskite decomposition. In order to overcome this shortcoming, some research groups have done ZnO surface modification by 3-aminopropanoic acid or use of self-assembled monolayer to modify the surface of ZnO.[25-30] ZnO layers fabricated by Al doped ZnO[31] and surface modification with a self-assembled monolayer simultaneously[23] has also been reported. Therefore, present work focuses on the fabrication of a thin layer of Nb_2O_5 for ZnO surface passivation, which has been reported as an effective blocking layer in case of dye sensitized solar cells and PSCs.[32-33] Amorphous Nb_2O_5 can be fabricated at low temperatures and works as an efficient blocking layer. Apart from this, its composite with TiO_2 was considered as a potential photoelectrode in dye sensitized solar cells too.[34] In spite of these promising role of

Nb_2O_5, there have been very less work pertaining to photoelectrode fabrication, especially its passivation effect on the top of ZnO semiconductor layer has not yet been explored. In addition, the conduction band of Nb_2O_5 is almost at the same level as that of ZnO, which enables to cause swift electron injection from perovskite layer to ZnO, which encouraged us to investigate about the fabrication of planar PSCs consisting of ultrathin Nb_2O_5/ZnO double layer.

In this work, it has shown that an ultrathin Nb_2O_5 passivating layer can be formed utilizing the sol-gel method on the top of the ZnO layer, which could not only reduce ZnO surface defects but also improves morphology of the $CH_3NH_3PbI_3$ perovskite film. It has been clearly demonstrated that with Nb_2O_5 passivating layer on ZnO, there is drastic improvement in the stability of perovskite absorber for > 20 days in air, which was less than 10 min when it was prepared over non-passivated bare ZnO. At the same time, there was a drastic improvement in the PCE from about 1% (bare ZnO) to 14.57% (13.56% average) after insertion of Nb_2O_5 passivating layer. In addition, this simple and effective method provides the direction for fabricating the stable and efficient PSCs cell under ambient conditions, which can pave the path for other PSCs as well for their commercialization.

4.2. Experimental

4.2.1 Materials and Method

0.4 M of ZnO precursor solution was prepared according to previous reported procedure.[83] In brief, it was prepared by dissolving Zinc acetate dihydrate (Wako, Japan 953 mg) and 850 µL of ethanolamine (Sigma, 99.5%) in the 10 ml of 2-methoxyethanol (Sigma, 99.8%) under stirring. Nb_2O_5 precursor solution (0.04 M) was prepared by

dissolving 128 mg of niobium chloride (Wako, Japan, 99.9%) in the 10 ml of dehydrated ethanol (Wako, Japan, 99.5%).

One-step solution processing method has been used for the fabrication of perovskite absorber layer. 1.5 M solution of perovskite precursor was prepared as reported earlier.[84] Methylammonium iodide (MAI) (Wako, Japan, 477 mg) and lead iodide (PbI_2) (Tokyo Chemical Industry, Japan, 1.38 gm) were dissolved in a mixture of dimethylformamide (Wako, Japan, 1.6 mL) and dimethyl sulfoxide (Wako, Japan, 0.4 mL) and stirred for 20 min at room temperature. This perovskite precursor solution was subjected to filtration using a 0.45 μm PVDF syringe filter to remove any insoluble sediments. Spiro-OMeTAD solution as hole transporting material was prepared by dissolving 72.3 mg of Spiro-OMeTAD (Merck) was dissolved in 1 mL chlorobenzene along with 17.5 μL of lithium bis(trifluoromethanesulfonyl)imide (Sigma, 99.9%) solution (520 mg mL^{-1} in acetonitrile) and 28.8 μL of 4-tert-butylpyridine.

4.2.2 Thin film characterization

Surface morphology of the prepared perovskite layer was investigated using a scanning electron microscope (JCM-6000 Nano Scope). A Veeco Dektak 150 surface profilometer was used to estimate the thickness of the ZnO film. UV-Visible electronic absorption spectra of the samples were obtained using a Shimadzu UV-2550 spectrophotometer. The X-ray diffraction (XRD) patterns of the perovskite films were recorded on Rigaku Smart Lab X-ray diffractometer with Cu Kα radiation (λ=1.5418 Å), 45 kV and 200 mA at room temperature.

4.2.3 Device Fabrication

Pre-patterned fluorine doped tin oxide (FTO) glass substrates (Nippon Sheet Glass Co. Ltd.) were cleaned sequentially with detergent, acetone, isopropanol and deionized water for 15 min. each, respectively, followed by 10 min oxygen plasma treatment. To prepare ZnO electron transport layer, the ZnO sol-gel precursor was spin coated onto FTO substrates, followed by heating at 200 °C for 30 min. Afterwards, Nb_2O_5 layer was prepared by spin coating a solution of niobium chloride (0.04 M in ethanol) on the same substrate and dried at 200 °C for 10 min. For preparation of perovskite layer, the perovskite precursor solution was spin coated on the Nb_2O_5 passivated ZnO layer at 4000 rpm for 25 s. In the meantime, 0.5 mL ethyl acetate acting as an antisolvent was quickly dropped onto the centre of the substrate at the 10th second while spinning. The obtained films were then dried at 65 °C for 1 min and 100 °C for 10 min. Subsequently, 20 μL of Spiro-OMeTAD solution was spin coated on top of the perovskite layer at 4000 rpm for 30 s. Devices were then left in a desiccator overnight and finally 80 nm of Au electrode was deposited by thermal evaporation to complete the perovskite solar cell used in this work.

4.2.4 Photovoltaic measurement

The current-voltage characteristics of PSCs thus fabricated were measured in air using a solar simulator (KHP-1, Bunko-Keiki, Japan) equipped with an AM 1.5 G filter at a calibrated intensity of 100 $mW \cdot cm^{-2}$ illumination. Illumination intensity of the solar simulator was confirmed by a standard silicon reference cell (BS-520 S/N 007, Bunko-Keiki, Japan). The incident photon to current conversion efficiency (IPCE) spectra were also measured in air under short-circuit conditions using the solar simulator. The working area of the cell was precisely maintained to be 0.10 cm^2 using a black metal mask.

4.3. Results and discussion

Device structure PSCs fabricated and used for investigation in this work has been schematically shown in the Figure 4-1(a). Solution processed electron transport layer consisted of ZnO was deposited by sol-gel method using zinc acetate precursor solution. A surface passivation layer of Nb_2O_5 was then fabricated onto the ZnO layer. Light harvesting perovskite layer consisted of $CH_3NH_3PbI_3$ with a band gap of 1.55 eV [9] was spin coated on the ZnO layer in the presence and absence of Nb_2O_5 passivation layer in order demonstrate the implications of surface passivation on the device performance. An energetic cascade between light absorber, hole transport layer and electron transport layer is one of the important requirements for optimal device functioning in the solar cells. A perusal of energy band diagram shown in the Figure 4-1(b) indicates that free electrons and holes generated in the $CH_3NH_3PbI_3$ layer after photoexcitation can easily undergo charge separation and collection owing to the favorable energy cascade of the different layers. Electrons can move to the underlying ZnO/Nb_2O_5 layer whereas the holes migrate towards the spiro-OMeTAD, as schematically shown in Figure 4-1 (b). Various characterizations pertaining to the nature of surface passivation, quality of perovskite layer and its stability on the substrate surface have been systematically carried out and depicted in the Figure 4-2.

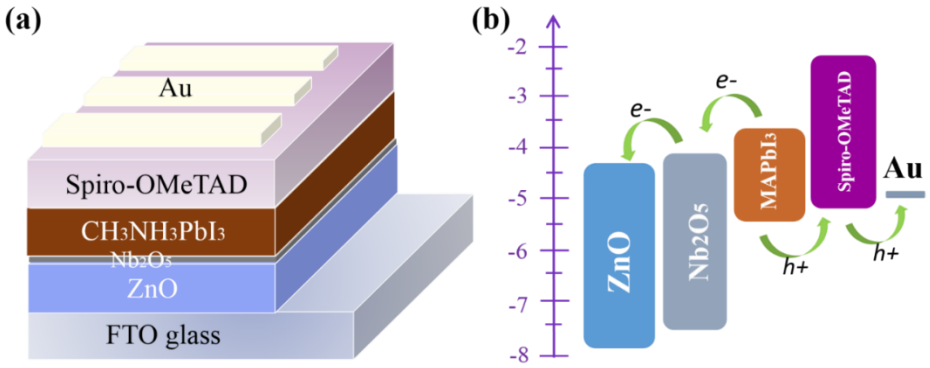

Figure 4-1 (a) Schematic diagram showing the complete device struture and (b) Energy band daigram showing the energy level with respect to vacuum level for the different components of the PSC, on the left the scale shows values in eV.

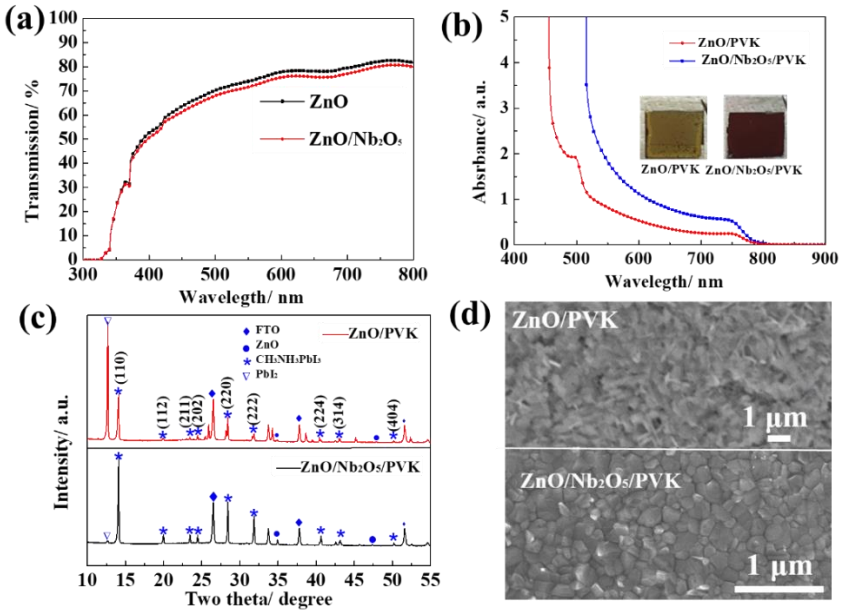

Figure 4-2 (a) Transmission spetcra of ZnO (black) and ZnO/Nb_2O_5 (red) thin films fabricated on FTO glass. (b) Absorption spectra of ZnO/PVK (red) and ZnO/Nb_2O_5/PVK (blue) while inset shows the photograph of the respective thin film taken 10 min. after their fabriaction. (c) XRD pattern of the films with (black) and without (red) Nb_2O_5 layer incorporation. (d) SEM image of PVK layers coated on ZnO (top) and ZnO/Nb_2O_5 (bottom).

Optical transmittance spectrum of FTO substrate coated with ZnO and in the presence and absence of Nb_2O_5 surface passivation layer is shown in Figure 4-2(a). It can be seen that FTO/ZnO film has slightly higher transmittance than FTO/ZnO/N_2O_5 film in the wavelength range of 400 nm to 800 nm. Since Nb_2O_5 is ultra-thin, it has very little effect on the transmittance of the film. Figure 4-3 also shows the negligible difference in the absorption spectra for ZnO single layer and Nb_2O_5/ZnO double layer as the reference, exhibiting the flat curve in 400-800 nm range. It can be seen that perovskite film onto ZnO single layer and ZnO/Nb_2O_5 double layer, optical absorption of the perovskite (PVK) layer i.e. ZnO/PVK and ZnO/Nb_2O_5/PVK was strikingly enhanced, especially in the visible wavelength region up to 800 nm as shown in the Figure 4-2(b). As previously reported, the absorption onset of the $CH_3NH_3PbI_3$ perovskite absorber is near to 800 nm with the optical band gap (Eg) of $CH_3NH_3PbI_3$ perovskite to be (Eg ~ 1.55 eV),[3,8,35] which is almost the same in both cases. However, there is significant difference in absorption coefficients and ZnO/PVK exhibits relatively lower value as compared to that of ZnO/Nb_2O_5/PVK (Figure 4-2b). At the same time, ZnO/Nb_2O_5/PVK film appears to be dark brown whereas ZnO/PVK shows not only the poor film morphology but color of the film was also yellowish in appearance (Figure 4-2b, inset). This could be attributed to decomposition of the perovskite films deposited on ZnO due to the presence of acetate ligands or hydroxyl groups on the ZnO surface. Apart from this, basic nature of the ZnO can also result in perovskite decomposition due to movement of the holes at the perovskite/ZnO interface as reported by Yang et. al.[24]

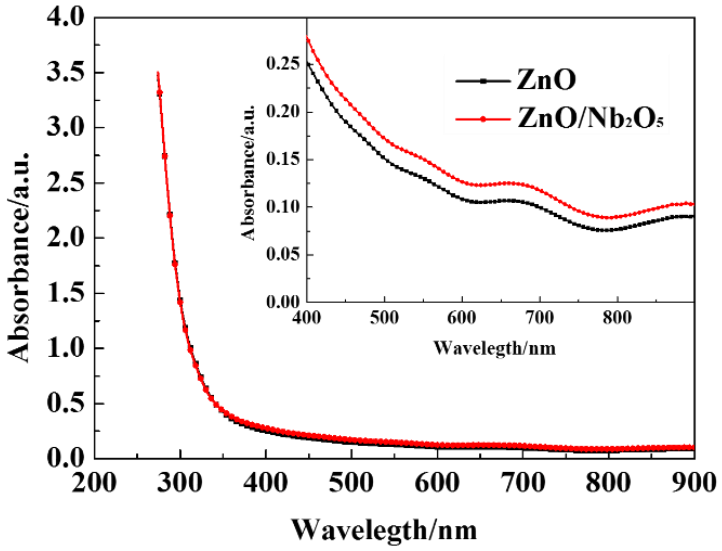

Figure 4-3 Electronic absorption spectra of ZnO and ZnO/Nb_2O_5 film prepared on FTO glass. Inset shows the enlarged view.

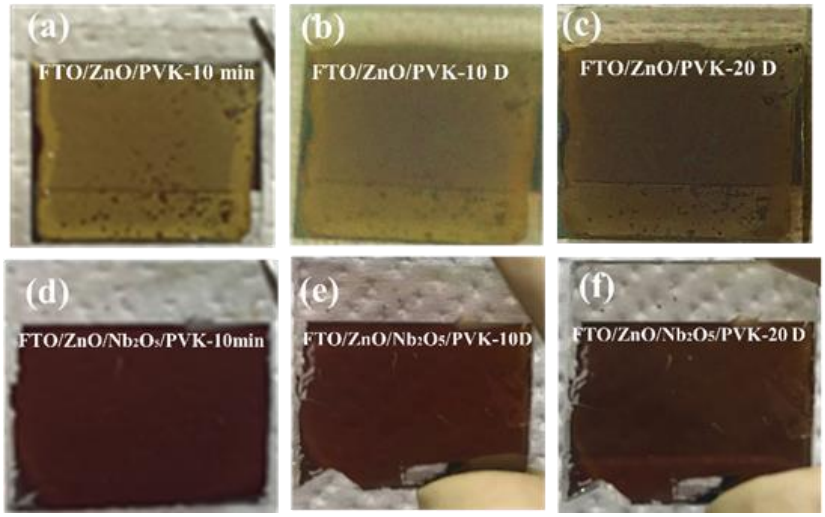

Figure 4-4 Photographs indicating the stability of perovskite absorber layer on to FTO/ZnO (a) after 10 min, (b) after 10 days and (c) 20 days. The same fabricated on FTO/ZnO/Nb_2O_5 substrates after their storage for 10 min (d), 10 days (e) and 20 days (f) in dark under ambient conditions.

It is worth to mention here that PVK films were fabricated by implementing one-step deposition process including anti-solvent dripping for acquiring large and pinhole free grains, which is considered to be more efficient, faster and simpler than two-step fabrication of PVK absorber layer.[37-38] In addition, usually the two-step method requires baking on the hot plate twice, while the one-step method only needs to be baked once, and the process is simpler and saves the production cost.[39-41] In a previous report, perovskite absorber layer was directly fabricated onto a bare ZnO substrate along with reported high efficiency, most commonly used two-step fabrication of perovskite film deposition process was used. This indicates that unlike one-step perovskite film fabrication, two-step method is effective towards the protection of its degradation on the bare ZnO surface. This could be explained considering the fact that first deposition of PbI_2 in the two-step sequential deposition process passivates the ZnO surface (acetate ligands or hydroxyl groups) layer at the interface of metal oxide and perovskite. This clearly indicates that by avoiding direct contact between perovskite and ZnO could effectively relieve perovskite decomposition. In the similar manner, Nb_2O_5 used in this present work plays the role of surface passivation, separates the direct contact between ZnO and PVK layer, and screens the damage of PVK layer by ZnO. Apart from this, it was also noticed that ZnO/Nb_2O_5/PVK films have pronounced resistance for atmospheric decomposition and fabricated films retain their original color over 20 days stored in dark under ambient conditions with humidity about 50%at room temperature (see Figure 4-4).

In order to investigate about the differential nature of the perovskite films formed on the bare ZnO and Nb_2O_5 layer passivated ZnO, XRD analysis was performed. XRD patterns of PVK on single layer ZnO and double layer Nb_2O_5/ZnO was recorded and results are shown in the Figure 4-2c. Diffraction peaks for different crystallographic planes along

with crystalline components originated from the substrates have been marked with different symbols. The diffraction peaks located at 26.48°, 37.78° and 51.57° can be indexed to the FTO substrate.[42] A diffraction peaks appearing at 36.26° and 47.54° can be assigned to the (101) and (102) planes of ZnO.[43] The appearance of a series of diffraction peaks at 14.17°, 20.04°, 23.59°, 24.56°, 28.24°, 28.52°, 31.03°, 31.94°,40.55°, 43.22° and 50.25° can be indexed to the (110), (112), (211), (202), (004), (220), (213), (222), (224), (314) and (404) planes of $CH_3NH_3PbI_3$, respectively, which is in accordance with the literature data for the tetragonal phase of the $CH_3NH_3PbI_3$ perovskite[87]4. For the XRD pattern of FTO/ZnO/PVK film a strong diffraction peak appearing at 12.70° and another weak peak at 39.58° belong to PbI_2 (red pattern in Figure 4-2c). The peak at 12.70° is very strong, indicating about the presence of large amount of PbI_2 generated in the sample of FTO/ZnO/PVK associated with decomposition of perovskite. On the other hand, FTO/ZnO/Nb_2O_5/PVK films a very weak diffraction peak associated with PbI_2 was observed at the same position. This confirms that the Nb_2O_5 passivation layer on ZnO surface plays a key role towards prevention of the perovskite decomposition. Change in the surface morphology of PVK layer was also noticed for the PVK films formed on the ZnO surface before and after Nb_2O_5 surface passivation as observed from SEM image shown in the Figure 4-2d. It can be clearly seen that a highly dense perovskite film was formed in the case of FTO/ZnO/Nb_2O_5/PVK. In contrast, perovskite film deposited directly on non-passivated bare ZnO exhibits surface with large roughness and poor coverage which might be associated with the perovskite decomposition. The perovskite deposited on Nb_2O_5 passivation layer shows a much smoother and more continuous surface than deposited on ZnO directly.

Table 1. Influence of ZnO layer thickness on the photovoltaic parameters for PSCs fabricated uisng Nb_2O_5 surface passivated ZnO. Values shown are the average value for 10 independent devices under each category and in parantyheses are standard deviations.

ZnO thickness	**J_{SC}/ mA·cm^{-2}**	**V_{OC} / V**	**FF**	**PCE/ %**
17 nm	17.27 (±1.76)	0.99 (±0.02)	0.61 (±0.04)	10.33 (±1.04)
28 nm	18.07 (±1.72)	1.00 (±0.03)	0.64 (±0.04)	11.49 (±1.24)
42 nm	21.01 (±1.02)	1.00 (±0.02)	0.64 (±0.03)	13.56 (±0.69)
60 nm	19.58 (±1.24)	1.00 (±0.02)	0.63 (±0.04)	12.28 (±0.46)

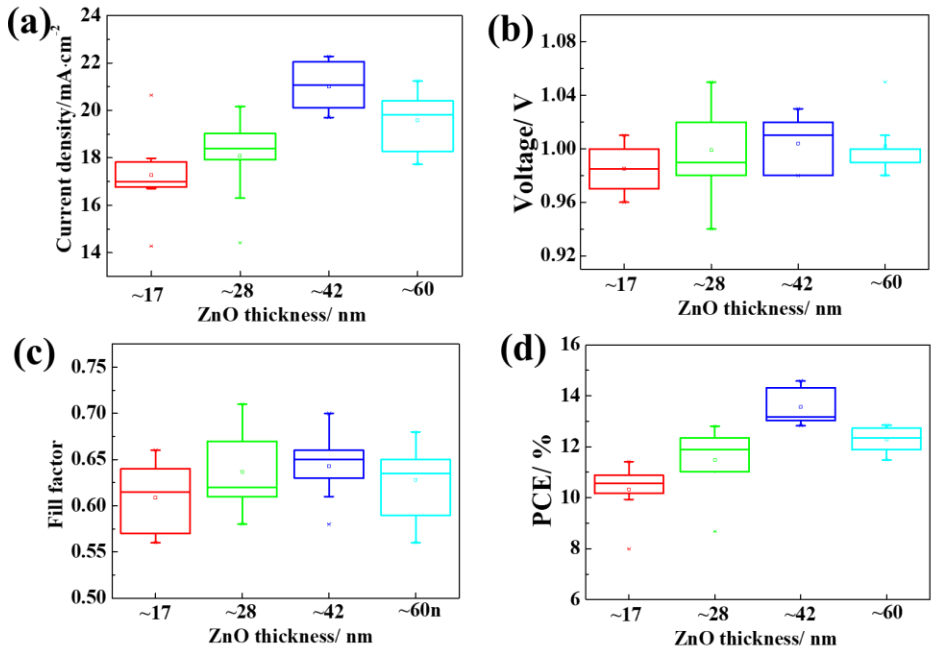

Figure 4-5 Photovoltaic parameters for 10 independent devices based on different thickness of ZnO and measured using a black metal mask with an illumination area of 0.10 cm^2.

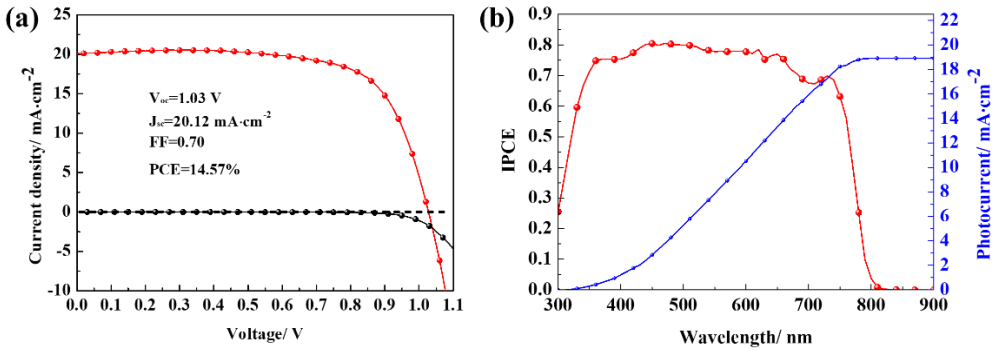

Figure 4-6 (a) J-V curve for the optimized PSC measured under simulated solar irradiation (1-sun) with ZnO thickness of 42 nm. (b) IPCE as a function of monochromatic light irradiation recorded for the same solar cells along with integrated J_{SC} obtained from the respective IPCE spectrum.

In our present device architecture, ZnO functions as flat scaffold for perovskite layer and Nb_2O_5 as surface passivating agent. In order to optimize the photovoltaic performance of the perovskite solar fabricated in this work, thickness of ZnO layer was systematically varied from 17 to 60 nm while keeping other parameters like Nb_2O_5 surface passivation and perovskite precursor conditions the same. Figure 4-5 shows the dependence of photovoltaic parameters like short-circuit current density (J_{SC}), open-circuit voltage (V_{OC}), fill factor (FF) and power conversion efficiency (PCE) on the thickness of ZnO layer for 10 devices in each thickness category. Average value for all of the photovoltaic parameters along with standard deviations as function of ZnO layer thickness are listed in the Table 1. A perusal of the table 1 clearly corroborates that for the ZnO layer thickness of about 17 nm, the average device efficiency was 10.33% with J_{SC} and V_{OC} values of 17.27 $mA \cdot cm^{-2}$ and 0.99 V, respectively. All of the photovoltaic parameters like, J_{SC}, V_{OC}, FF and PCE were found to increase as a function of increase in the thickness of ZnO layer up to about 40 nm followed by a slight decrease. Optimum ZnO layer thickness was found to 42 nm giving best photovoltaic performance with J_{SC}, V_{OC}, FF and PCE of 21.01 $mA \cdot cm^{-2}$, 1.0 V, 0.64 and 13.56%, respectively. Further increases in the thickness of the ZnO layer was proved not good due to decrease in the J_{SC} and FF. A poor performance in case of a very thin ZnO layer of 17 nm might be due to the inefficient coverage FTO surface and presence of pinholes. Upon increasing the thickness of thickness ZnO layer up to 42 nm, there is a possibility of decrease in pinhole density and enhanced FTO surface coverage by ZnO leading to improved solar cell performance. In the case of increasing the thickness of the ZnO beyond 42 nm especially for 60 nm of ZnO, there might be possibility of increase in the film resistance, which in turn decreases J_{SC} and FF, which is clear from the Figure 4-5 as well as table 1. Figure 4-6a shows the photovoltaic performance for our optimized and best perovskite solar cell with a device structure of

FTO/ZnO/Nb_2O_5/$CH_3NH_3PbI_3$/Sprio-OMeTAD/Au, under AM 1.5G solar irradiation of 100 mW·cm^{-2}. Under simulated solar irradiation, this solar cell exhibits a high PCE of 14.57% with a V_{OC} of 1.03 V, J_{SC} of 20.12 mA·cm^{-2} and FF of 0.70. It can be seen that in this newly designed PSC the efficiency of the optimized device is mainly attributed to the higher J_{SC} and FF. The corresponding photocurrent action spectrum for this device and integrated J_{SC} of 19 mA·cm^{-2} (from action spectrum) as shown in Figure 4-6b validates the accuracy of photovoltaic measurement obtained for simulated 1-Sun irradiation. From this figure, we can clearly observe that the entire visible region was covered efficiently with the IPCE spectrum approaching 80% in the range of 400 ~ 650 nm.

4.4. Conclusions

In summary, fabrication of an efficient planar-heterojunction PSC based on $CH_3NH_3PbI_3$ has been successfully demonstrated by tuning the interfacial properties of ZnO electron transport layer using an ultrathin Nb_2O_5 layer as a surface modifier. Our results indicates that once the surface properties of low temperature sol-gel processed ZnO layer was engineered by the ultrathin Nb_2O_5 passivation layer, it resulted in to an efficient electron transport layer in PSCs. The ultrathin Nb_2O_5 passivation layer effectively prevents direct contact between the ZnO and perovskite and prevents the decomposition of perovskite light absorber coated over ZnO. Importance of an efficient Nb_2O_5 surface passivation of ZnO layer in planer heterojunction PSC with dramatic enhancement in the device performance up to 14.57% and perovskite material stability beyond 20 days under ambient conditions have been clearly demonstrated. Moreover, our results explore that modified ZnO semiconductor could be an alternative to TiO_2 as electron transport layers in PSCs, especially for low temperature processed photovoltaic solar cells.

4.5 References

[1] Y. Cai; Zhang, Z.; Zhou, Y.; Liu, H.; Qin, Q.; Lu, X.; Gao, X.; Shui, L.; Wu, S.; Liu, J., Electrochim. Acta 261 (2018) 445-453.

[2] Y. Jiang; Leyden, M.R.; Qiu, L.; Wang, S.; Ono, L.K.; Wu, Z.; Juarez‐Perez, E.J.; Qi, Y., Adv. Funct. Mater. 28 (2018) 1870007.

[3] S.D. Stranks; Eperon, G.E.; Grancini, G.; Menelaou, C.; Alcocer, M.J.; Leijtens, T.; Herz, L.M.; Petrozza, A.; Snaith, H.J., Science 342 (2013) 341-344.

[4] G.W. Adhyaksa; Johlin, E.; Garnett, E.C., Nano Lett. 17 (2017) 5206-5212.

[5] W. Nie; Tsai, H.; Blancon, J.C.; Liu, F.; Stoumpos, C.C.; Traore, B.; Kepenekian, M.; Durand, O.; Katan, C.; Tretiak, S., Adv. Mater. 30 (2018) 1703879.

[6] W. Zhang; Ren, Z.; Guo, Y.; He, X.; Li, X., Electrochim. Acta 268 (2018) 539-545.

[7] W.S. Yang; Park, B.-W.; Jung, E.H.; Jeon, N.J.; Kim, Y.C.; Lee, D.U.; Shin, S.S.; Seo, J.; Kim, E.K.; Noh, J.H., Science 356 (2017) 1376-1379.

[8] A. Kojima; Teshima, K.; Shirai, Y.; Miyasaka, T., J. Am. Chem. Soc. 131 (2009) 6050-6051.

[9] S.I. Seok; Grätzel, M.; Park, N.G., Small 14 (2018) 1704177.

[10] J.-H. Im; Lee, C.-R.; Lee, J.-W.; Park, S.-W.; Park, N.-G., Nanoscale 3 (2011) 4088-4093.

[11] P. Zhang; Hu, Z.; Wang, Y.; Qin, Y.; Li, W.; Wang, J., Nano-micro letters 8 (2016) 232-239.

[12] A. Mei; Li, X.; Liu, L.; Ku, Z.; Liu, T.; Rong, Y.; Xu, M.; Hu, M.; Chen, J.; Yang, Y., Science 345 (2014) 295-298.

[13] P.-Y. Gu; Wang, N.; Wang, C.; Zhou, Y.; Long, G.; Tian, M.; Chen, W.; Sun, X.W.; Kanatzidis, M.G.; Zhang, Q., Journal of Materials Chemistry A 5 (2017) 7339-7344.

[14] G. Niu; Wang, S.; Li, J.; Li, W.; Wang, L., Journal of Materials Chemistry A 6 (2018) 4721-4728.

[15] T. Wu; Wu, J.; Tu, Y.; He, X.; Lan, Z.; Huang, M.; Lin, J., J. Power Sources 365 (2017) 1-6.

[16] F. Zhao; Dai, S.; Wu, Y.; Zhang, Q.; Wang, J.; Jiang, L.; Ling, Q.; Wei, Z.; Ma, W.; You, W., Adv. Mater. 29 (2017) 1700144.

[17] S. Intermite; Arbizzani, C.; Soavi, F.; Gholipour, S.; Turren-Cruz, S.-H.; Correa-Baena, J.P.; Saliba, M.; Vlachopoulos, N.; Ali, A.M.; Hagfeldt, A., Electrochim. Acta 258 (2017) 825-833.

[18] C. Liu; Yang, Y.; Ding, Y.; Xu, J.; Liu, X.; Zhang, B.; Yao, J.; Hayat, T.; Alsaedi, A.; Dai, S., ChemSusChem 11 (2018) 1232-1237.

[19] D. Shi; Adinolfi, V.; Comin, R.; Yuan, M.; Alarousu, E.; Buin, A.; Chen, Y.; Hoogland, S.; Rothenberger, A.; Katsiev, K., Science 347 (2015) 519-522.

[20] Q. Dong; Fang, Y.; Shao, Y.; Mulligan, P.; Qiu, J.; Cao, L.; Huang, J., Science 347 (2015) 967-970.

[21] Z.-L. Tseng; Chiang, C.-H.; Chang, S.-H.; Wu, C.-G., Nano Energy 28 (2016) 311-318.

[22] P. Zhang; Wu, J.; Zhang, T.; Wang, Y.; Liu, D.; Chen, H.; Ji, L.; Liu, C.; Ahmad, W.; Chen, Z.D., Adv. Mater. 30 (2018) 1703737.

[23] Q. An; Fassl, P.; Hofstetter, Y.J.; Becker-Koch, D.; Bausch, A.; Hopkinson, P.E.; Vaynzof, Y., Nano Energy 39 (2017) 400-408.

[24] J. Yang; Siempelkamp, B.D.; Mosconi, E.; De Angelis, F.; Kelly, T.L., Chem. Mater. 27 (2015) 4229-4236.

[25] R. Azmi; Hadmojo, W.T.; Sinaga, S.; Lee, C.L.; Yoon, S.C.; Jung, I.H.; Jang, S.Y., Advanced Energy Materials 8 (2018) 1701683.

[26] J. Cao; Wu, B.; Chen, R.; Wu, Y.; Hui, Y.; Mao, B.W.; Zheng, N., Efficient, Adv. Mater. 30 (2018) 1705596.

[27] L. Zuo; Gu, Z.; Ye, T.; Fu, W.; Wu, G.; Li, H.; Chen, H., J. Am. Chem. Soc. 137 (2015) 2674-2679.

[28] J. Kim; Kim, G.; Kim, T.K.; Kwon, S.; Back, H.; Lee, J.; Lee, S.H.; Kang, H.; Lee, K., Journal of Materials Chemistry A 2 (2014) 17291-17296.

[29] T. Stubhan; Salinas, M.; Ebel, A.; Krebs, F.C.; Hirsch, A.; Halik, M.; Brabec, C.J., Advanced Energy Materials 2 (2012) 532-535.

[30] Q. Hu; Wu, J.; Jiang, C.; Liu, T.; Que, X.; Zhu, R.; Gong, Q., ACS nano 8 (2014) 10161-10167.

[31] J. Dong; Zhao, Y.; Shi, J.; Wei, H.; Xiao, J.; Xu, X.; Luo, J.; Xu, J.; Li, D.; Luo, Y., Chem. Commun. 50 (2014) 13381-13384.

[32] X. Ling; Yuan, J.; Liu, D.; Wang, Y.; Zhang, Y.; Chen, S.; Wu, H.; Jin, F.; Wu, F.; Shi, G., ACS applied materials & interfaces 9 (2017) 23181-23188.

[33] A. Le Viet; Jose, R.; Reddy, M.; Chowdari, B.; Ramakrishna, S., The Journal of Physical Chemistry C 114 (2010) 21795-21800.

[34] K. Eguchi; Koga, H.; Sekizawa, K.; Sasaki, K., J. Ceram. Soc. Jpn. 108 (2000) 1067-1071.

[35] R. Azmi; Aqoma, H.; Hadmojo, W.T.; Yun, J.M.; Yoon, S.; Kim, K.; Do, Y.R.; Oh, S.H.; Jang, S.Y., Advanced Energy Materials 6 (2016) 1502146.

[36] F. Yang; Kapil, G.; Zhang, P.; Hu, Z.; Kamarudin, M.A.; Ma, T.; Hayase, S., ACS applied materials & interfaces 10 (2018) 16482-16489.

[37] N.J. Jeon; Noh, J.H.; Kim, Y.C.; Yang, W.S.; Ryu, S.; Seok, S.I., Nature materials 13 (2014) 897.

[38] N.J. Jeon; Noh, J.H.; Yang, W.S.; Kim, Y.C.; Ryu, S.; Seo, J.; Seok, S.I., Nature 517 (2015) 476.

[39] Y. Zhao; Zhu, K., The Journal of Physical Chemistry C 118 (2014) 9412-9418.

[40] D. Prochowicz; Yadav, P.; Saliba, M.; Kubicki, D.J.; Tavakoli, M.M.; Zakeeruddin, S.M.; Lewiński, J.; Emsley, L.; Grätzel, M., Nano energy 49 (2018) 523-528.

[41] M. Wang; Feng, Y.; Bian, J.; Liu, H.; Shi, Y., Chem. Phys. Lett. 692 (2018) 44-49.

[42] X. Yang; Hu, L.; Deng, H.; Qiao, K.; Hu, C.; Liu, Z.; Yuan, S.; Khan, J.; Li, D.; Tang, J., Nano-micro letters 9 (2017) 24.

[43] J. Qiu; Qiu, Y.; Yan, K.; Zhong, M.; Mu, C.; Yan, H.; Yang, S., Nanoscale 5 (2013) 3245-3248.

Chapter 5. Preparation of perovskite films under liquid nitrogen atmosphere for high efficiency perovskite solar cells

5.1 Introduction

In recent few years, perovskite solar cells (PSCs) have gained great attention owing to the long diffusion length, suitable band gap, and of the superior carrier mobility perovskite materials.[1-2] Miyasaka research group first reported the efficiency of 3.8% liquid-electrolyte-based PSCs in 2009,[3] which within a few short years reached an efficiency over 23%.[4] The key factor for getting high performance PSCs is to control the morphology for getting high quality of perovskite layer. Various preparation ways or deposition techniques are introduced to prepare high-quality perovskite films, such as interface engineering,[5] solvent engineering,[6-7] composition modulation[8-9] and so on.[10-14] All of these methods are based on crystal nucleation-growth theory to control the morphology of the film.[15-17] According to the crystal nucleation-growth theory and previous reports, rapid nucleation and slow growth are the key factors for obtaining dense and smooth perovskite films.[18-19] In an one-step anti-solvent method, Dai et al.[20] have reported the method to enhance the perovskite films` quality through lowering the anti-solvent`s temperature. The low-temperature anti-solvent not only removes the excess solvent from the perovskite precursor solution to increase the precursor concentration, but also lowers the temperature on the substrate, allowing the perovskite precursor film to reach super-cooling quickly, thereby facilitating rapid nucleation. By this method they have improved the surface coverage of perovskite layer. Furthermore, the speed of crystal growth is also playing an important role for the film. If the grain growth is too

fast, it will lead to a film with high defect density.[21] Zhu et al. has experimentally added $MAPbCl_3$ to the perovskite precursor.[22] In this case the crystal growth rate is effectively reduced, and a well-formed perovskite film is obtained. However, preparation of high-coverage and low-defect perovskite films still poses great challenges. In this study, a liquid nitrogen assisted one-step anti-solvent process was used to prepare perovskite films. The volatile liquid nitrogen takes away the heat from the perovskite precursor film, accelerating the rapid nucleation process of the perovskite. Through this process, a pinhole-free smooth and dense perovskite film was obtained. The average PCE of the regular mesoporous structure devices by incorporating these high-quality perovskite films significantly improved from the initial 14.50% to 15.54% and the champion device in this work shows the highest PCE of 16.53%. 89% of the initial performance was retained even after 30 days of cell fabrication.

5.2 Results and discussion

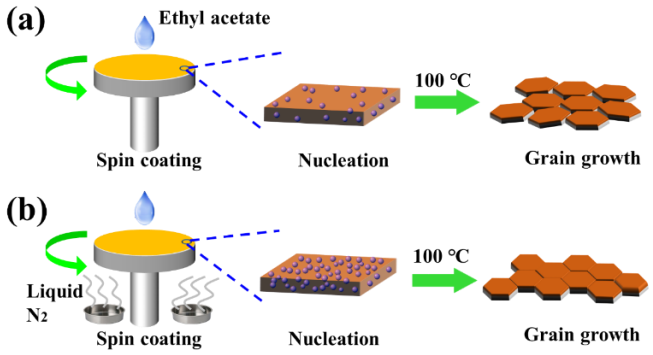

Figure 5-1 Fabricating perovskite films method of conventional one-step spin-coating process (a) and liquid nitrogen assisted process (b). Conventional one-step spin-coating method usually results in rich defects at a grain boundary, where non-uniform large crystals from a result of slow nucleation. In the liquid nitrogen assisted method (NL method), perovskite precursor solution can easily reach below the degree of undercooling, and rapidly and massively nucleate, thereby forming densely arranged grains of film.

The one-step spin-coating anti-solvent method for preparing the $CH_3NH_3PbI_3$ layer is shown in Figure 5-1. In the conventional process (a), a perovskite precursor solution was spin-coated on the TiO_2 substrate at 4000 rpm. After a delay time for 10 s, ethyl acetate anti-solvent was dripped on the substrates. The anti-solvent reduces the solubility of perovskite in the precursor film, promoting growth of the crystals and fast nucleation in the film. After annealed at 100 ℃ on a hot plate for 10 min to evaporate the residual solvent and further promote crystal growth, the perovskite film was achieved. While in the liquid nitrogen assist process (b), liquid nitrogen is used as an aid, as shown in Figure 5-2, two stainless steel petri dishes filled with liquid nitrogen were placed under the spinner. It is noted that the spin-coating instrument accelerates the volatilization of liquid nitrogen during high-speed rotation. Therefore, sufficient liquid nitrogen should be injected into the stainless steel petri dishes before spin coating to ensure continuous liquid nitrogen volatilization during spin coating. The low-temperature nitrogen evaporated from liquid N_2 allows the perovskite to nucleate rapidly on the precursor film. The crystal grows after baking to form a dense perovskite film. According to the previous reports, during the preparation of perovskite film, the slow nucleation leads to large grain boundaries and poor film coverage in the films.[18-23] To solve this problem, researchers have tried to improve the film preparation by different anti-solvents.[24] The anti-solvent allows the initial solution to quickly reach supersaturation, which in turn promotes nucleation. As is well known, the key factors affecting crystal nucleation are supersaturation and undercooling. In this study, the liquid nitrogen assisted process effectively reduces the surface temperature of the precursor film to reach the nucleation critical state, and promoting a large number of nucleation in a short time.

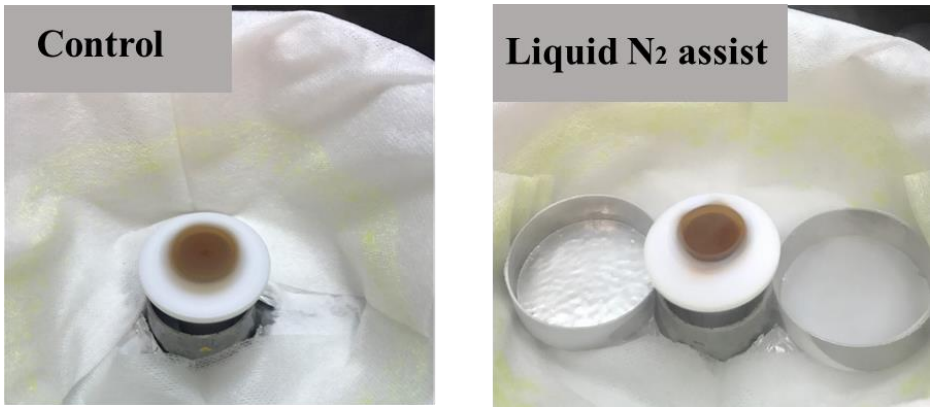

Figure 5-2 One-step anti-solvent method for preparing perovskite films. (a) Conventional process and (b) liquid nitrogen assist process, the ambient temperature is about 23 ℃ and the temperature during spin-coating was about 4 ℃.

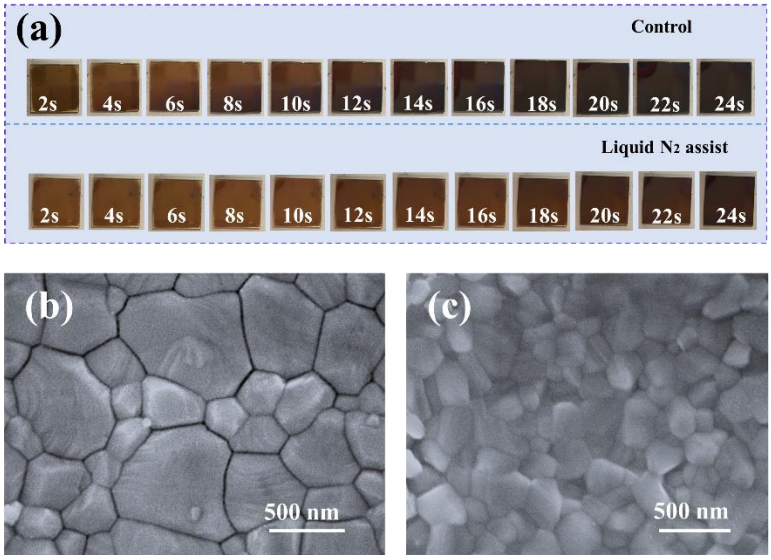

Figure 5-3 (a) Photographs of perovskite $CH_3NH_3PbI_3$ films during annealing process at 100 °C. Top-view SEM images of $CH_3NH_3PbI_3$ layers deposited on TiO_2/FTO: (b) control, (c) LN method.

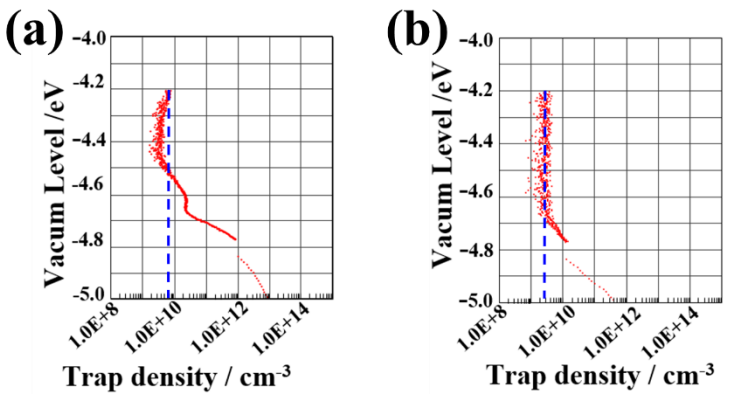

Figure 5-4 Trap distribution on perovskite films. (a) Control and (b) LN method.

Figure 5-3 (a) presents a comparison of perovskite films prepared by conventional processes and LN process. Compared with the controlled group, the perovskite film prepared by LN method took a longer time to complete the crystallization process, resulting in high quality morphology densely packed grains in the perovskite films. The top-view SEM images of the $CH_3NH_3PbI_3$ layers are illustrated in Figure 5-3b-c. As can be seen in Figure 5-3b, the perovskite films with big grains and significant grain boundary defects are formed by the conventional process. In general, a perovskite film with a large crystal is more advantageous for charge transport, but due to a large number of grain boundary defects, the performance of the device is not ideal.[25] Large grain boundary defects might cause direct contact between the electron transporting layer and the hole transporting layer, which cause charge leakage and non-radiative recombination.[26] However, as shown in Figure 5-3c, a close-grained perovskite film can be obtained by a liquid nitrogen assist method. The grains of this dense perovskite film were almost linked together without large gap between grains, which reduces the carrier's non-radiative recombination and promotes the efficient transmission of charges in the device.[27] Thermally stimulated current (TSC) was introduced to explore the trap density of $CH_3NH_3PbI_3$

layers. TSC is a powerful measuring tool to investigate the trap distribution of the trapped charge carriers within the perovskite material. Generally, the carrier traps are priorly cooled to the temperature of liquid nitrogen, followed by the filling of carriers generated from the electrodes under a small forward bias. The trapped carries are subsequently released and obtained through slowly rising up the temperature at a continuous speed of 2 ºC/min under a small reverse bias, which gives rise to the TSC curves.[28] The results are shown in Figure 5-4. The conduction band level of $CH_3NH_3PbI_3$ is -3.93 eV from vacuum level, for control group trap density at -4.2 eV was $5\times10^9/cm^3$, as shown in Figure 5-4a. While, trap density of perovskite film prepared by LN method decreased significantly, was about was $2\times10^9/cm^3$ at the same level (see Figure 5-4b).

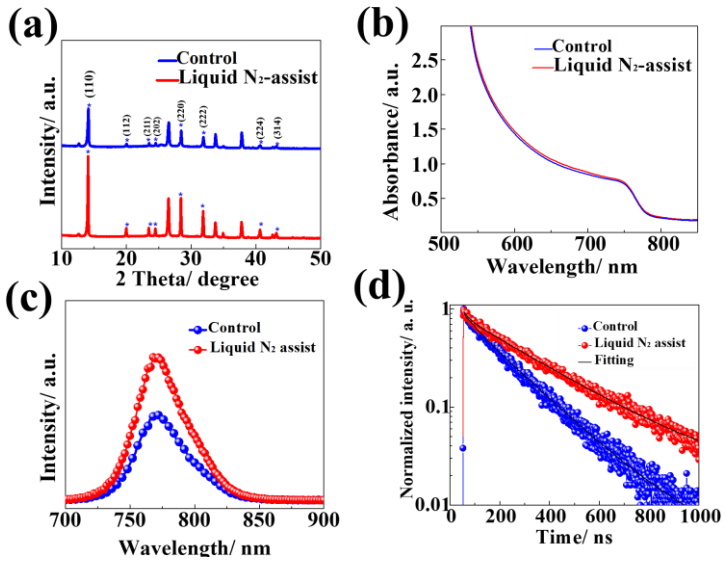

Figure 5-5. (a) X-ray diffraction spectra and (b) Ultraviolet–visible spectroscopy absorption spectra of $CH_3NH_3PbI_3$ layers prepared on TiO_2 with or without liquid nitrogen assistance. (c) PL spectra and (d) TRPL spectra of the glass/$CH_3NH_3PbI_3$ films.

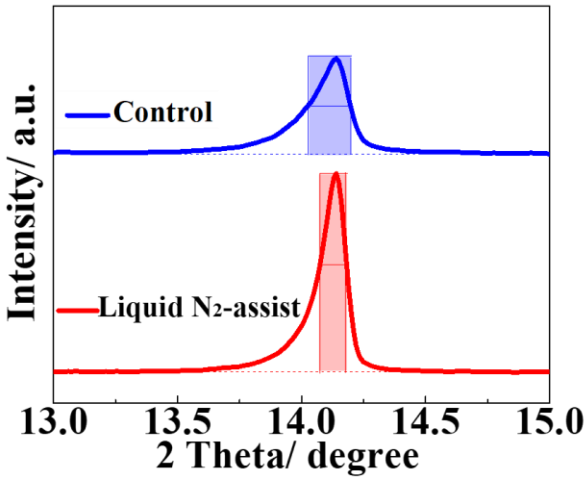

Figure 5-6 X-ray diffraction spectra of $CH_3NH_3PbI_3$ perovskite films prepared by conventral process and liquid nitrogen assisted process. The full width at half maximum (FWHM) of peak at 14.17°。

The crystalline properties of perovskite films were further recorded by XRD. As shown in Figure 5-5a, the X-ray patterns of perovskite layers prepared with or without liquid nitrogen assistance displayed typical diffraction peaks of $CH_3NH_3PbI_3$ perovskite phase. The diffraction peaks at 14.17, 20.04, 23.59, 24.56, 28.52, 31.94, 40.55 and 43.22°, can be assigned to the (110), (112), (211), (202), (220), (222), (224) and (314) planes of the tetragonal $CH_3NH_3PbI_3$ structure.[29] The intensity of the perovskite peaks (red) was significantly enhanced and full width at half maximum (FWHM) was narrow than that of control (see Figure 5-6). This suggests film crystallinity prepared by the LN method is better than that of control. The good crystallinity of perovskite film led to good optical properties. As shown in Figure 5-5b, the perovskite film prepared by LN method showed almost the same absorption. The high-quality perovskite film as described above can transport carriers more effectively and effectively reduce charge

recombination as well. Next, the steady-state photoluminescence (PL) and time-resolved photoluminescence (TRPL) test were performed on the perovskite film. The results are shown in Figure 5-5c and d. Compared with the control group, it can be found that the PL peak of the film prepared by LN process was stronger. This means that the film prepared by the LN method has a higher quality. The TRPL results are shown in Figure 5-5d. The film prepared by LN process had a carrier lifetime of 61.2 ns, which is much longer than that of the control group (27.9 ns). Therefore, the LN method effectively increased the carrier lifetime of perovskite films, which is agreed with the photoluminescence spectra.

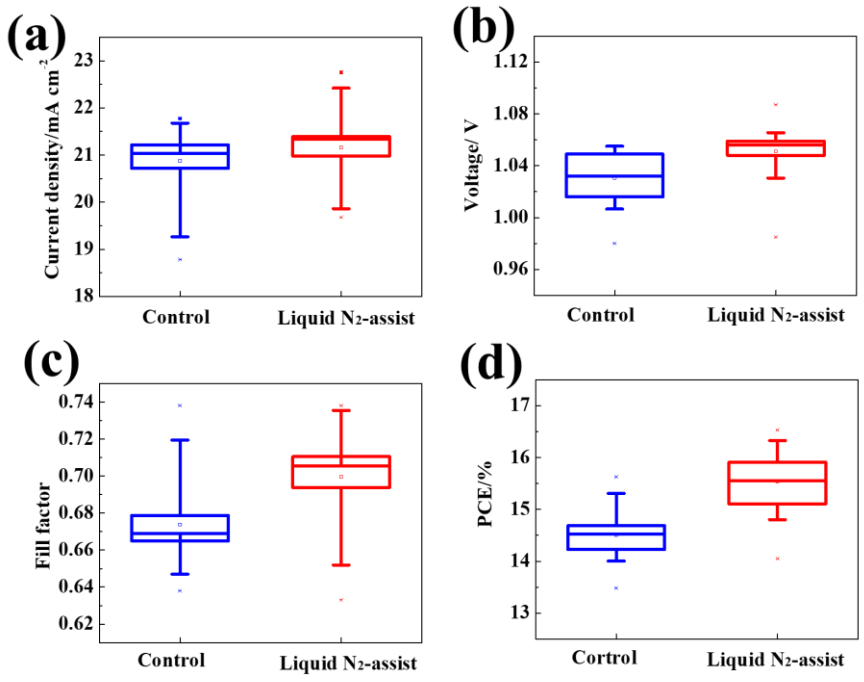

Figure 5-7. Photovoltaic statistics of two group perovskite solar cells. (a) J_{SC}, (b) V_{OC}, (c) FF, (d) PCE. Statistical analysis of data from 30 cells of each group.

Figure 5-7 (a-d) show the photovoltaic statistics of two group perovskite solar cells with the structure FTO/c-TiO_2/m-TiO_2/$MAPbI_3$/HTL/Au. The devices parameters showed that

the LN method can effectively improve all the photovoltaic parameters of PSCs including J_{SC}, V_{OC} and FF. The schematic of device structure and cross-section SEM image of the completed devices, as shown in Figure 5-7a-b. As mentioned above, the closely arranged grain and high-quality perovskite films prepared by the LN method result in higher J_{SC}. In addition, fewer grain boundary pinholes can effectively avoid contact between hole transporting layer and electron transporting layer (see Figure 5-7c-d), which can reduce electric leakage, and reduce carrier recombination, improving both V_{OC} and FF.[30]

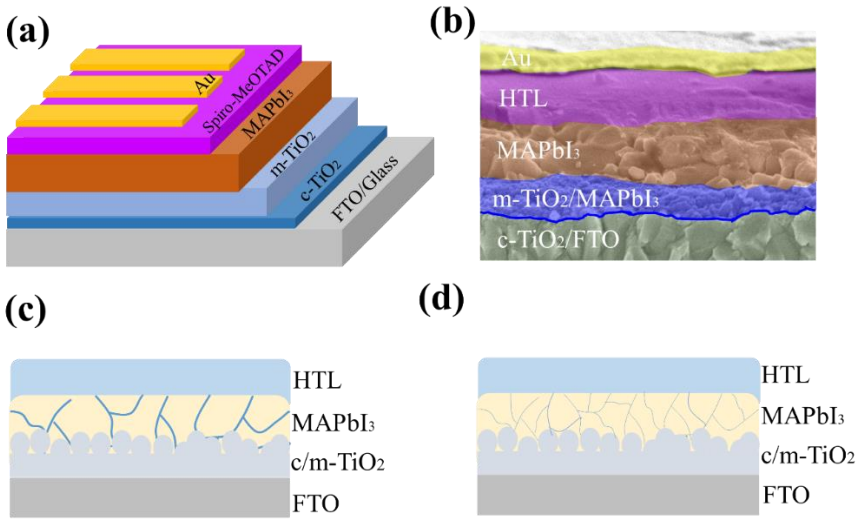

Figure 5-8 (a) Device structure of FTO/c-TiO_2/m-TiO_2/$MAPbI_3$/HTL/Au PSCs and (b) cross-section SEM image of the completed devices. Cross sectional structure of perovskite film prepared by (c) conventional process with large grain boundary pin holes and (d) LN method with small grain boundary defects.

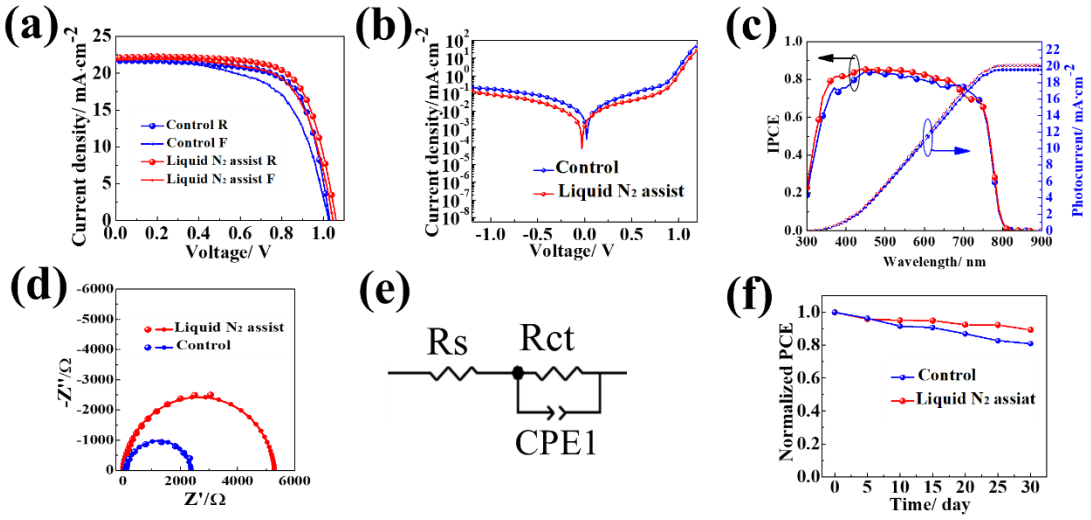

Figure 5-9 The illuminated (a) and dark (b) Current-voltage characteristics and (c) EQE spectra of the champion PSCs based conventional method and LN method. (d) Nyquist plots of PSCs measured with an applied bias of 0.6 V in dark condition and (e) an equivalent circuit. (f) Stability test for control and liquid nitrogen assisted perovskite solar cells.

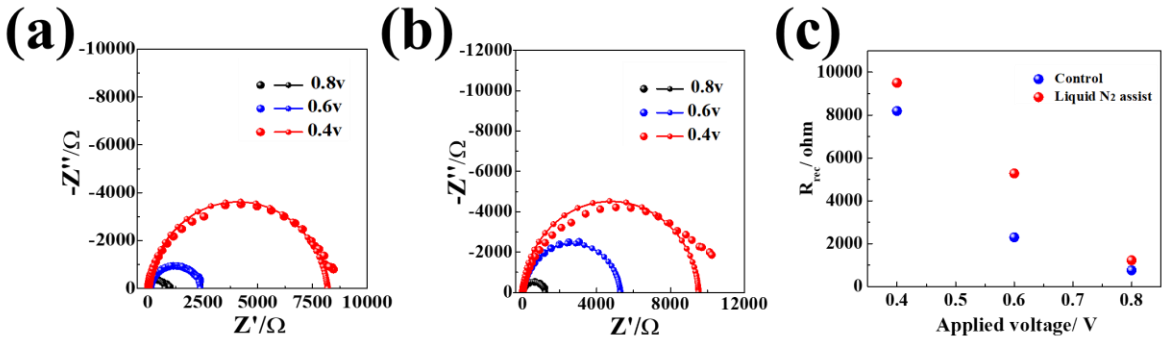

Figure 5-10 Nyquist plots of perovskite solar cells based on $CH_3NH_3PbI_3$ measured in dark condition with different applied bias (0.4, 0.6 and 0.8 V). (a) Control group and (b) liquid nitrogen assisted group. (c) Charge recombination (Rrec) resistance extracted from EIS measurements at different applied bias.

Figure 5-9 (a) illustrates the J-V characteristics of champion PSCs prepared using conventional way and LN method, tested under reverse and forward voltage. The device prepared by conventional method (blue curve) achieved a PCE of 15.63 (13.66) %, with a V_{OC} of 1.03 (1.02) V, J_{SC} of 21.69 (21.68) $mA \cdot cm^{-2}$, and FF of 0.70 (0.62) measured under reverse (forward) direction, showing a large hysteresis. While the device prepared by LN method (red curve) achieved a PCE of 16.53 (15.71) %, with a V_{OC} of 1.06 (1.05) V, a J_{SC} of 22.19 (21.77) $mA \cdot cm^{-2}$ and a FF of 0.70 (0.69) measured under reverse (forward) direction, revealing a decreased hysteresis and an enhanced efficiency. Due to the excellent quality $CH_3NH_3PbI_3$ layer prepared by the LN method, there are no pinholes, and less grain boundary defects, which reduces the carrier recombination sites and reduces the hysteresis. The PCE enhancement is mainly attributed to the improvement in J_{SC} and V_{OC}. The high quality film with less grain boundary pin holes will reduce the shunt pathways and effectively block electrons on the $TiO_2/CH_3NH_3PbI_3$ interface to decrease electron-hole recombination (see Figure 5-8a, b). It can also be seen in the dark current curve (Figure 5-9 b), that the dark current of the LN device was lower than that of the control device, thereby leading to a larger V_{OC} of the device prepared by liquid nitrogen assisted method.[31] Figure 5-9 (c) shows the IPCE spectra of the champion devices. The integrated current densities were 20.10 and 19.58 $mA \cdot cm^{-2}$ for control and liquid nitrogen assisted devices, respectively. Electrochemical impedance spectrum (EIS) is an effective method to study the charge recombination in devices. Figure 5-9 (d) presents the Nyquist plots of both devices carried out in the dark condition at an applied voltage of 0.6 V. The series resistance (Rs) and charge recombination resistance (R_{ct}) could be fitted by employing an equivalent circuit model (Figure 5-9e), in the equivalent circuit model.[32] As a result, the device prepared by liquid nitrogen assisted method has an R_{ct} of 5276 Ω, which is higher than conventional devices (2293 Ω), suggesting that electron recombination can be effectively

reduced. The Nyquist plots measured with different applied bias are displayed in Figure 5-10 a-b. According to the equivalent circuit model the corresponding results were plotted as shown in Figure 5-10 c. It can be seen that at the same applied bias, the LN group has a higher R_{ct}, which could explain the higher V_{OC} achieved from the current voltage measurements.[33] We examined the long-term stability of the PSCs. The stability measurement of the unencapsulated PSCs were performed in a desiccator with 20-40% humidity at room temperature for 30 days. As shown in Figure 5-9 (f), device prepared by the LN method showed a better stability, maintaining 89% of the initial PCE after 30 days of storage in desiccator, whereas the control group drop more of the initial efficiency under the same conditions.

5.3 Conclusions

In summary, we introduced an efficient and facile approach to prepare high quality perovskite film. During the process of perovskite nucleation, the LN method effectively reduces the ambient temperature, taking away heat from the substrate surface and accelerating the nucleation process. By observing the film morphology, we found that the LN method can produce pinhole-free, grain tightly arranged perovskite films. At last, an effective PCE of 16.53% was observed for the film prepared by the LN method. The performance could retain over 89% of the initial PCE after 30 days storage in 20-40% humidity air condition at room temperature.

5.4 References

(1) Bi, C.; Wang, Q.; Shao, Y.; Yuan, Y.; Xiao, Z.; Huang, J. Nature communications 2015, 6, 7747.

(2) Yang, F.; Kamarudin, M. A.; Zhang, P.; Kapil, G.; Ma, T.; Hayase, S. ChemSusChem 2018, 11, 2265-2265.

(3) Kojima, A.; Teshima, K.; Shirai, Y.; Miyasaka, T., J. Am. Chem. Soc. 2009, 131, 6050-6051.

(4) Jeon, N. J.; Na, H.; Jung, E. H.; Yang, T.-Y.; Lee, Y. G.; Kim, G.; Shin, H.-W.; Seok, S. I.; Lee, J.; Seo, J., Nature Energy 2018, 3, 682-689.

(5) Huang, L.-B.; Su, P.-Y.; Liu, J.-M.; Huang, J.-F.; Chen, Y.-F.; Qin, S.; Guo, J.; Xu, Y.-W.; Su, C.-Y., J. Power Sources 2018, 378, 483-490.

(6) Kim, Y. Y.; Park, E. Y.; Yang, T.-Y.; Noh, J. H.; Shin, T. J.; Jeon, N. J.; Seo, J., Journal of Materials Chemistry A 2018, 6, 12447-12454.

(7) Tu, Y.; Wu, J.; He, X.; Guo, P.; Wu, T.; Luo, H.; Liu, Q.; Wang, K.; Lin, J.; Huang, M. Journal of Materials Chemistry A 2017, 5, 4376-4383.

(8) Kim, J.; Saidaminov, M. I.; Tan, H.; Zhao, Y.; Kim, Y.; Choi, J.; Jo, J. W.; Fan, J.; Quintero-Bermudez, R.; Yang, Z., Adv. Mater. 2018, 30, 1706275.

(9) Tombe, S.; Adam, G.; Heilbrunner, H.; Yumusak, C.; Apaydin, D. H.; Hailegnaw, B.; Ulbricht, C.; Arendse, C. J.; Langhals, H.; Iwuohaa, E., Solar Energy 2018, 163, 215-223.

(10) Dong, H.; Wu, Z.; Xi, J.; Xu, X.; Zuo, L.; Lei, T.; Zhao, X.; Zhang, L.; Hou, X.; Jen, A. K. Y., Adv. Funct. Mater. 2018, 28, 1704836.

(11) Li, Y.; Li, Y.; Shi, J.; Zhang, H.; Wu, J.; Li, D.; Luo, Y.; Wu, H.; Meng, Q., Adv. Funct. Mater. 2018.10, 1705220.

(12) Fu, X.; Dong, N.; Lian, G.; Lv, S.; Zhao, T.; Wang, Q.; Cui, D.; Wong, C.-P., Nano Lett. 2018, 18, 1213-1220.

(13) Jiang, Y.; Tu, L.; Li, H.; Li, S.; Yang, S.-E.; Chen, Y., Crystals 2018, 8, 44.

(14) Ito, N.; Kamarudin, M. A.; Hirotani, D.; Zhang, Y.; Shen, Q.; Ogomi, Y.; Iikubo, S.; Minemoto, T.; Yoshino, K.; Hayase, S., The journal of physical chemistry letters 2018, 9, 1682-1688.

(15) LaMer, V. K.; Dinegar, R. H., J. Am. Chem. Soc. 1950, 72, 4847-4854.

(16) Wang, F.; Richards, V. N.; Shields, S. P.; Buhro, W. E., Chem. Mater. 2013, 26, 5-21.

(17) Luo, W.; Wu, C.; Sun, W.; Guo, X.; Xiao, L.; Chen, Z., ACS applied materials & interfaces 2017, 9, 26915-26920.

(18) Qin, P. L.; Yang, G.; Ren, Z. w.; Cheung, S. H.; So, S. K.; Chen, L.; Hao, J.; Hou, J.; Li, G. , Adv. Mater. 2018, 30, 1706126.

(19) Zhang, F.; Shi, W.; Luo, J.; Pellet, N.; Yi, C.; Li, X.; Zhao, X.; Dennis, T. J. S.; Li, X.; Wang, S., Adv. Mater. 2017, 29, 1606806.

(20) Ren, Y.-K.; Ding, X.-H.; Wu, Y.-H.; Zhu, J.; Hayat, T.; Alsaedi, A.; Xu, Y.-F.; Li, Z.-Q.; Yang, S.-F.; Dai, S.-Y., Journal of Materials Chemistry A 2017, 5, 20327-20333.

(21) Bai, S.; Sakai, N.; Zhang, W.; Wang, Z.; Wang, J. T.-W.; Gao, F.; Snaith, H. J., Chem. Mater. 2016, 29, 462-473.

(22) Zhao, Y.; Zhu, K., The Journal of Physical Chemistry C 2014, 118, 9412-9418.

(23) Hao, J.; Hao, H.; Cheng, F.; Li, J.; Zhang, H.; Dong, J.; Xing, J.; Liu, H.; Wu, J., J. Cryst. Growth 2018, 491, 66-72.

(24) Yang, F.; Kapil, G.; Zhang, P.; Hu, Z.; Kamarudin, M. A.; Ma, T.; Hayase, S., ACS applied materials & interfaces 2018.10, 16482-16489.

(25) Yang, M.; Zhang, T.; Schulz, P.; Li, Z.; Li, G.; Kim, D. H.; Guo, N.; Berry, J. J.; Zhu, K.; Zhao, Y., Nature communications 2016, 7, 12305.

(26) Long, R.; Liu, J.; Prezhdo, O.V., J. Am. Chem. Soc. 2016, 138, 3884-3890.

(27) Ng, A.; Ren, Z.; Li, G.; Djurišic, A. B.; Surya, C., International Society for Optics and Photonics. 2018; 10533, 105331Y.

(28) Qin, C.; Matsushima, T.; Fujihara, T.; Potscavage Jr, W. J.; Adachi, C., Adv. Mater. 2016, 28, 466-471.

(29) Yu, J.; Chen, X.; Wang, Y.; Zhou, H.; Xue, M.; Xu, Y.; Li, Z.; Ye, C.; Zhang, J.; Van Aken, P.A., Journal of Materials Chemistry C 2016, 4, 7302-7308.

(30) Cho, K. T.; Paek, S.; Grancini, G.; Roldán-Carmona, C.; Gao, P.; Lee, Y.; Nazeeruddin, M. K., Energy & Environmental Science 2017, 10, 621-627.

(31) Jhuo, H.-J.; Yeh, P.-N.; Liao, S.-H.; Li, Y.-L.; Sharma, S.; Chen, S.-A., Journal of Materials Chemistry A 2015, 3, 9291-9297.

(32) Jiang, L.-L.; Cong, S.; Lou, Y.-H.; Yi, Q.-H.; Zhu, J.-T.; Ma, H.; Zou, G.-F., Journal of Materials Chemistry A 2016, 4, 217-222.

(33) Jiang, X.; Yu, Z.; Zhang, Y.; Lai, J.; Li, J.; Gurzadyan, G. G.; Yang, X.; Sun, L., Scientific reports 2017, 7, 42564.

General conclusions

This thesis mainly focused on the interface passivation of various layers of perovskite solar cells and the preparation of high quality perovskite films. In the carbon electrode based perovskite solar cell, the perovskite light absorbing layer was prepared by one-step process and two-step process. The effect of PbI_2 on the surface of the carbon electrode on the performance of the device was investigated. In the solar cell of the gold electrode structure, surface passivation of the electron transport layer is effectively reduced by passivation of the electron transport layer, and device stability and device efficiency are improved. The main work is summarized as follows.

(1) The porous framework structure of TiO_2/ZrO_2/Carbon was prepared by spin coating and screen printing method. The perovskite light absorbing layer was prepared on the mesoporous structure by a one-step method and a two-step method. As a result, a PCE of 7.08% with two-step method was attained, better than one-step method (2.21%). Furthermore, a novel analysis method using QCM was reported, which is an effective technology to monitor the change of carbon electrode surface in carbon based PSCs. The results obtained from QCM demonstrate that PbI_2 loaded on the carbon surface can't be removed even after rinsing with solvent (DMF), the remnants were C-O-Pb linkages bonded covalently as confirmed from XPS and FTIR. It has been proven that passivation of carbon electrode is necessary to enhance the PCE, by reducing the recombination due to direct contact with absorber layer. The passivation using C-O-Pb was finally utilized successfully in fabricating the solar cells with improved PCE of 7.30% and 6.55%, employing two-step and one-step fabrication methods respectively.

(2) We demonstrated that the interface between the electron transporting layer and perovskite is important for device performance of perovskite solar cells. The thin SbI_3

passivation layer was prepared by a simple immersion method which can passivate the TiO_2 surface and thus effectively reduced the TiO_2 electronic trap states and enabled faster electron transport. QCM monitors of the adsorption of SbI_2 on TiO_2 surface, XPS and TSC result effectively proved that the surface trap concentration of TiO_2 after passivation was reduced. The solar cell efficiency with the SbI_3-passivated mesoporous TiO_2 electrodes was enhanced from 15.82% (15.04% in average) to over 17.33% (16.41% on average). Even after 60 days, the device still maintained more than 80% of the initial efficiency at air without encapsulation.

(3) Fabrication of an efficient planar-heterojunction PSC based on CH3NH3PbI3 has been successfully demonstrated by tuning the interfacial properties of ZnO electron transport layer using an ultrathin Nb_2O_5 layer as a surface modifier. Our results indicates that once the surface properties of low temperature sol-gel processed ZnO layer was engineered by the ultrathin Nb_2O_5 passivation layer, it resulted in to an efficient electron transport layer in PSCs. The ultrathin Nb_2O_5 passivation layer effectively prevents direct contact between the ZnO and perovskite and prevents the decomposition of perovskite light absorber coated over ZnO. Importance of an efficient Nb_2O_5 surface passivation of ZnO layer in planer heterojunction PSC with dramatic enhancement in the device performance up to 14.57% and perovskite material stability beyond 20 days under ambient conditions have been clearly demonstrated. Moreover, our results explore that modified ZnO semiconductor could be an alternative to TiO_2 as electron transport layers in PSCs, especially for low temperature processed photovoltaic solar cells.

Future Prospects

Organic-inorganic perovskite materials have excellent photoelectric properties. In the past 10 years, perovskite solar cells have made rapid progress. But perovskite solar cells are still a long way from real commercialization. Based on the understanding and consideration of perovskite solar cells, some prospects for perovskite solar cells are given below.

(1) We need to further improve the long-term stability of perovskite solar cells. Perovskite solar cells have achieved power conversion efficiencies of 23%, but their stability is far from comparable to commercially available silicon-based solar cells. Since the perovskite material itself is very sensitive to moisture, the water in the air easily decomposes the perovskite, resulting in partial or even complete failure of the perovskite solar cell. In order to improve stability, we can start from the following aspects. Improve the stability of the perovskite solar cell by adjusting the perovskite component. For example, perovskites are prepared using all inorganic materials; The stability of the perovskite solar cell is optimized by the interface, for example, passivation of the interface between the electron transport layer or the hole transport layer and the perovskite layer; Isolation of perovskite from air by optimizing the packaging means to improve the stability of the perovskite solar cell.

(2) We need to reduce the damage to the environment or the human body by perovskite materials. The perovskite material itself contains heavy metal element lead, which can cause harm to the environment and the human body. Therefore, we need to study less lead or lead-free perovskites. Tin and lead are homologous elements with similar properties and can partially or completely replace lead to reduce the toxicity of perovskite materials.

(3) We need to further reduce the production cost of perovskite solar cells. Conventional structures of perovskite solar cells usually use gold electrodes, gold itself is expensive, and its evaporation process is also a high energy process. Therefore, the development of low-cost perovskite devices is the only way to achieve commercialization of perovskite solar cells. For example, carbon electrode based perovskite solar cells can greatly reduce production costs.

Achievements

Publications

(1) **Putao Zhang**, Fu Yang, Muhammad Akmal Kamarudin, Chi Huey Ng, Gaurav Kapil, Tingli Ma, Shuzi Hayase. Performance Enhancement of Mesoporous TiO_2-Based Perovskite Solar Cells by SbI_3 Interfacial Modification Layer. ***ACS applied materials & interfaces*****, 2018**, 10, 29630-29637. **(IF=8.097)**

(2) **Putao Zhang**, Gaurav Kapil, Kengo Hamada, Shyam S. Pandey, Tingli Ma, Shuzi Hayase. Study Pertaining To Observe the Effect of PbI_2 Passivation on Carbon Electrode for Perovskite Solar Cells by Quartz Crystal Microbalance System. ***ACS Sustainable Chem. Eng.*** **2018,** 6, 10221-10228 (**IF=6.140**)

(3) **Putao Zhang**, Fu Yang, Kapil, G., Shen, Q., Toyoda, T., Yoshino, K. Shuzi Hayase. Enhanced performance of ZnO based perovskite solar cells by Nb_2O_5 surface passivation. ***Organic Electronics*** **2018.** 62, 615-620.(**IF=3.680**)

(4) **Putao Zhang**, Fu Yang, Gaurav Kapil, Chi Huey Ng, Tingli Ma, Shuzi Hayase. Preparation of Perovskite Films under Liquid Nitrogen Atmosphere for High Efficiency Perovskite Solar Cells. ***ACS Sustainable Chem. Eng.,*** **2019,** 7, 3956-3961. (**IF=6.140**)

(5) Yang, Fu. , **Zhang, Putao.** , Kamarudin, M. A., Kapil, G., Ma, T. and Hayase, S. (2018), Addition Effect of Pyreneammonium Iodide to Methylammonium Lead Halide Perovskite-2D/3D Hetero Structured Perovskite with Enhanced Stability. ***Advanced functional materials***.**2018 (IF=13.325)**

(6) Zhen Wang , Anusha Pradhan, Muhammad Akmal kamarudin , Manish Pandey , Shyam S. Pandey , **Putao Zhang** , Chi huey Ng, Atul S.M. Tripathi, Tingli Ma , and Shuzi Hayase*

Passivation of Grain Boundary by Squaraine Zwitterions for Defect Passivation and Efficient Perovskite Solar Cells. ***ACS applied materials & interfaces***, **2019** DOI: 10.1021/acsami.8b22044

Conferences

1 "Study pertaining to observe the effect of PbI_2 passivation on carbon electrode for perovskite solar cells by quartz crystal microbalance system" Putao Zhang, Gaurav Kapil, Kengo Hamada, Shyam S. Pandey, Tingli Ma, and Shuzi Hayase. 2018 Asia-Pacific Hybrid and Organic Photovoltaics Conference (AP-HOPV), Kitakyushu, Japan, 28th-30th January, 2018. (Poster)

2 "Performance enhancement of mesoporous TiO_2-based perovskite solar cells by SbI_3 interfacial modification layer" Putao Zhang, Fu Yang, Muhammad Akmal Kamarudin, Chi Huey Ng, Gaurav Kapil, Tingli Ma, Shuzi Hayase. The 79th JSAP autumn meeting, Nagoya, Japan, 18th-21th, September, 2018. (Poster)

Acknowledgements

In 2016, I am honored to enter Hayase Lab. in Kyushu Institute of Technology and study as a Ph.D scholar. First, I would like to express my deepest thanks to my supervisor Professor Shuzi Hayase for giving me the opportunity to study here. He is very knowledgeable on optoelectronic devices, having taught me much knowledge in this field. He gave me great guidance in his doctoral thesis. In daily life, he is very peace and patient. He has a lot of excellent qualities worth learning, setting an excellent example for my future work and study.

In the research work of the doctoral period, I also got the help of Prof. Tingli Ma. Prof. Ma is very professional in nanomaterials and solar cells. Thanks to Prof. Ma for her guidance and help in the experiment and life. Associate Professor Shyam S. Pandey is a good teacher in daily life. He has given valuable advice on laboratory safety, also gave me a lot of help in modifying the paper. Without helps of Prof. Ma and associate Prof. Pandey, I could hardly finish my research and doctoral thesis in time. Furthermore, Prof. Ma and associate Prof. Pandey kindly gave me many of helps in my daily life, including helping me write a letter of recommendation when I am looking for a job.

I want to thank every member of the Hayase Lab. When I was confused or in trouble, they gave me a lot of encouragement and comfort, and filled me with energy. In particular, I want to thank Gaurav Kapil, Dr. Zhaosheng Hu, Dr. Muhammad Akmal Kamarudin. Dr. Chi Huey Ng, Dr. Fu Yang, Dr. Zhen Wang, Dr. Kengo Hamada, and all master students and staffs. With their help, I successfully carried out my research.

I am very grateful to the China Scholarship Council (CSC) for funding in my doctoral period.

Moreover, I want to thank my wife and parents. They don't have too high demands and expectations for me, only hope that I have a healthy body and a positive attitude. I am very grateful for this. Thanks for their support and encouragement. At last, I would like to express my gratitude to those who have contributed to this thesis.